VNIVERSITAT DE VALÈNCIA

Doctorado en Nanociencia y Nanotecnología

Ph.D. thesis:

Ionic-Electronic Interaction in Optoelectronic and Sensing Devices

Ph.D. candidate:

Enrico Bandiello

Supervisors:

Dr. Hendrik Jan Bolink

Dr. Michele Sessolo

Tutor:

Dr. Michele Sessolo

Diciembre 2016

D. Hendrik Jan Bolink y **D. Michele Sessolo**, Investigador de la Universidad de Valencia en el Instituto de Ciencia Molecular (ICMol) e Investigador Postdoctoral del Instituto de Ciencia Molecular, respectivamente, certifican que la memoria presentada por el doctorando Enrico Bandiello con el título "Ionic-electronic interaction in optoelectronic and sensing devices" corresponde a su Tesis Doctoral y ha sido realizada bajo su dirección y tutoría, autorizando mediante este escrito la presentación de la misma.

En Valencia, a 25 de Noviembre de 2016

Dr. Hendrik Jan Bolink	Dr. Michele Sessolo	Dr. Michele Sessolo
(director)	(director)	(tutor)

Dedicated to my little,
wonderful family.

Acknowledgments

First, I would like to thank my thesis director, Dr. Hendrik Jan Bolink, for trusting in me and accepting me as a Ph.D. student in his group. I am very grateful to him for supporting me at every level, for giving me the freedom to pursue my own particular research interests and for all the discussions and suggestions about matters often unrelated with Science and Research. At the same time, I need to sincerely thank my Ph.D. advisor and thesis co-director Dr. Michele Sessolo for the helpful discussions during many laboratory sessions and coffee breaks and for his tireless didactic attitude. I am especially grateful to him for his patience and his friendly encouragements while listening to my rants when I was struggling with the not-so-infrequent bad experimental results that plague the everyday life of the average Ph.D. student (and for teaching me that problems are often simpler than they appear at a first sight...).

Even if I cannot name them individually here, I feel the need to thank all my colleagues (friends!) from ICMol and all the people that I have worked with over these years. I feel that each one of them has taught me something on a professional or on a human level. I would like them to know that I feel very fortunate to have been part of such a wonderful work group and I sincerely hope that our friendship will continue even after our professional careers will have taken different paths.

I would like to show my gratitude to Prof. George Malliaras and to all the people working at Department of Bioelectronics of the École Nationale Supérieure des Mines de Saint-Etienne for accepting me in their group for my research stay and for contributing to make it so productive and, above all, so pleasant. In particular, I'd like to thank Dr. Jonathan Rivnay, who was my tutor during my research stay.

Thanks to Jorge Ferrando for his invaluable help with all the laboratory setup and for putting his LabView programming skills at work every time it was needed for my experiments. Equally, thanks to Ángel López for always taking the time to help me with everything I needed, even when he was more in hurry than I was. Thanks to Dr. María Monrabal for proofreading and editing the spanish summary of the thesis and to Dr. Antonio Pertegás for his useful comments about the chapter on light-emitting electrochemical cells.

Finally, I will never be grateful enough to the persons that have been supporting and trusting me unconditionally along all these years: my mother and my father. Even if he is not here anymore, I know that my father would have been proud of my achievements, because he knew that I inherited from him my passion for Science.

Dulcis in fundo, I have a pleasant debt of gratitude with my wife Karina and with my son Francesco for their help and their patience while putting up with my bad mood in my most stressful moments, especially during these last months. I am sure that I would not have come this far without them. Thank you for being at my side.

1. Introduction and aim

1.1. Introduction

The working mechanism of today's most common solid-state optoelectronic devices such as field effect thin-film transistors (TFTs), light-emitting diodes (LEDs) and solar cells is based solely on electronic processes, meaning that only electronic charges play a role, while the effects related to ionic charges are either absent, irrelevant or even detrimental for their purposes. On the other hand, many applications do actually benefit from the presence of ions in the structure of a device. One typical example in the research field for inexpensive and efficient lighting sources are light-emitting electrochemical cells (LECs).[1] These are light emitting devices composed by a single ionic electroluminescent layer sandwiched between two electrodes. The ions in the active layer are either added during the fabrication process (LECs based on electroluminescent polymers blended with ionic liquids) or are part of the electroluminescent compound (LECs based on ionic transition metal complexes (iTMCs),[2,3] even if also in this case a small amount of ionic liquid or other salts is often added to enhance the LECs performances.[4,5] The deposition of the active layer can be performed by simple solution processing (i.e. spin coating, dip coating, meniscus coating). When a voltage bias V_{bias} is applied at the external contacts, mobile ions in the active layer migrate towards the electrodes and favor the injection of holes and electrons from the electrodes themselves. When the injection barriers are overcome and if V_{bias} is large enough (higher than E_{g}/e, where E_{g} is the band gap of the active material and e is the elementary charge), electrons and hole are injected into the LUMO and the HOMO of the electroluminescent material, respectively (HOMO is the acronym for highest occupied molecular orbital, and is the analogue for organic semiconductors of the top of the valence band of inorganic semiconductors; similarly, LUMO is the acronym for lowest unoccupied molecular orbital, the analogue for organic semiconductors of the bottom of conduction band of inorganic semiconductors). The charge carriers are then driven by diffusion into the bulk of the active layer, where they recombine radiatively. The mechanism by which the charge carrier injection and transport take place has been object of an intense debate (*electrochemical model* vs. *electrodynamical model* vs. *unified model*, see Section 3.1),[6] nonetheless the main principle is that the ionic-assisted charge injection allows the fabrication of simple and potentially inexpensive light-emitting devices whose performances are only weakly affected by the work function of the chosen electrodes, since the charge injection is self-regulated by the ionic mechanism.[7]

The "non-ionic" counterpart of LECs are the widely studied and already commercialized organic light-emitting diodes (OLEDs). State-of-the-art OLEDs are multi-layer devices whose manufacturing requires multi-step vacuum deposition techniques, which are still too expensive to make OLEDs a viable alternative in the mainstream lighting market.[8] In general, multi-layer solution processing is difficult because the solvent needed to deposit a layer has to be carefully chosen to avoid damaging of the underlying stack of layers. This step, moreover, can introduce wetting issues which complicate the uniform deposition of the desired material. In the case of OLEDs, the multilayer approach is used in order to integrate the structure of the device with electron- and hole-injection and transport layers to facilitate the optimal displacement and confinement of charge carriers into the bulk of the electroluminescent material. Moreover, unlike LECs, OLEDs need rigorous encapsulation not only to protect the organic materials from air or moisture, but also because to ensure an efficient electron injection low work function, reactive metals such as Ba or Ca can be used as the cathode.[9] These constraints can be circumvented in LECs, at least partially.

It is important to point out that LECs and OLEDs show great differences in their performances such as efficiency, lifetime, and turn-on time. In general, while LECs are still an ongoing research topic, OLEDs are a mature technology that is already being used in commercial applications such as displays.

In many cases the interplay between ions and electrons can boost the performances of already existing devices, as in the case of electrolyte-gated transistors (EGTs), that have their counterpart in traditional solid-state TFTs. As will be shown more in detail in the following sections, EGTs share the same working principle of TFTs, meaning that they are fundamentally (organic) field-effect transistors, (O)FETs, in which the gate insulator is replaced by a suitable electrolyte in direct contact with the semiconductor channel. Under the application of a small gate bias (typically below 3 V), the ions in the electrolyte accumulate at the interface of the semiconductor, forming a thin electrical double layer (EDL). As the area capacitance of the EDL is much higher compared to that of common insulator, and considering that the current modulation in an (O)FET is proportional to that same capacitance, EGTs can be operated at a very low voltage. Moreover, unlike in classical (O)FETs, the performances of EGTs are in principle independent of the thickness of the electrolyte. This translates in a much simpler fabrication because processes such as drop casting or spin coating can be employed for the deposition of the electrolyte. Also, the organic semiconductor itself can be functionalized or, alternatively, the architecture of the transistor can be modified to make it suitable as a sensor for biologically relevant ions or analytes.[10–15]

More recently, another class of devices whose behavior is influenced by the interaction between ions and electrons has gained popularity among the research community. These are the solar cells based on hybrid organic-inorganic perovskites. Perovskite is the name of the crystalline structure of the photoactive material. The hybrid character of perovskites used in photovoltaics comes from these materials being composed by organic cations intercalated in an inorganic framework. The most commonly used perovskite for photovoltaics is methylammonium lead iodide ($CH_3NH_3PbI_3$). The popularity of the solar cells based on this material is due to the extraordinary photovoltaic performances that they can deliver,[16–18] together with the flexibility of the preparation methods, ranging from vacuum deposition to simple solution processes.

Despite their outstanding performances, perovskite solar cells (PSCs) are rather peculiar devices because, unlike classical solid state or even organic solar cells, they often present a certain degree of hysteresis in their current density–voltage measurements (J–V), depending on the speed and direction of the voltage scan,[19] and also transient phenomena in photocurrent on timescales of the order of hundreds of seconds are often observed.[19,20] This leads to uncertainties about the "true" performances of these devices, which cannot be inferred confidently by a simple J–V scan.[21] While many attempts have been made to explain and mitigate such a particular behavior, one of the hypotheses involves the presence of mobile ions in the perovskite layer itself.[19,22] These ions influence the operation of a PSC and as such they can be used to tune or improve the extraction of photogenerated charges.

1.2. Aim of the thesis

The aim of this work is to demonstrate that the interplay between the ionic and the electronic charges can be employed as a tool for the development of new devices based on traditional paradigms, and to understand how the presence of given mobile ionic species can influence the behavior of devices such as light-emitting electrochemical cells and solar cells. In particular, this will be demonstrated using the following specific cases:

- ▹ The fabrication and characterization of an EGT based on the zinc oxide semiconductor (ZnO) that works at low voltage in an aqueous environment. The EGT is integrated with an ion-selective membrane to serve as an ion sensor for the selective measurement of K^+ ions in an electrolyte. Moreover, the transistor is used as a glucose sensor through the functionalization of the ZnO with the glucose oxidase enzyme.

- ▹ The influence of lithium salts as substitutes for ionic liquids on the performances and lifetime of iTMC LECs. The behavior of the LECs is shown to be heavily dependent on the lithium counterion.

- ▹ The electroluminescence of a perovskite solar cell under bias. The effect of the bias on a unipolar device is the onset of an ambipolar charge injection regime and an improved electroluminescence, just like in the case of light-emitting electrochemical cells. Moreover, the efficiency of a degraded device can be partially recovered after biasing it for few minutes. The presence of mobile ions in the perovskite explains the similarities between the processes observed in the solar cell and those that are predominant in LECs

2. Electrolyte-Gated Transistors for Environmental and Biological Sensing

2.1. Field effect transistors

In this section, some basic concepts about FETs and their characterization will be outlined. These concepts will be useful in Section 2.2 and Section 2.3, where electrolyte-gated transistors and ion/glucose sensors based on EGTs will be introduced.

A transistor is called every device with three terminals in which the resistance of a (semi)conductor (*channel*) between two of the electrodes (*source* and *drain*) can be controlled by the voltage V_g applied to the third electrode (*gate*). In most common TFTs the semiconductor is separated from the gate by a thin insulating layer, usually SiO_2 or a high dielectric constant material (Figure 2.1). When a fixed voltage V_d is applied between the source and the drain, the current I_d between these two electrodes can be modulated by varying V_g. These devices are mainly used to amplify signals and to translate a variation of voltage (ΔV_g), whatever its origin is, into a variation of current (ΔI_d). As such, they are also

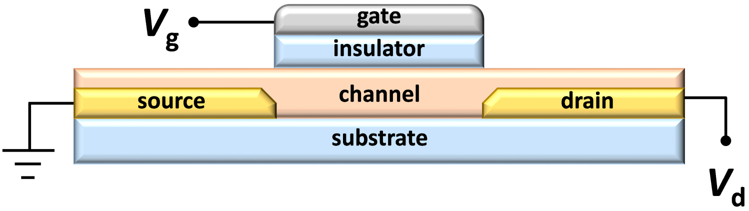

Figure 2.1.: Structure of a bottom-contact, top-gate TFT. Conventionally, the source contact is used as the reference for V_g and V_d. I_d is the current flowing through the semiconducting channel.

known as *transducers*. The structure shown in Figure 2.1 is flexible, meaning that many configurations of the same TFT exist, according to the relative positions of the electrodes (top/bottom contact and/or gate). By convention, V_d and V_g are both referred to the potential of the source electrode, which is usually grounded.

The working principle of a FET is based on the capacitive polarization induced by the gate voltage on the insulator. When a suitable gate bias is applied, charge carriers that are injected from the source into the semiconductor material accumulate at the interface with the insulator, creating a conductive channel. The application of a drain voltage causes these carriers to drift, producing a current I_d. According to the sign of the carriers accumulating in the semiconductor layer, the transistor is said to be *p*-type (V_g, V_d and $I_\mathrm{d} < 0$; the conductive channel is formed by holes from the source that accumulate in the semiconductor at the interface with the insulator and drift towards the drain) or *n*-type (V_g, V_d and $I_\mathrm{d} > 0$; the channel is formed by electrons that drift toward the drain electrode). This convention also explains the terminology used for FETs: independently of the sign of their charge, the majority carriers always originate on the source electrodes and drift towards the drain electrode, their flow rate (current) being controlled by the gate voltage.

The devices described above fall in the class of the *enhancement mode* (or

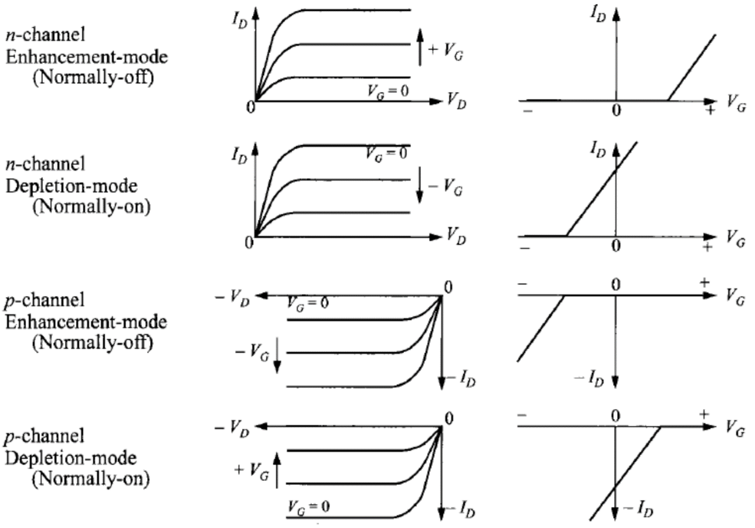

Figure 2.2.: Current dependence on V_g and V_d for the different character and working mechanism of a FET. On the left: output characteristics (I_d as a function of V_d for a fixed V_g). On the right: transfer characteristic (I_d as a function of V_g for a fixed V_d).[23]

accumulation mode) transistors, meaning that they are in their *off* state (no conductive channel, $I_\mathrm{d} = 0$) when $V_\mathrm{g} = 0$ and they turn *on* ($I_\mathrm{d} \neq 0$) only when $|V_\mathrm{g}|$ is sufficiently higher than 0, with $|I_\mathrm{d}|$ increasing with $|V_\mathrm{g}|$. This is the usual working mode for solid-state FETs. On the other hand, other transistors work in *depletion mode*, meaning that the channel is conductive (ohmic) at $V_\mathrm{g} = 0$ and its conductivity decreases when $|V_\mathrm{g}| \neq 0$. Both classes of devices can be either *p*- or *n*-type. So, a basic classification of FETs will include their *p* or *n* character and their accumulation/depletion mode working mechanism.[23] The above terminology will be used during this thesis also in reference to EGTs.

In Figure 2.2 a schematic plot of the current in a FET according to its classification is shown. The typical study of a FET requires plotting the dependence of I_d from V_d and V_g, separately. These plots are called *output characteristics* and

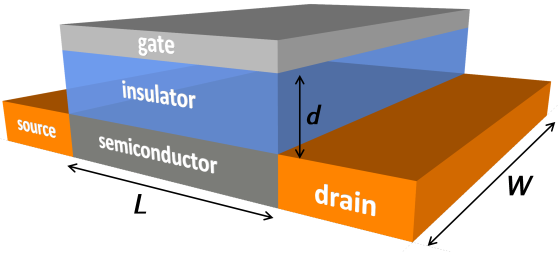

Figure 2.3.: Geometrical parameters of a TFT: interelectrode distance or *channel lenght* (L), channel width (W) and thickness of the insulator (d).

transfer characteristics respectively (or simply *output* and *transfer*), and allow the extraction of many characteristic parameters.

The current in a FET depends on the geometrical parameters of the transistor itself such as W, the width of the source/drain electrodes (*channel width*) and their distance L (*channel lenght*), both shown in Figure 2.3. Taking as an example a prototypical n-type device working in accumulation mode, the family of curves in Figure 2.4 shows how the drain current changes when an increasing V_d is applied, while keeping V_g fixed. A nearly linear (ohmic) part is present in all the curves for low values of V_d and is called the *linear regime.* It is described by Eq. (2.1), in which C_ins is the capacitance of the insulator for unit area ($C_\mathrm{ins} \propto d^{-1}$, where d is the thickness of the insulator) and μ_e is the electron mobility:

$$I_\mathrm{d}\left(V_\mathrm{d}\right) = \frac{W}{L}\mu_e C_\mathrm{ins}\left(V_\mathrm{g} - V_\mathrm{th} - \frac{V_\mathrm{d}}{2}\right)V_\mathrm{d} \approx \frac{W}{L}\mu_e C_\mathrm{ins}\left(V_\mathrm{g} - V_\mathrm{th}\right)V_\mathrm{d}. \tag{2.1}$$

The parameter V_th is called *threshold voltage* and represents the minimum gate voltage necessary to create a conductive channel between the source and the drain electrodes. It depends mainly on the channel semiconductor and the dielectric,[24] even if slight variations of V_th have been reported in an organic TFT depending on the work function of the gate metal.[25] The rightmost part of Eq. (2.1) holds

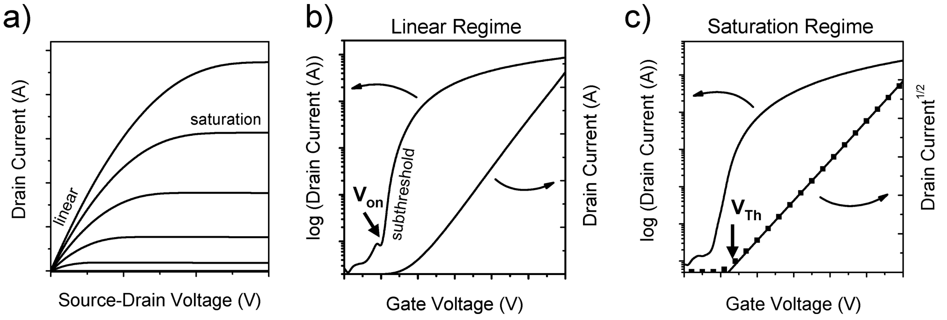

Figure 2.4.: a) Output and transfer characteristics in b) the linear regime and c) the saturation regime for a generic FET.[24]

for $V_\mathrm{d} \ll (V_\mathrm{g} - V_\mathrm{th})$, when the "linearity" is almost fulfilled. For higher values of $V_\mathrm{d} > (V_\mathrm{g} - V_\mathrm{th})$, the current saturates: this is called the *saturation regime* and the current reaches a value $I_\mathrm{d,sat}$, independent from V_d, given by Eq. (2.2)

$$I_\mathrm{d,sat} = \frac{W}{2L}\mu_e C_\mathrm{ins} \left(V_\mathrm{g} - V_\mathrm{th}\right)^2 . \tag{2.2}$$

From (2.1) and (2.2), the value of the FET mobility μ_e in both situations can be extracted, using Eq. (2.3) and (2.4):

$$\mu_{e,\mathrm{lin}} = \frac{\partial I_\mathrm{d}}{\partial V_\mathrm{g}} \frac{L}{W C_\mathrm{ins} V_\mathrm{d}} = g_\mathrm{m} \frac{L}{W C_\mathrm{ins} V_\mathrm{d}} = s_\mathrm{lin} \frac{L}{W C_\mathrm{ins} V_\mathrm{d}} \tag{2.3}$$

$$\mu_{e,\mathrm{sat}} = \frac{\partial I_\mathrm{d,sat}}{\partial V_\mathrm{g}} \frac{L}{W C_\mathrm{ins} \left(V_\mathrm{g} - V_\mathrm{th}\right)} = g_\mathrm{m} \frac{L}{W C_\mathrm{ins} \left(V_\mathrm{g} - V_\mathrm{th}\right)} = s_\mathrm{sat}^2 \frac{2L}{W C_\mathrm{ins}} . \tag{2.4}$$

The magnitude $g_\mathrm{m} = \partial I_\mathrm{d} / \partial V_\mathrm{g}$ is one of the most important parameters for FETs and it is called the *transconductance* of the transistor: it gives a measurement of how much the drain current varies for a small variation of V_g. The parameters s_lin and s_sat can be extracted from the transfer characteristic as in Figure 2.4 and are the slope of the I_d and $I_\mathrm{d}^{1/2}$, respectively, as a function of V_g for a fixed

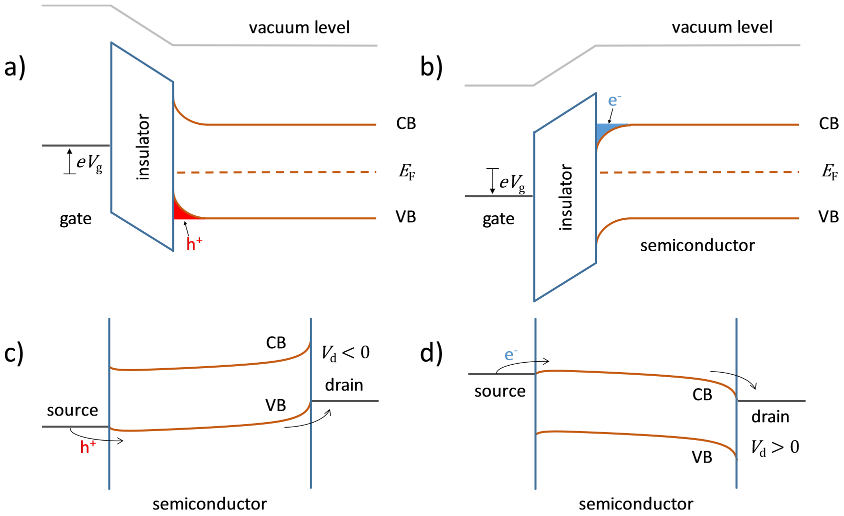

Figure 2.5.: Simplified energy band diagram for the working mechanism of a TFT after the formation of the conductive channel ($|V_g| > |V_{th}|$), in a plane perpendicular to the source-drain electrodes: a) *p*-type, b) *n*-type. The situation in a plane parallel to source-drain, when $|V_d| > 0$: c) *p*-type and d) *n*-type.

V_d. The threshold voltage V_{th} can be measured by linearly fitting $I_d^{1/2}$ in the saturation regime and taking V_{th} as the intercept of the extrapolated value on the V_g axis. Alternatively, V_{th} can be measured in the linear regime, if $V_d \ll V_g$, extrapolating the linear fitting of I_d and taking the intercept on the V_d axis. The obtained value in this case is $V_{th} + {}^1\!/\!{}_2 V_d$.[23]

Another important parameter for a FET is its *on*/*off* ratio, i.e. the ratio between its current in the saturation state and the current in the *off* state, which can be read directly on the transfer output. The *on*/*off* ratio of a FET can span several orders of magnitude and is a measurement of the increase of the conductivity of the semiconductor channel (or its decrease, in case of a depletion-mode transistor).

To better visualize the formation of the channel in a TFT, a simplified energy band diagram of an accumulation-mode TFT is shown in Figure 2.5a and 2.5b, which represent the energy in a plane perpendicular to the source-drain axis, when $|V_\mathrm{g}| > |V_\mathrm{th}|$. The reduction of the injection barrier controlled by V_g allows carriers from the source to be injected into the semiconductor. A current flow I_d between the source and the drain is then established in presence of a drain voltage, as in Figure 2.5c and 2.5d.

2.2. Electrolyte-gated transistors

In this section the basic working mechanism of EGTs will be elucidated, along with some examples of how these devices can be employed as sensors.

The working voltage for a typical solid-state or organic FET is typically in the range of tens of volts. From (2.1) and (2.2) it is evident that the amplification of the current due to the gate voltage in a FET is directly proportional to W and to the inverse distance of the source and drain electrodes L. So a method to increase the amplification factor of a FET would be to build a transistor with very large electrodes separated by a relatively small distance. On the other hand, this is not easily achievable, as transistors with an interelectrode distance of less than 5 µm are difficult to obtain *via* standard optical photolithographic techniques on the laboratory scale.

An alternative approach to improve FETs performances is increasing the capacitive term C_ins in (2.1) and (2.2) given that, as can be seen in Eq. (2.5), the transconductance is proportional to C_ins:

$$g_\mathrm{m} = \frac{\partial I_\mathrm{d}}{\partial V_\mathrm{g}} \propto C_\mathrm{ins} = \frac{\epsilon \epsilon_0}{d}. \tag{2.5}$$

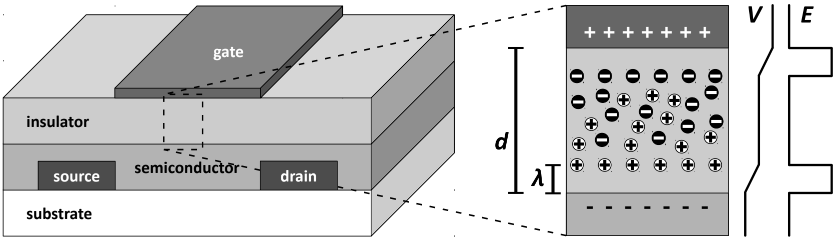

Figure 2.6.: Working principle of an electrolyte-gated transistor (n-type); d is the thickness of the insulator, λ is the thickness of the EDL at the interface with the semiconductor channel. The trend of the potential V and of the electric field E are also shown.

As the specific capacitance of the insulator is a function of the relative permittivity of the material ϵ and of its thickness d, the most straightforward strategy to improve g_m is to use very thin insulators with a large dielectric constant. In practice this is achieved in solid-state FETs by using thin layers ($< 100\,\mathrm{nm}$) of the SiO_2, Al_2O_3 or Ta_2O_5 insulators,[26–28] self-assembled molecular (SAM) monolayers,[29] or even simple polymers like poly(methyl methacrylate) (PMMA) or polystyrene (PS).[30] In this way, specific dielectric capacitances on the order of several $\mathrm{nF\,cm^{-2}}$ can be achieved.

A clever strategy to increase the transconductance and to lower V_th consists in replacing the solid state/SAM/polymeric gate insulator with a suitable liquid or polymeric electrolyte.[15] When the semiconductor channel is impermeable to ions, an EGT is obtained (Figure 2.6). The value of C_ins in (2.5) is not determined anymore by the thickness d of the insulator, but by the thickness λ of the electrical double layer (EDL) that is formed at the interface of the electrolyte with the semiconductor because of the applied V_g (λ is also called the *Debye screening length*). As the value of λ is generally orders of magnitude lower than d and C_ins scales with λ^{-1} for a single EDL, specific capacitances in the order of 1–100 µF cm^{-2} can be reached, resulting in enhanced channel conductance values.[11,14,15]

It has to be noted that the gate electrode plays an important role in determining the total capacitance C_{ins}: given that ion accumulation takes place at both gate/electrolyte and semiconductor/electrolyte interfaces, the actual total capacitance is given by the series capacitance of these two EDLs, C_{gate} and C_{sc}:

$$C_{\mathrm{ins}} = \left(C_{\mathrm{gate}}^{-1} + C_{\mathrm{sc}}^{-1}\right)^{-1} = \frac{C_{\mathrm{gate}} C_{\mathrm{sc}}}{C_{\mathrm{gate}} + C_{\mathrm{sc}}}. \tag{2.6}$$

Eq. 2.6 also implies that C_{ins} is dominated by the lowest between C_{gate} and C_{sc}. The maximization of the transistor performances requires thus the maximization of the potential drop in the EDL at the interface between the electrolyte and the semiconductor. This can be achieved either by choosing a gate electrode with an area much larger than the $(W \cdot L)$ product, or by using a so-called *non-polarizable* electrode (NPE). A typical NPEs is a Ag/AgCl pellet, commonly used in electrochemistry. In presence of an electrolyte, at the surface of an Ag/AgCl electrode a redox reaction such as

$$\mathrm{Ag} + \mathrm{Cl}^{-} \longrightarrow \mathrm{AgCl} + \mathrm{e}^{-}$$

takes places, so that a steady current flows from the electrode to electrolyte preventing the formation of the EDL. In short, when a NPE is used as the gate in an EGT, the potential due to V_{g} mainly drops at the electrolyte-semiconductor interface.[31] The inherent large area due to the porosity of the material further facilitates the maximization of g_{m}. On the other hand, the work function of the gate itself also defines the final behavior of the transistors: for example, high-work function metal such as Au are more suitable to be used in p-type EGTs, as they can significantly lower the threshold voltage of the device.[32]

Unlike in TFTs, the performances of EGTs are largely independent of the thickness of the electrolyte layer, so in the case of a “soft” electrolyte (a liquid or a polymer) quick deposition methods can be employed, such as drop casting or spin coating. The reliance of the working mechanism on the ionic conductivity of the electrolyte, however, implies that the thicker a given electrolyte, the slower the response of the transistor when changes in V_g occur. However, response times of the order of 10 µs have already been recorded in EGTs using a polyelectrolyte as the gate insulator.[33]

Apart from their inherent advantages over FETs such as the low threshold voltage[34] and their high transconductance,[35] the electrolytes in EGTs can be structurally flexible or conformable, making these devices suitable in applications in which traditional solid-state FETs would be difficult or impossible to use, i.e. in textiles.[36] More importantly, the electrolyte being in direct contact with the semiconductor makes relatively easy to use such devices as biosensors for ions, molecules, proteins. As an example, in EGTs using a liquid electrolyte the transistor can be modified or the channel semiconductor can be functionalized to react according to the content and/or the concentration of the solution. A given analyte can hence be used as the electrolyte, allowing the monitoring of its parameters of interest by the changes in the current–voltage behavior of the EGT.[37–40]

2.3. ZnO electrolyte-gated transistors for ion and glucose sensing

As mentioned in the previous sections, EGTs can be used as sensors for the measurement of relevant ions or molecules. Here an EGT based on the ZnO semiconductor will be presented. The transistor works in an aqueous environment, using a solution with salts as the electrolyte. The performances of the device are shown, along with its characterization when it is modified and used as a potassium or glucose sensor.

2.3.1. Introduction

Metal oxides (MOxs) are convenient semiconductors for transistors to be used in biosensing as they have attractive features such as high carrier mobility[41], easy functionalization[42,43] and they can be deposited by inexpensive solution method.[44,45] Unlike organic semiconductors, they are stable in air and usually in water. The latter is a fundamental requisite for devices working in an aqueous or physiological environment. Nonetheless, even MOxs that are slightly soluble in water can be useful for the purposes of biosensing, as they can be integrated in implantable, biosorbable devices that would slowly being absorbed by the body.[46,47] One of such MOxs is ZnO, which is easily processed from solution, being it readily available as nanoparticle suspensions in many different solvents.

The idea behind an EGT with a nanostructured channel, such as one made by sintered ZnO nanoparticles, is that a nanostructured/porous channel would offer a very large area for the semiconductor to interact with the electrolyte, with respect to a flat surface (Figure 2.7a). A rough estimate, considering a single layer of identical spherical nanoparticles with a diameter of 35 nm, gives an approximate 3-fold increased surface area, for a transistor channel with $W = 2000\,\mu\text{m}$ and $L = 20\,\mu\text{m}$. Of course, the sintering process and the irregular shape of the nanoparticles can decrease this factor. Nonetheless, the increased surface area would allow a large modulation of the current with the gate bias (Figure 2.7c).

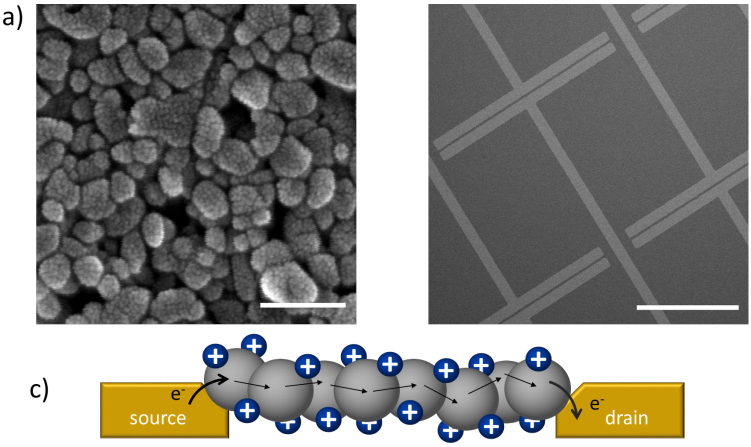

Figure 2.7.: a) SEM image of a nanoporous layer of ZnO nanoparticles after the sintering process. Scale bar: 100 nm. b) SEM image of the source-drain electrodes after the ZnO deposition. Scale bar: 1000 µm. C) Working mechanism for a EGT with a channel constituted by MOx nanoparticles.

Taking advantage from the good behavior of the transistor (see Section 2.3.3), an ion sensing device was fabricated. An *ion sensor* is defined as a device that is able to *selectively* measure the ionic concentration in a given solution, meaning that only one ionic species influences the response of the sensor. In the case of an EGT, an ion sensor can be built by integrating an *ion selective membrane* (ISM) in the structure of the transistor. Across such a membrane a potential difference is established when its opposite faces are in contact with solutions of different concentrations in a given ion X^{z+} (assuming that the species that has to be quantified is a cation). This potential difference acts as an additional effective gate bias and the current in the EGT is modulated by the different concentration of the ions at both faces of the ISM. In a given concentration range, the potential

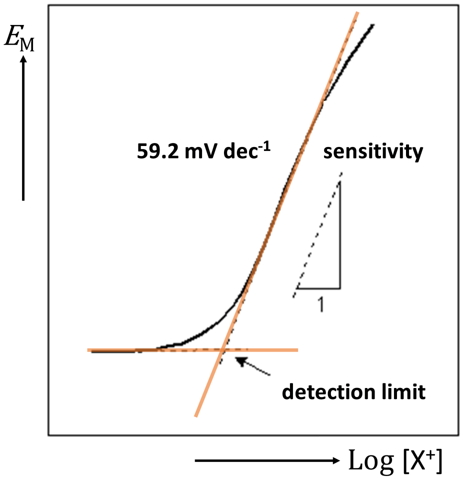

Figure 2.8.: Ideal Nernstian behavior of an ion sensor for monovalent ions at RT. The range of validity of the law is represented by the linear part of the curve.

difference across an ISM follows Nernst's Law

$$E_\mathrm{M} = E^0 + \frac{RT}{zF} \ln \frac{[\mathrm{X}^{z+}]_\mathrm{o}}{[\mathrm{X}^{z+}]_\mathrm{i}}, \tag{2.7}$$

where R is the gas constant, F is Faraday's constant and T is the absolute temperature, while z is the charge of the ion X^{z+}. The term E^0 includes all the contributions to the potential difference that are independent from the sample under study (for example, an external voltage).[48] In the case of monovalent ions ($z = 1$) at room temperature (298 K, RT), changing the natural logarithm in Eq. (2.7) into a base 10 logarithm, we have that $(RT/zF) \cdot \ln(10) = 59.2\,\mathrm{mV}$. This means that the potential drops across the membrane changes in about 60 mV for a variation of a decade of the ionic concentration.

The properties of the membrane define the behavior of the sensor, schematically represented in Figure 2.8. The slope of the linear part of the potential difference

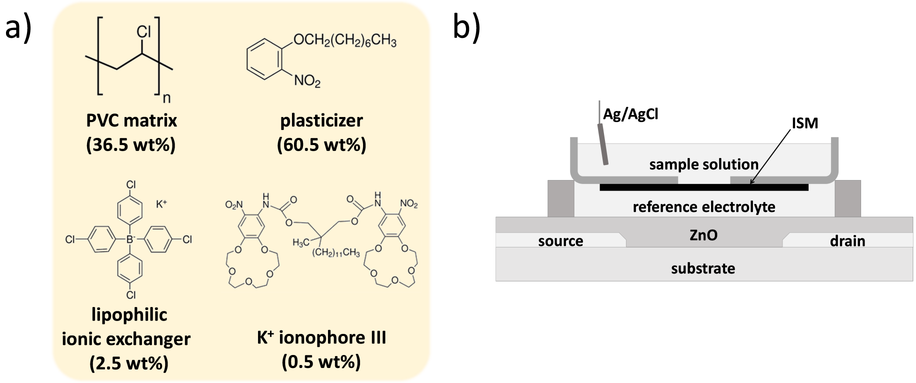

Figure 2.9.: a) Components of the ISM used in our ion sensor, together with their weight ratios in the membrane. b) Structure of the ion sensor, with the membrane separating the reference electrolyte from the analyte.

vs. the concentration is called the *sensitivity* of the sensor. In the conditions mentioned above, the maximum theoretical sensitivity is $59.2\,\mathrm{mV\,dec^{-1}}$ (Nernst limit). The intercept of the extrapolated linear part with the baseline, when projected on the axis of abscissas, defines the *detection limit*, i.e. the minimum concentration that can be measured by the sensor.

In our case, the ion of interest was K^+, so an ISM capable to detect K^+ ions was used. Importantly, a potential difference across the membrane can also arise in presence of different cations. Hence, a parameter called *selectivity* quantifies the response of the sensor in presence of interfering ions (cations, in our case). The selectivity of an ISM sensor is entirely determined by the characteristics of the membrane, which in turn acquires its selectivity because of the ionophore that it contains. Ionophores are molecules able to preferentially bind only one ionic species, whereas other ions with the same charge will have a smaller binding constant. The other components of the ISM are the hydrophobic polymer polyvinyl chloride (PVC), a plasticizer and an ionic exchanger. The plasticizer gives elasticity to the PVC matrix, while the ionic exchanger allows the K^+ ions to penetrate into the membrane despite its hydrophobicity. The composition of the K^+-ISM used in this work is highlighted in Figure 2.9a. In our ion sensor, a reference solution, containing a known concentration of K^+, is placed in direct contact with the transistor channel and one of the faces of the ISM. The analyte is added on the other face of the ISM, so that a potential difference arises between the two sides of the ISM. The final structure of the ion sensor is depicted in Figure 2.9b.

The ZnO-based transistor can also be used as a glucose (GLC) sensor. For this purpose, the surface of the ZnO nanoparticles is covalently functionalized with the glucose oxidase enzyme (GOD). To achieve this, the first step is the deposition of a monolayer of (3-glycidyloxypropyl)-trimethoxysilane (GOPS) on the ZnO surface. The GOPS molecule has a methoxysilane group on one end, which binds with the OH groups naturally presents on ZnO, and an epoxy group on the opposite end, which is able to bind the GOD. So, after the GOPS deposition, an aqueous solution of GOD is allowed to react with the GOPS, binding the protein on top of the ZnO. A schematics of the process is represented in Figure 2.10. In presence of glucose (β-D-glucose) and GOD the following reaction takes place:

$$\beta\text{-D-glucose} + O_2 \longrightarrow \text{D-glucono-}\delta\text{-lactone} + H_2O_2. \tag{2.8}$$

In (2.8) the GOD catalyzes the reaction of β-D-glucose and the oxygen to produce D-glucono-δ-lactone (subsequently hydrolyzed to D-gluconate) and hydrogen peroxide. In presence of a Pt electrode the H_2O_2 decomposes on its surface as

$$H_2O_2 \longrightarrow 2\,H^+ + O_2 + 2\,e^-. \tag{2.9}$$

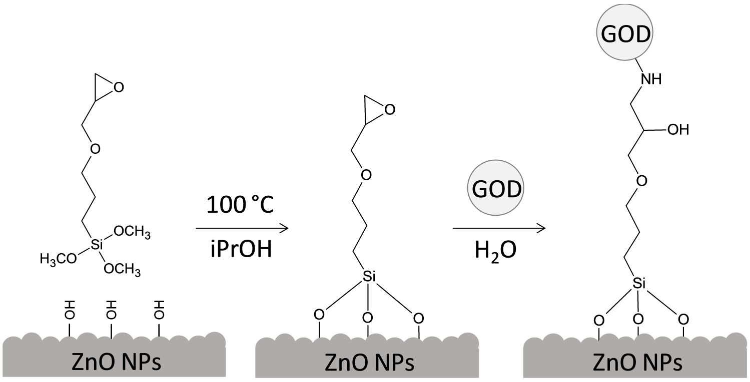

Figure 2.10.: Binding of the GOD on the surface of the ZnO nanoparticles.

The additional gate current caused by the oxidation of H_2O_2 at the Pt electrode causes an ionic redistribution in the electrolyte, hence modulating the channel conductivity.[49] Since platinum catalyzes the reaction in (2.9), the Ag/AgCl gate has been replaced by a Pt electrode, when our transistor has been used as a glucose sensor.[50]

2.3.2. Experimental methods

The ZnO-based EGTs have been fabricated by depositing a commercial ZnO nanoparticle suspension (average size $< 35\,\mathrm{nm}$) on a clean glass substrate with pre-patterned ITO source and drain electrode ($W/L = 2000\,\mathrm{\mu m}/20\,\mathrm{\mu m} = 100$) by spin coating. The nanoparticles where suspended in ethanol at 5 wt %. The suspension was filtered through a PTFE membrane with 0.22 µm pore size before the deposition. Due to the low boiling point of ethanol (≈ 78 °C) the spin coating process has been carried out in an ethanol saturated atmosphere, to slow down the evaporation of the solvent and be able to obtain smooth layers. After the deposition, sintering of the nanoparticles has been promoted by an annealing step of 30 min at 450 °C. The final thickness of the ZnO layer was ≈ 60 nm. An Ag/AgCl gate was used to modulate the current in the transistor. As the electrolyte, an aqueous KCl solution was employed (10^{-1} M). The electrolyte was in contact with the source and drain electrodes through the nanoparticulate layer, as no insulator was used on the contacts.

The performances of the transistor and the sensors' response were measured using a Keythley 2636B potentiostat-amperometer driven by a custom-made LabView program. The EDL capacitance of the nanostructured and of the flat ZnO layers was measured as a function of frequency by means of a Gamry Interface 1000 potentiostat. The flat ZnO layer were prepared by a SOL-GEL method by dissolving zinc acetate dihydrate ($Zn(O_2CCH_3)_2(H_2O)_2$) in a mixture of ethanol and water 3:1 vol. Acetic acid was added in order to avoid the precipitation of zinc hydroxide ($Zn(OH)_2$) and to improve the film formation.[51] The solution was deposited by spin coating on a clean glass-ITO substrate, which was then heated at 450 °C to allow the formation of a flat ZnO film. The final area of the contact was 4.46 mm^2.

The ion selective membrane used for the K^+ sensor has been fabricated by drop casting a tetrahydrofuran mixture containing polyvinyl-chloride (PVC), diisodecyl adipate (a plasticizer), potassium ionophore III (the ionophore) and potassium tetrakis(4-chlorophenyl)-borate (the ionic exchanger) in the 36.5:60.5:2.5:0.5 wt % onto a clean glass slide. The solution, confined within the borders of a small rubber funnel, was allowed to dry at room temperature to form the membrane, which was subsequently peeled off together with the funnel. The calibration of the K^+ sensor has been carried out by using a reference solution (KCl 10^{-2} M) in direct contact with the electrolyte in a glass well and testing the response of the sensor when solutions with varying concentration of KNO_3 (10^{-7}–10^{-1} M) were used as

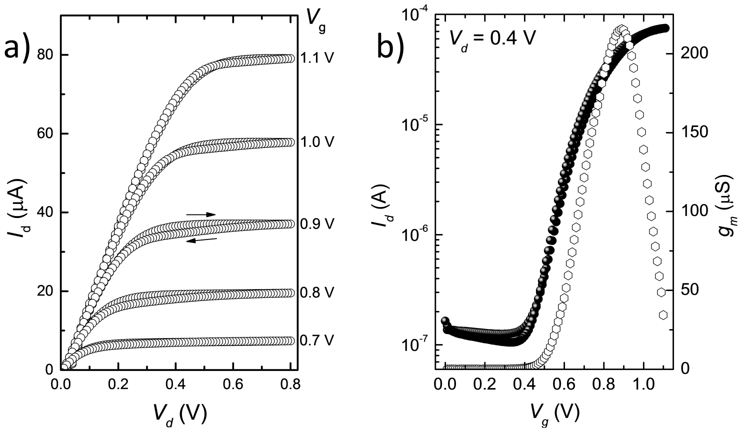

Figure 2.11.: a) Output characteristic and b) transfer characteristic (closed circles) and transconductance (open hexagons) of the ZnO EGT at $V_\mathrm{d} = 0.4\,\mathrm{V}$.

the analyte. The voltages V_g and V_d were maintained at fixed values during the measurements.

To functionalize the ZnO nanoparticles for the glucose sensing, a solution containing a 10 wt % (3-glycidyloxypropyl)-trimethoxysilane (GOPS) solution in 2-propanol was deposited by spin coating onto the ZnO channel and subsequently annealed at 100 °C for 10 min. The layer was then rinsed with 10^{-1} M KCl to remove the excess GOPS. Subsequently, an aqueous solution of glucose oxidase (GOD) was added onto the transistor and left to dry overnight in a fridge at 4 °C to allow the GOPS to bind the GOD. Before the characterization, the sensor was rinsed again with KCl 10^{-1} M, to remove the unattached GOD. Finally, the sensor performances were tested employing aqueous solutions with increasing concentration of GLC (10^{-7}–10^{-1} M) in an electrolyte with fixed salt concentration (10^{-1} M KCl). A Pt gate working as a catalyzer, instead of the Ag/AgCl one, has been used for the measurement of GLC. Again, V_g and V_d were kept at fixed values during the measurements.

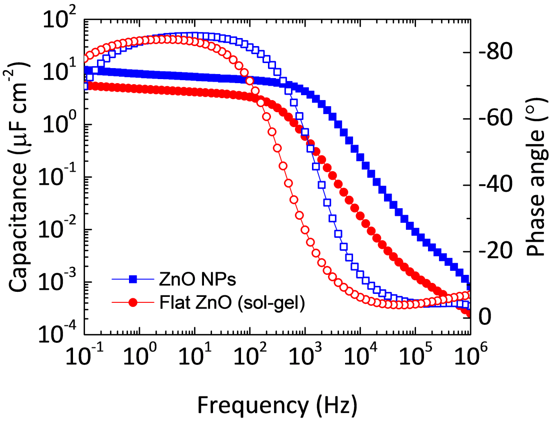

Figure 2.12.: Capacitance (closed symbols) and phase (open symbols) for a flat and a nanoporous ZnO layer.

2.3.3. Results and discussion

The performances of the transistor were evaluated in an aqueous solution of KCl (10^{-1} M) by means of current–voltage measurements and using an Ag/AgCl gate electrode.

The device shows a strong modulation of the current even at low voltages. The threshold voltage V_{th} is as low as 0.57 V, while the current saturates at $V_{\mathrm{g}} = 1.2\,\mathrm{V}$ with an *on/off* ratio reaching values of 10^3. The high current modulation at low voltage is the confirmation that the transistor works in the EGT regime. The transconductance g_{m} reaches a maximum value of 215 µS at $V_{\mathrm{g}} = 0.88\,\mathrm{V}$ (Figure 2.11a and 2.11b). For meaningful comparison with analogue systems the value of the transconductance is often normalized with respect to the channel width W, giving in our case a value of $g_{\mathrm{m}}/W = 107\,\mu\mathrm{S\,mm}^{-1}$. This value is comparable to a value of $800\,\mu\mathrm{S\,mm}^{-1}$ reported for single-crystal, flat ZnO EGTs.[52] These are promising results, given that the performances of the devices are limited by the absence of insulation over the source and drain electrodes, causing current

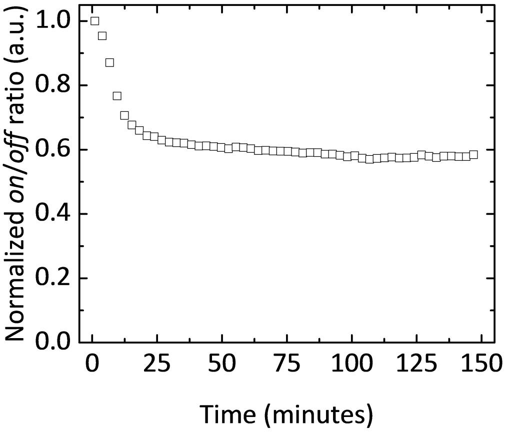

Figure 2.13.: Lifetime of the ZnO EGTs under periodical cycling between the *on* and the *off* states.

leakage between the gate and the source. Moreover, nanoparticulate ZnO layers are expected to contain a large amount of defects, especially at the nanoparticles boundaries, which limit the mobility of the charge carriers. Despite that, the saturation mobility for our transistor is found to be $0.88\,\mathrm{cm^2\,V^{-1}\,s^{-1}}$, in line with the value of $1.61\,\mathrm{cm^2\,V^{-1}\,s^{-1}}$ reported by Hong *et al.* for printed compact ZnO layers gated through a gel electrolyte.[53] The values of the mobility has been calculate using Eq. (2.4), with an EDL capacitance of $C_{\mathrm{dl,np}} = 8.04\,\mathrm{\mu F\,cm^{-2}}$. This value has been extracted by phase/capacitance measurements in the low frequency regime (10 Hz). For comparison, the capacitance of the EDL for a flat ZnO layer has also been measured, obtaining a value of $C_{\mathrm{dl,flat}} = 4.14\,\mathrm{\mu F\,cm^{-2}}$, which confirms the increment of the exposed ZnO surface area (Figure 2.12).

As ZnO is slightly soluble in water, a test to determine the lifetime of the transistor has been performed. In this test, the *on/off* ratio of the EGT has been monitored while V_{g} was cycled between 0 V (*off*) and 0.9 V (*on*, maximum of the transconductance) with a period of 180 s. After 2.5 h the *on/off* ratio was still at the 60 % of its maximum value, indicating a remarkable stability of the transistor in an aqueous environment (Figure 2.13)

Using the setup in Figure 2.9b, the performances of the transistor as an ion sensor have been evaluated using the figure of merit $\Delta I/I_0$, where ΔI is the difference between I_d at a given concentration and the current at “infinite dilution” (10^{-7} M). The concentration of K^+ ions in the analyte has been varied over seven orders of magnitude. The value of $V_\mathrm{g} = 0.7$ V has be chosen to match the interval of highest g_m increase (Figure 2.11b). In the given concentration range, the increase of $\Delta I/I_0$ is 30-fold, while the detection limit of the ion sensor is 4.7×10^{-4} M. This value is somewhat higher than expected, as a detection limit of 1.5×10^{-5} M has been obtained for an analogue sensor with the same ISM formulation.[54] This is likely due to the lack of insulation on the drain and source electrodes, that causes detrimental gate current leakage. Nonetheless, the sensitivity of the sensor in the Nernstian regime, calculated by translating the measured current variation into effective gate voltage variation through the transfer curve, settles at 44.5 mV dec^{-1}, in line with previously reported values. The calibration curve is shown in Figure 2.14.

The sensor itself proved to be rather fast in the detection of the K^+ ions as its response time, estimated as the time needed for the current to reach 90 % of its maximum value, is less than 20 s, independently of the concentration of the solution tested (Figure 2.15). This compares favorably with previously reported sensors based on the same ISM integrated on an organic electrochemical transistor (OECT).[54] The mentioned OECTs rely on the *volumetric* de-doping of an organic *p*-type conductor (PEDOT:PSS) by the K^+ cations, and have response times ranging from 36 s to 74 s, depending on the value of V_g. The selectivity of the ion sensor entirely depends on the formulation and the characteristics of the

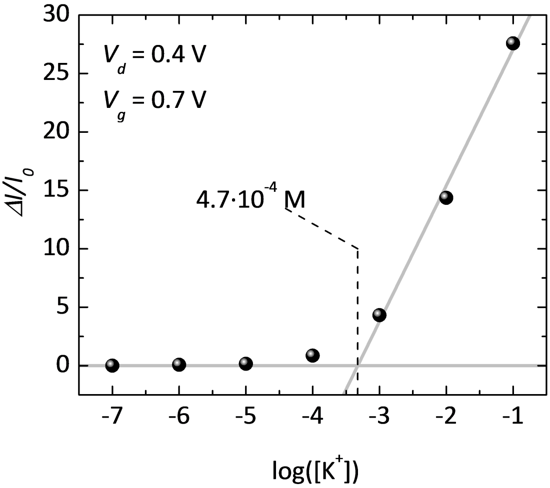

Figure 2.14.: Sensor response as a function of the concentration of K^+ ions, expressed as decades of molar concentration.

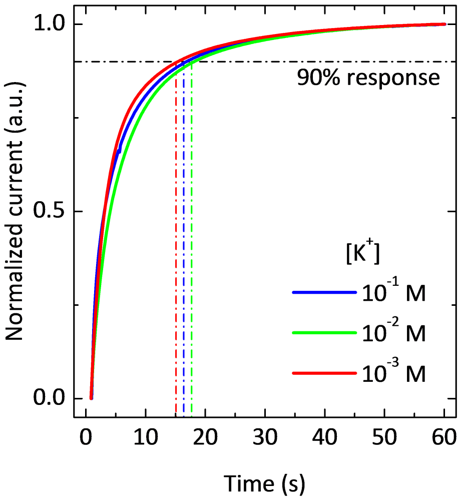

Figure 2.15.: Normalized current response of the ion-selective electrolyte-gated transistor at different concentrations of potassium in water $[K^+]$. The time to reach 90 % of the equilibrium current is highlighted for three different concentrations.

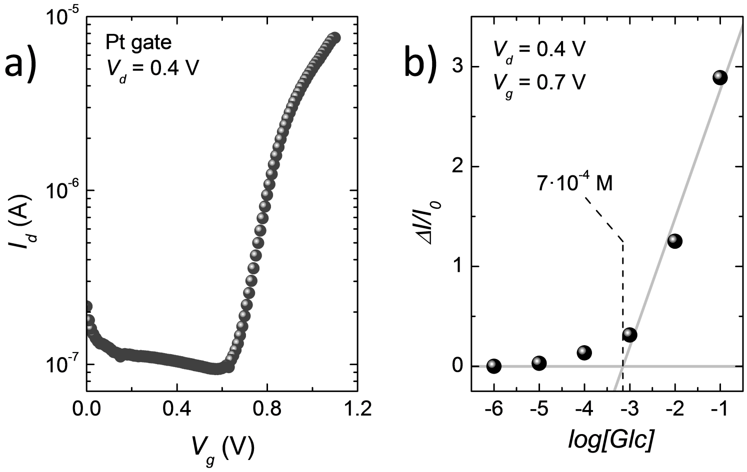

Figure 2.16.: a) Output transfer of the ZnO EGT when driven with a Pt gate and a 10^{-1} M KCl solution as the electrolyte and b) calibration curve of the glucose sensor.

ISM and can be quantified, for example, by the so called *selectivity coefficient*, i.e. the concentration ratio at which the interfering ion (for example, Na^+) and the reference ion generate the same potential difference. In particular, for our ISM the selectivity coefficient has been calculated to be $-\log\left([K^+]/[Na^+]\right) = 2.7$.[54]

For the purpose of building a glucose sensor, the Ag/AgCl gate has been replaced by a Pt wire, as it facilitates the enzymatic reaction that allows the measurement of the glucose concentration in a solution. This change is detrimental for the performances of the transistor as such because Pt, besides being a polarizable electrode, has a higher work function with respect to Ag/AgCl. As a consequence, the *on/off* ratio of the transistor decreased in one order of magnitude and the threshold voltage increased up to $V_{\text{th}} = 0.66\,\text{V}$ (Figure 2.16a). Nonetheless, the transistor was capable to sense the glucose content with a linear response in a range from 7×10^{-4} M (detection limit) to 10^{-1} M, which overlaps the range of glucose content in human blood for healthy people (4×10^{-3}–8×10^{-3} M) and in patients with diabetes (2×10^{-3}–3×10^{-2} M).[55] The overall increment of the current is only 3-fold, probably due to the reduced *on/off* ratio (Figure 2.16b).

2.3.4. Conclusions

We have demonstrated an EGT prepared by simple solution processing of commercial ZnO nanoparticles. The transistor showed a remarkable 10^3 *on/off* ratio. The device was able to work in an aqueous environment for over 2.5 h and to reach the saturation regime at a voltage compatible with the electrochemical window of the water (< 1.2 V). In agreement with analogue measurements on EGTs based on compact ZnO layers, the calculated electron mobility is $0.88\,\mathrm{cm^2\,V^{-1}\,s^{-1}}$. Through the integration of an ion selective membrane, a device capable of sensing K^+ ion with good sensitivity over a wide range of concentrations has been fabricated. To show the versatility of this approach for biological sensing, a proof of concept glucose sensor has been fabricated by a simple functionalization of the ZnO semiconductor. The sensor is capable of measuring the content of glucose in a range compatible with that in human blood. This work demonstrates the potential of metal oxide-based EGTs as platform for future development of inexpensive and disposable ion and biological sensors.

2.4. Contribution of the author

E. Bandiello, M. Sessolo, H. J. Bolink, "*Aqueous electrolyte-gated ZnO transistors for environmental and biological sensing*". Journal of Materials Chemistry C, 2014, **2**, 10277-10281. DOI: 10.1039/C4TC02075H

Reproduced by permission of The Royal Society of Chemistry

Journal of
Materials Chemistry C

COMMUNICATION

Cite this: *J. Mater. Chem. C*, 2014, **2**, 10277

Received 15th September 2014
Accepted 17th October 2014

DOI: 10.1039/c4tc02075h

www.rsc.org/MaterialsC

Aqueous electrolyte-gated ZnO transistors for environmental and biological sensing†

E. Bandiello, M. Sessolo* and H. J. Bolink

Electrolyte-gated transistors (EGTs) based on ZnO thin films, obtained by solution processing of suspensions of nanoparticles, have a low turn-on voltage (<0.5 V), a high on/off ratio and transconductance exceeding 0.2 mS. Importantly, the ZnO surface can be functionalized with a large variety of molecular recognition elements, making these devices ideal transducers in physiological and environmental monitoring. We present simple glucose-sensing and ion-selective EGTs, demonstrating the versatility of such devices in biosensing.

The development of simple yet reliable sensors for the identification of biomolecules, pathogens, ions and pollutants has become a primary research challenge due to the expected widespread application and integration of sensors in our society and environment.[1–3] One illustrative example is the glucose sensor which, despite being commercially available for the past 25 years, is still attracting considerable research efforts because of the demand for low-cost and reliable methods for the self-monitoring of blood glucose.[4–6] While the commonly applied transduction mechanisms are mostly electrochemical or optical,[7,8] the application of field-effect transistors (FETs) to biosensing has gained increasing attention due to the intrinsic signal amplification of such devices.[9,10] From the perspective of their low-cost and simple manufacturing process, the organic thin-film transistors represent the most promising candidates for such applications, thanks also to the unique possibility of tuning the properties of the organic semiconductor through rational chemical design.[11–13] A limited number of examples exist of conjugated molecular materials that are stable in an aqueous environment.[14,15] Metal oxides represent a possible alternative as the semiconductor in biosensing applications. They have high carrier mobilities,[16] easiness of surface functionalization,[17,18] and can be processed by simple solution methods, leading to inexpensive devices, even on flexible substrates.[19,20] Unlike most organic semiconductors, metal oxide semiconductors are usually stable in air and in water, an essential prerequisite for sensor devices working in an aqueous or physiological environment. A type of transistor which is especially suited for biosensing is the electrolyte-gated transistor (EGT). The working principle of EGTs is analogous to that of traditional FETs, in which the gate insulator (usually a solid high-κ dielectric) is replaced by a convenient electrolyte (solid, liquid or gel).[21,22] The variation of the conductivity of the channel with the gate voltage (V_g) is determined by the capacitance of the nanometrically thin electrical double layer (EDL) that forms at the interface between the electrolyte and the semiconductor channel as a consequence of the ionic displacement. The capacitance of an EDL can be orders of magnitude larger compared to that of traditional insulators, and for this reason EGTs usually show high transconductance (g_m) at very low voltages.[21] A few recently reported examples of EGTs employing semiconducting metal oxides thin films suggest that such devices can have performances superior to the associated FET, and show how they could even be used in the development of bio-sorbable, implantable devices.[23,24] A unique feature of metal oxides is that it is possible to obtain stable nanoparticle (NP) dispersions from them, which can be casted forming nanostructured thin films with enhanced surface area and tunable properties. Taking advantage of the unique properties of metal oxides and EGTs, in this paper we present aqueous EGTs employing solution processed ZnO NPs as the semiconducting material. The high surface area of the nanostructured channel further enhances the EDL capacitance and allows the saturation of the drain current (I_d) at V_g as low as 1.1 V. What makes EGTs ideal candidates for sensing applications is that the drain current is influenced by any physical or chemical modification of the EDL. As a proof of principle, we demonstrate the potential of these devices by presenting ion-selective EGTs, realized through the integration of an ion-selective membrane (ISM) into the device architecture, as well

---

Instituto de Ciencia Molecular (ICMOL), Universidad de Valencia, 46980 Paterna, Valencia, Spain. E-mail: michele.sessolo@uv.es

† Electronic supplementary information (ESI) available: TGA, time response of the ion-selective transistors and capacitance measurements. See DOI: 10.1039/c4tc02075h

as simple enzymatic glucose sensors, obtained by the covalent binding of the enzyme to the ZnO surface.

The EGTs were prepared on glass slides with pre-patterned indium tin oxide (ITO) source–drain electrodes, with a channel width (W) and length (L) of 2 mm and 20 μm, respectively ($W/L = 100$, Fig. 1a). The ITO/glass substrates were cleaned by chemical and plasma methods. Commercially available ZnO NPs in suspension in ethanol (5 wt%) were filtered through a 0.22 μm PTFE membrane and spin-coated onto the substrates. The layers were subsequently annealed at 450 °C for 30 minutes in order to remove the stabilizing ligands (Fig. S1†). The final thickness of the layers was about 60 nm. In spite of the high annealing temperature, the ZnO surface shows a high porosity (Fig. 1b), with the grain size resembling the average particle size of the suspension (<35 nm). The grazing incident X-ray diffraction (GIXRD) pattern confirms a high degree of crystallinity of the nanostructured film. Moreover, the crystal size estimated from signal broadening on the (101) direction is 35 nm, which is consistent with morphological measurements and manufacturer's datasheet. Glass wells, used to confine the electrolyte, were integrated onto the transistor array using a thin layer of polydimethylsiloxane (PDMS). An Ag/AgCl pellet electrode or a platinum wire immersed in the electrolyte were used as transistor gate electrodes.

The performance of the transistors was evaluated in aqueous electrolyte (KCl 0.1 M) using a porous Ag/AgCl pellet as the gate electrode (Fig. 2). The output characteristics at five different gate voltages are reported in Fig. 2a. The device shows a high modulation of the current, both in the linear and saturation regimes, with large saturation currents of >75 μA at very low driving voltages ($V_g = 1.1$ V, $V_d > 0.5$ V). A turn on voltage (V_{on}) of only 0.4 V is observed from the transfer curve measured at $V_d = 0.4$ V (Fig. 2b), with a corresponding threshold voltage of $V_{th} = 0.57$ V and a current on/off ratio of about 10^3. The high current modulation at very low voltages is the hallmark of EGTs, and can be quantified by the device transconductance $g_m = \partial I_d/\partial V_g$. The maximum $g_m = 215$ μS was obtained for $V_g = 0.88$ V (Fig. 2b), giving a normalized transconductance per channel width of $g_m/W = 107$ μS mm^{-1}, which compares favorably to the values reported for atomically flat, single crystal ZnO EGTs (~800 μS mm^{-1}).[25] It is important to point out that the device performances are limited by the absence of insulation between the ZnO-NP films and the electrolyte in the area surrounding the channel. Moreover, nanostructured films, when compared to poly-/mono-crystalline layers, will suffer from reduced charge mobility due to the intrinsically high defect concentrations. In spite of these limitations, the ZnO-NP EGT performs favorably and exhibits a saturation electron mobility of 0.81 cm^2 V^{-1} s^{-1} (calculated using the EDL capacitance $C_{dl} = 8.04$ μF cm^{-2}, ESI†), in agreement with values obtained using compact ZnO thin films gated through ion-gel dielectrics.[26] The capacitance of the EDL for the nanostructured ZnO almost doubles that of a flat ZnO layer ($C_{dl} = 4.14$ μF cm^{-2}), confirming the enhancement effect of the increased surface area (ESI, Fig. S2†).

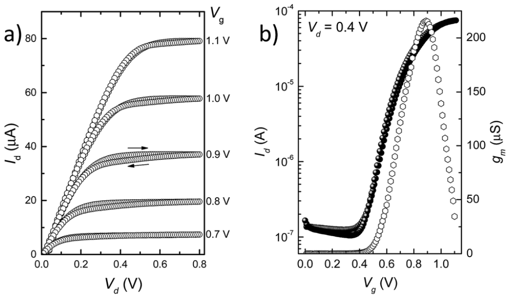

Fig. 2 (a) The output characteristics of the EGTs in aqueous electrolyte with V_g varying from 0.7 V to 1.1 V with a step of 0.1 V. (b) The transfer curve for $V_d = 0.4$ V (full circles) with the associated transconductance (empty hexagons).

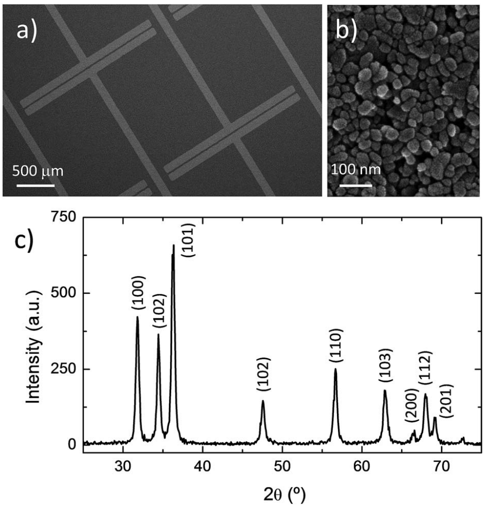

Fig. 1 SEM images of (a) the transistor array with visible ITO source–drain electrodes and (b) the detailed ZnO nanostructured surface. (c) The GIXRD pattern with Cu Kα_1 radiation ($\lambda = 1.54056$ Å) of the thin films.

The remarkable device performance in water-based electrolytes makes the ZnO NP-based EGTs attractive elements for sensors working in an aqueous environment. Since the working principle of these devices is based on the displacement of cations in the proximity of the metal oxide surface, their use as ion sensors is the most obvious direct application. Ion-selective EGTs were prepared by integrating a polymer ISM doped with a potassium ionophore, using an architecture recently described for electrochemical transistors based on both semiconducting and conducting polymers.[27,28] The device structure (Fig. 3a) consists of a reference electrolyte (KCl 10^{-2} M) in contact with the ZnO channel, separated from the analyte by the ISM. The ISM consists of a polyvinylchloride matrix containing a plasticizer, an anionic exchanger and the potassium ionophore III. As previously detailed, the solution containing the ISM

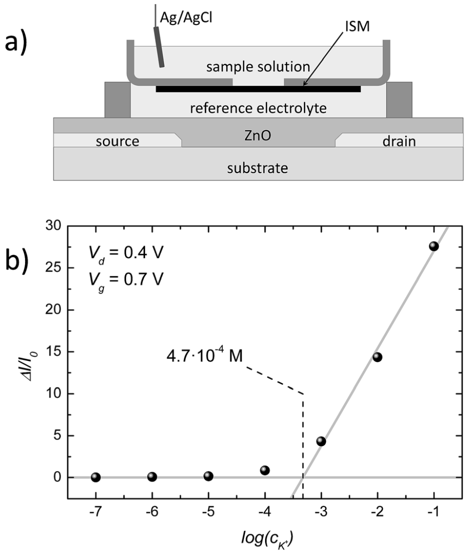

Fig. 3 (a) A schematic of the device architecture used in the preparation of the ion-selective EGTs. (b) The device response as a function of the c_{K^+} expressed in decades of molar concentration.

components was drop-casted onto a glass substrate and, after drying, the obtained membrane was transferred onto the EGT array.[28] Changes in the K^+ concentration (c_{K^+}) in the sample shift the potential at the electrolyte/membrane interfaces and the resulting electric field drops onto the channel modulating its conductivity.[29] Stock solutions with increasing K^+ concentrations were exchanged in the upper chamber while monitoring the consequent variation of the current I_d. Fig. 3b shows the response of the transistor, $\Delta I/I_0$ (with ΔI being the difference between I_d at a given concentration and I_0, the current at infinite dilution), for c_{K^+} spanning 7 orders of magnitude. The response of the device was measured 60 s after injection with the saline solution, but we observed that at least 90% of the current response was reached in less than 20 s (Fig. S2†). The IS-EGTs are capable of sensing K^+ with a detection limit of $c_{K^+} = 4.7 \times 10^{-4}$ M and with a thirty-fold increase in the current for the concentration range $10^{-4} \leq c_{K^+} \leq 10^{-1}$ M. The detection limit was estimated as the cross point between the slope of the dataset and a line corresponding to the noise level of the device (I_d at a low K^+ concentration). It is important to emphasize again that the ZnO film exposed to the electrolyte is not restricted solely to the channel area, leading to a detection limit which is somewhat higher compared to what is expected by using this particular ISM formulation.

Through the precise patterning of the channel together with insulation of the ITO contacts and interconnects, we expect the device to show a sensitivity and detection limit in agreement with similar ion-sensing structures.[28] A key advantage of metal oxides over conducting polymers or molecular semiconductors is that it is possible to tune their properties as well as introduce tailored functionalities by direct surface modifications.[30] As in most metal oxides, the surface of ZnO is rich in –OH groups, which can be readily functionalized by electrostatic or covalent bonding of virtually any type of molecule.[31] For these reasons, ZnO has been widely used as an electroactive substrate in the preparation of amperometric enzymatic sensors.[32] As a proof of principle, we prepared simple glucose-sensing EGTs by covalent binding of the enzyme glucose oxidase (GOD) onto the ZnO NPs' surface. GOD was grafted onto the metal oxide by using (3-glycidyloxypropyl)-trimethoxysilane (GOPS) as the covalent linker. The methoxysilane functionality of the GOPS binds onto the ZnO surface, while the epoxide group allows the formation of a secondary amine bond with the enzyme (Fig. 4a).[33,34] A 10 wt% GOPS solution in isopropanol (iPrOH) was deposited by spin coating onto the ZnO channel and annealed at 100 °C for 10 minutes. The layer was subsequently rinsed with 0.1 M KCl in water to remove the excess of unbound GOPS. Afterwards, an aqueous GOD solution was added onto the transistor and was allowed to dry at RT overnight. Before the device characterization was carried out, the functionalized ZnO films were rinsed gently with 0.1 M KCl in water to remove any excess of unattached GOD. For the sensor characterization, a Pt wire was used as the gate electrode in order to avoid the necessity of adding a redox mediator.[4] We observed an increased V_{th} of 0.83 V and a reduction of the on/off ratio to about 2 orders of magnitude (Fig. 4b), in accordance with the increased electrode work function of Pt.[35] In this case, the achievement of the current

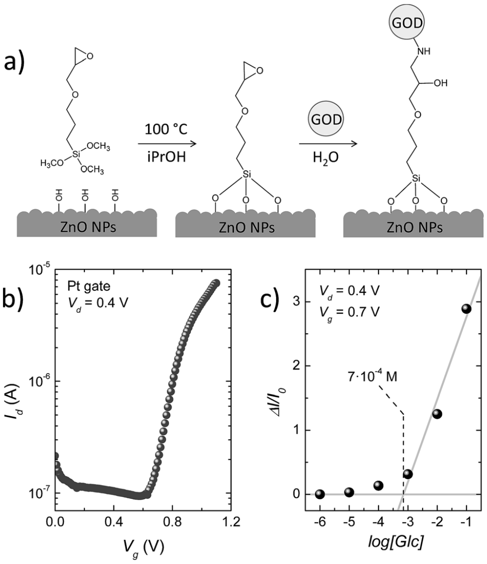

Fig. 4 (a) The reaction scheme for the functionalization of the ZnO NPs' surface with the enzyme GOD. (b) The transfer curve of the GOD-functionalized EGTs employing a Pt gate electrode. (c) The device response to increasing glucose concentration, expressed in decades of molar concentration.

saturation (and thus higher on/off ratio) is limited by the electrochemical window of water. The current response $\Delta I/I_0$ of the sensor was measured 60 s after the injection with stock 0.1 M KCl aqueous solutions with increasing D-glucose concentrations [Glc], and is reported in Fig. 4c.

The operation of the device as a glucose sensor confirms that the biological activity of the enzyme is preserved after its covalent bonding onto the ZnO NPs. The functionalized EGT is capable of sensing Glc in the concentration range of $10^{-4} \leq$ [Glc] $\leq 10^{-1}$ M, with the highest sensitivity (slope of the response curve) above 10^{-3} M, which matches the physiological concentration of glucose in humans (1–20 mM).[4] The corresponding detection limit, calculated as in the case of the ion-selective transistor, is 7×10^{-4} M. As a final test, we evaluated the overall stability of the EGT by continuously cycling it between $V_g = 0$ V and $V_g = 0.9$ V (maximum of transconductance) at $V_d = 0.4$ V. The on/off ratio readily reaches and stabilizes at 60% of its maximum value for at least 2.5 h (ESI, Fig. S4†), indicating a remarkable lifetime of the aqueous electrolyte-gated ZnO transistor.

Conclusions

In summary, we have presented electrolyte-gated transistors (EGTs) prepared by a simple solution processing of commercial ZnO NP suspension. The device can work in an aqueous environment at biases as low as 1 V, and shows electron mobility of 0.81 $cm^2 V^{-1} s^{-1}$. Of great importance is the versatility of such devices for the realization of a variety of biosensors. Ion-selective membranes can be integrated with the electrolyte-gated transistors leading to sensitive ion sensors capable of determining K^+ concentration over a wide range of concentrations. In addition to this, ZnO is an extraordinary platform for further chemical modifications, since virtually any type of chemical transducer (electrochemical and even optical) can be bonded onto its surface leading to a variety of different functionalities. Through the use of an alkoxysilane functional group, we covalently attached glucose oxidase to the surface of the transistor channel, resulting in a simple sensor for the physiological monitoring of glucose. These results clearly show the potential of metal oxide electrolyte-gated transistors in environmental and biomedical applications, and pave the way for a new generation of low-cost, disposable and even flexible biosensors.

Acknowledgements

This work has been supported by the European Union (HYSENS, Grant STRP 263091), the Spanish Ministry of Economy and Competitiveness (MINECO) (MAT2011-24594), and the Generalitat Valenciana (Prometeo/2012/053). E. B. acknowledges MINECO for an FPI grant. The authors thank Jorge Ferrando and Alejandra Soriano for technical assistance in the characterization of the transistors and XRD measurements.

Notes and references

1 A. Milenković, C. Otto and E. Jovanov, *Comput. Commun.*, 2006, **29**, 2521–2533.
2 A. Pantelopoulos and N. G. Bourbakis, *IEEE Trans. Syst. Man Cybern. C Appl. Rev.*, 2010, **40**, 1–12.
3 V. Velusamy, K. Arshak, O. Korostynska, K. Oliwa and C. Adley, *Biotechnol. Adv.*, 2010, **28**, 232–254.
4 A. Heller and B. Feldman, *Chem. Rev.*, 2008, **108**, 2482–2505.
5 E. H. Yoo and S. Y. Lee, *Sensors*, 2010, **10**, 4558–4576.
6 Y. Wang and M. Hu, in *Detection Challenges in Clinical Diagnostics*, The Royal Society of Chemistry, 2013, pp. 65–88, DOI: 10.1039/9781849737302-00065.
7 S. Scarano, M. Mascini, A. P. F. Turner and M. Minunni, *Biosens. Bioelectron.*, 2010, **25**, 957–966.
8 N. J. Ronkainen, H. B. Halsall and W. R. Heineman, *Chem. Soc. Rev.*, 2010, **39**, 1747–1763.
9 P. Bergveld, *Sens. Actuators, B*, 2003, **88**, 1–20.
10 K. I. Chen, B. R. Li and Y. T. Chen, *Nano Today*, 2011, **6**, 131–154.
11 M. E. Roberts, A. N. Sokolov and Z. Bao, *J. Mater. Chem.*, 2009, **19**, 3351–3363.
12 P. Lin and F. Yan, *Adv. Mater.*, 2012, **24**, 34–51.
13 L. Torsi, M. Magliulo, K. Manoli and G. Palazzo, *Chem. Soc. Rev.*, 2013, **42**, 8612–8628.
14 O. Knopfmacher, M. L. Hammock, A. L. Appleton, G. Schwartz, J. Mei, T. Lei, J. Pei and Z. Bao, *Nat. Commun.*, 2014, **5**, 2595.
15 D. Khodagholy, J. Rivnay, M. Sessolo, M. Gurfinkel, P. Leleux, L. H. Jimison, E. Stavrinidou, T. Herve, S. Sanaur, R. M. Owens and G. G. Malliaras, *Nat. Commun.*, 2013, **4**, 2133.
16 M.-G. Kim, H. S. Kim, Y.-G. Ha, J. He, M. G. Kanatzidis, A. Facchetti and T. J. Marks, *J. Am. Chem. Soc.*, 2010, **132**, 10352–10364.
17 D. Weber, S. Botnaraş, D. V. Pham, J. Steiger and L. De Cola, *J. Mater. Chem. C*, 2013, **1**, 3098.
18 M. M. Rahman, A. J. Ahammad, J. H. Jin, S. J. Ahn and J. J. Lee, *Sensors*, 2010, **10**, 4855–4886.
19 S. R. Thomas, P. Pattanasattayavong and T. D. Anthopoulos, *Chem. Soc. Rev.*, 2013, **42**, 6910–6923.
20 Y. Sun and J. A. Rogers, *Adv. Mater.*, 2007, **19**, 1897–1916.
21 S. H. Kim, K. Hong, W. Xie, K. H. Lee, S. Zhang, T. P. Lodge and C. D. Frisbie, *Adv. Mater.*, 2013, **25**, 1822–1846.
22 T. Fujimoto and K. Awaga, *Phys. Chem. Chem. Phys.*, 2013, **15**, 8983–9006.
23 A. Al Naim and M. Grell, *Appl. Phys. Lett.*, 2012, **101**, 141603.
24 L. Torsi, M. Singh, G. Palazzo, G. Romanazzi, G. P. Suranna, N. Ditaranto, C. Di Franco, M. V. Santacroce, M. Y. Mulla, M. Magliulo and K. Manoli, *Faraday Discuss.*, 2014, DOI: 10.1039/c4fd00081a.
25 H. Yuan, H. Shimotani, A. Tsukazaki, A. Ohtomo, M. Kawasaki and Y. Iwasa, *Adv. Funct. Mater.*, 2009, **19**, 1046–1053.
26 K. Hong, S. H. Kim, K. H. Lee and C. D. Frisbie, *Adv. Mater.*, 2013, **25**, 3413–3418.

27 K. Schmoltner, J. Kofler, A. Klug and E. J. W. List-Kratochvil, *Adv. Mater.*, 2013, **25**, 6895–6899.

28 M. Sessolo, J. Rivnay, E. Bandiello, G. G. Malliaras and H. J. Bolink, *Adv. Mater.*, 2014, **26**, 4803–4807.

29 E. Bakker, P. Bühlmann and E. Pretsch, *Chem. Rev.*, 1997, **97**, 3083–3132.

30 M. A. Neouze and U. Schubert, *Monatshefte fur Chemie*, 2008, **139**, 183–195.

31 Y. Zhang, T. R. Nayak, H. Hong and W. Cai, *Curr. Mol. Med.*, 2013, **13**, 1633–1645.

32 X. Shi, W. Gu, B. Li, N. Chen, K. Zhao and Y. Xian, *Microchim. Acta*, 2014, **181**, 1–22.

33 X. Strakosas, M. Sessolo, A. Hama, J. Rivnay, E. Stavrinidou, G. G. Malliaras and R. M. Owens, *J. Mater. Chem. B*, 2014, **2**, 2537–2545.

34 D. Jung, C. Streb and M. Hartmann, *Int. J. Mol. Sci.*, 2010, **11**, 762–778.

35 L. Kergoat, L. Herlogsson, B. Piro, M. C. Pham, G. Horowitz, X. Crispin and M. Berggren, *Proc. Natl. Acad. Sci. U. S. A.*, 2012, **109**, 8394–8399.

3. Lithium Salts Additives for Light-Emitting Electrochemical Cells

3.1. Light-emitting electrochemical cells

This section serves as a brief introduction to the structure and the main features of light-emitting electrochemical cells (LECs), in particular to their peculiar working mechanism and the state-of-the-art methods to enhance their performances. The focus will be on LECs based on ionic transition metal complexes (iTMCs), as they have been the subject of the research presented in this work.

LECs are luminescent devices consisting, generally, of a single thin film of an electroluminescent material (typically $\approx 100\,\mathrm{nm}$) sandwiched between two electrodes, one of which is transparent (see Figure 3.1a). The electroluminescent material in LECs is either ionic, as for LECs based on iTMCs,[56–58] or it can consist of a neutral polymer semiconductor or organic small-molecules to which ionic species are added. Typical additives are *ionic liquids* (ILs), which are salts with a low melting point.[59] iTMCs are mostly positively charged complexes whose charge is compensated by anions such as PF_6^- or BF_4^- (Figure 3.2a).

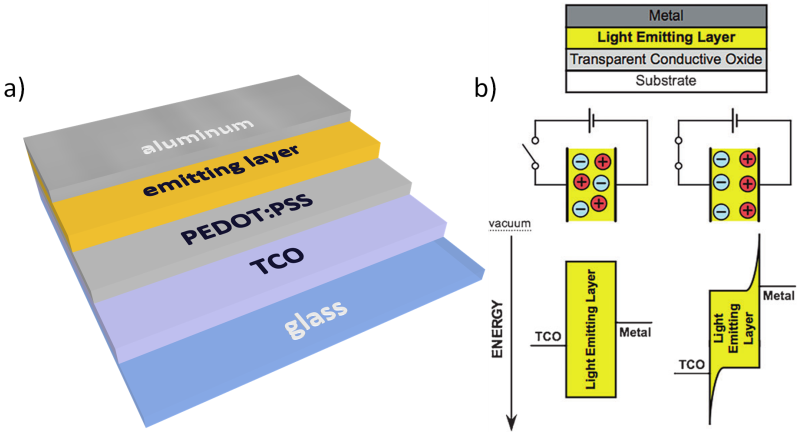

Figure 3.1.: a) Structure of a LEC and b) schematic working principle[2].

iTMCs are attractive materials for LECs, as they can simultaneously perform the transport of holes/electrons. This occurs by the subsequent and reversible oxidation/reduction of neighboring molecules. Upon recombination of an electron and a hole, an exciton is generated on the iTMC, which then relaxes under the emission of a photon. Importantly, iTMCs are phosphorescent emitters, hence intrinsically more efficient as compared to fluorescent materials such as conjugated polymers. Several metal centers such as on Ru^{3+}, Os^{3+}, Ir^{3+} and Cu^{2+} have been studied as electroluminescent materials in LECs,[60–63] with the most efficient ones being by far those based on Ir^{3+}.[2,58] Despite iTMCs being intrinsically ionic materials, often ILs (Figure 3.2b) are also added in order to enhance the devices' performances.[4]

The working principle of LECs is based on the presence of mobile ions in the active layer, which can be displaced by an electric field and accumulate close to the respective electrodes (anions near to the anode, cations near to the cathode). At these interfaces, electrical double layers (EDLs) are formed, which lower the

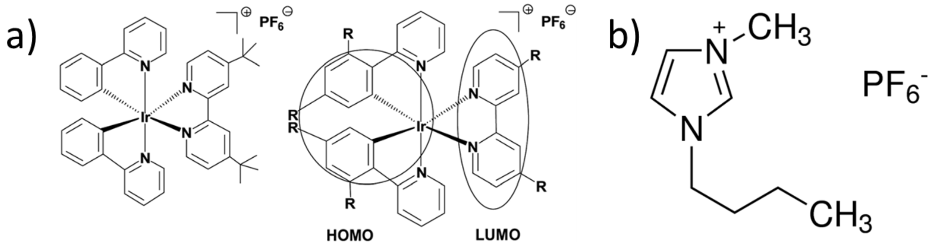

Figure 3.2.: a) Chemical structure of a typical Ir-iTMC, bis(2-phenylpyridine)(4,4-di-*tert*-butyl-2,20-dipyridyl)-iridium(III) hexafluorophosphate, with the spatial localization of the HOMO and the LUMO levels[58] and b) structure of the most commonly used ionic liquid, 1-butyl-3-methylimidazolium hexafluorophosphate.

energy barrier for the injection of electrons and holes (Figure 3.1b). When the barriers are overcome holes and electrons are injected into the HOMO and the LUMO of the electroluminescent material, respectively, and they can recombine radiatively when they, after transport, meet on a single site. As anticipated in the Section 1.1, two modes of operation have been proposed for LECs, both predicting the formation of the EDLs as an effect of the applied bias, but with a very different potential drop distribution:

- The *electrodynamical model* (ED), in which holes and electrons, once injected, diffuse into the field-free bulk of the electroluminescent layer, where they can recombine. In this model, the potential drops only at the EDLs and the electric field in the bulk is zero. The electronic carriers in the bulk are compensated by a different local concentration of anions and cations.[64–68]

- The *electrochemical model* (EC), in which the potential drops partially at the EDLs only to allow ohmic charge injection. After that, electrons (holes) in the bulk are compensated by cations (anions), forming an *n*- and a *p*-doped region, respectively. These doped zones, which facilitate the trans-

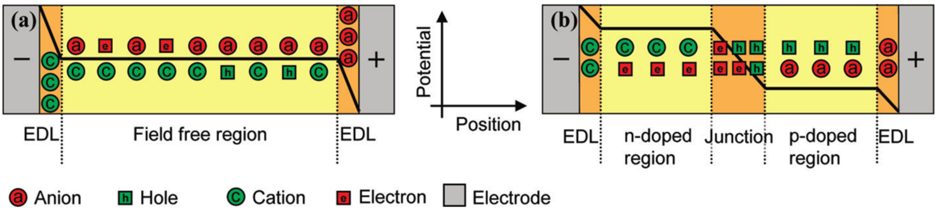

Figure 3.3.: Proposed operating modes of LECs: a) electrodynamical model and b) electrochemical model.[6]

port of the injected charges, are physically separated by an intrinsic zone, where the potential drops and where electron and the hole recombine radiatively.[69–72]

Both theoretical models, schematically shown in Figure 3.3, are partially in agreement with the experimental data, hence a long-standing debate took place in the scientific community about the “true” model explaining the operation of LECs. Recently, van Reenen and coworkers showed that both models actually coexist, meaning that LECs operate in one mode or the other according to the character of the interfaces between the electroluminescent material and the electrodes. For nearly-ohmic contacts (non-injection limited contacts), where the energy barrier for the charge injection is sufficiently small, LECs operate in the electrochemical regime, while injection-limited devices are better described by the electrodynamical model. Importantly, LECs initially operating in the EC mode can show a slow transition to the ED regime due to side electrochemical reactions or oxidation of the electrodes.[6]

As mentioned in Section 1.1, the attractiveness of LECs comes from its simplicity and enhanced robustness towards processing and air. This implies that they can be produced at a lower cost than OLEDs, opening new markets that are difficult to address by the latter. LECs are single-layer devices that can be fabricated by simple solution processes, whereas efficient OLEDs require slow and expensive multi-step, vacuum deposition methods. In addition, in OLEDs the mandatory presence of low work function cathodes requires a rigorous device encapsulation, in order to avoid the oxidation of the metal when exposed to air/humidity. This requirement is less demanding for a LEC, as its working mechanism makes it only weakly dependent on the work function of the electrodes, thus allowing the use of stable metals for this purpose.

The main disadvantages of LECs over OLEDs are their efficiencies and overall lifetime. Moreover, relying on the ionic conductivity of the electroluminescent layer, the turn-on time of LECs is dictated by the time needed for the ions to form the EDLs at the interface with the electrodes. When driven at a constant voltage, the turn-on process can be considerably slow, from many minutes to hours. To overcome this issue various techniques have been adopted, many of which rely on improving the ionic conductivity of the active layer, especially in iTMC LECs: the addition of ionic liquids to increase the amount of mobile ions,[4] the inclusion of inert polymers to facilitate the ionic transport[73] or the use of higher voltages to speed-up the charge redistribution. The downside of these approaches is that a higher ionic conductivity implies a faster growth of the EDLs or of the doped regions, which reduces the thickness of the recombination zone and leads to a faster degradation of the device. Hence, when driven under constant bias, a low turn-on time and a long lifetime for a LEC are mutually exclusive.[74]

In 2012 Tordera *et al.* developed a strategy to overcome this issue by employing a pulsed-current driving scheme, which allows for both a fast turn-on and a long lifetime for LECs based on an iTMC with an added ionic liquid. Using rectangular current waves with 1 kHz frequency and 30 % duty cycle, they were able to fabricate devices with high luminance ($> 600\,\mathrm{cd\,m^{-2}}$), sub-second turn-

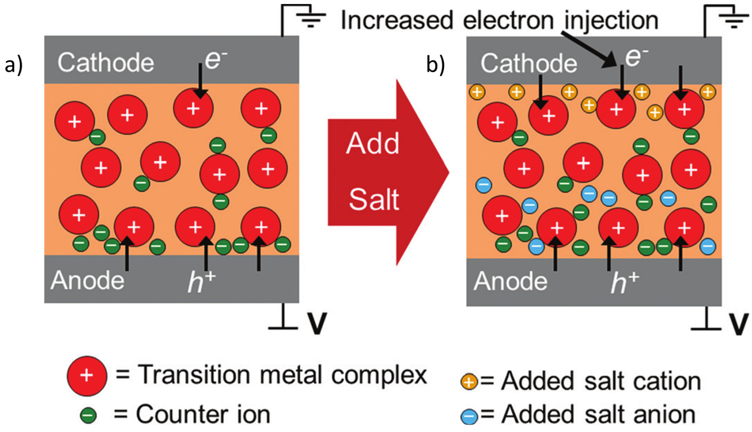

Figure 3.4.: Different ionic density at the cathode for a) a pristine LEC (iTMC only) and b) a LEC iTMC + ionic additive.[5]

on time, and lifetime exceeding 4000 h. In practice, the fast turn-on results from an initial high voltage bias, which allows for a fast redistribution of the mobile ions. On the other hand, the long lifetime is due to the stabilization of the doped zones: the ions drift toward the respective electrodes when a positive current is imposed on the device, while the system relaxes during the rest of the cycle, when no current is applied.[75] More recently, Shen *et al.* hypothesized that the low lifetime and poor luminance often observed for LECs employing additive-free iTMCs, are caused by the unbalanced injection of electrons and holes, which would displace the recombination zone towards the cathode, where quenching occurs. As iTMCs are salts with a bulky, virtually non-mobile cation and a relatively small anion, the accumulation of anions near the anode is much more efficient compared to that of the cations at the cathode. The hole injection is thus favored, leading to the aforementioned effects. It has to be noted that the most commonly used ionic liquids for LECs suffer of this same asymmetry between the sizes of the cation and the anion, even if perhaps to a lesser extent (Figure 3.2b).

A successful strategy to address this problem is the addition of salts with more balanced size-ratio between the cation and the anion (Figure 3.4). In particular, iTMC-LECs with added lithium hexafluorophosphate ($LiPF_6$) show impressive luminance and turn-on time with respect to a pure-iTMC LEC, at the cost of a only slightly reduced lifetime.[5] An analogue result was obtained for polymer LECs, where inorganic salts with matching anion/cation sizes were added to the electroluminescent material, confirming the validity of this approach.[76]

The following are the most common figures of merit used in the characterization of LECs:

The maximum luminance, $L_{\max}$. Measured in $\mathrm{cd\,m^{-2}}$, quantifies the intensity of the electroluminescence.

The turn-on time. This parameter is usually defined as the time $t_{\max}$ to reach $L_{\max}$ after biasing the device. For convenience and ease of comparison, the value t_{100}, defined as the time to reach a luminance of $100\,\mathrm{cd\,m^{-2}}$, can also be used. The latter definition will be used in this work.

The lifetime of the LEC. This is usually defined as the time $t_{1/2}$ for the luminance to reach $1/2 L_{\max}$. The lifetime directly relates with the device stability.

The efficacy. Measured in $\mathrm{cd\,A^{-1}}$, is defined as the luminance divided by the current density.

The power conversion efficiency (PCE). Measured in lumens per watt, $\mathrm{lm\,W^{-1}}$, this parameter takes into account the wavelength of emission as well as the power consumption of the device.

3.2. Influence of lithium salt counterion on the performances of light-emitting electrochemical cells

In the following sections, the performances of iTMC-LECs with different lithium salts additives are presented and discussed. The anions of the lithium salts appear to have a major impact both on the turn-on time and lifetime of the device. In particular, lithium tetrafluoroborate $LiBF_4$ enlarges the lifetime of a pristine LEC (additive-free) about 40 times, resulting in a remarkable lifetime of about 2000 h.

3.2.1. Introduction

In the aforementioned work by Shen and coworkers the beneficial effect of some inorganic hexafluorophosphate salts on the behavior of Ir-TMC-LECs has been demonstrated.[5] The LECs, employing a thin layer of lithium fluoride (LiF) to facilitate the electron injection, were driven at a constant current density $J = 500\,\mathrm{A\,m^{-2}}$. Some of the additives, namely ammonium hexafluorophosphate (NH_4PF_6) and potassium hexafluorophosphate (KPF_6) show an improved lifetime and maximum luminance $L_{\max}$ at the expense of the turn-on time $t_{\max}$, while the addition of $LiPF_6$ substantially increases the luminance and the quantum efficiency of the device (emitted photons per electron) compared that of the pristine LEC. Moreover, after a soft heat-treatment of the iTMC-$LiPF_6$ solution before the deposition (65 °C, 10 min), which improves the dissociation of the lithium salt, the turn-on of the LECs with $LiPF_6$ decreases from 50 h to only 10 s. The authors concluded that, due to a more balanced carrier injection, hexafluorophosphate additives and in particular $LiPF_6$, can greatly improve the

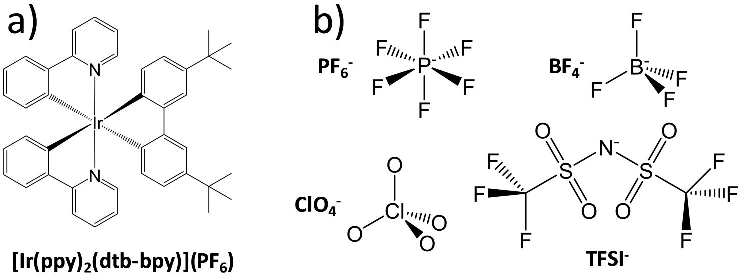

Figure 3.5.: a) $[Ir(ppy)_2(dtb\text{-}bpy)]^+(PF_6)^-$ iTMC complex and b) counterions of the lithium salts used in this study.

luminance of LECs. Nonetheless, the very large luminance span and the use of t_{max} as a characterizing parameter make difficult a meaningful comparison of the performances of these devices. Similar enhancements were later obtained in another work from the same group, using an optimized iTMC with the additions of $LiPF_6$.[77] On the other hand, the presence of LiF as an electron injection layer in LECs presented in the aforementioned works is rather unusual and may give place to misleading comparisons of these results with others given in the literature. Also, the effect of different lithium counterions on the device performances have not been studied.

For the above reasons, we prepared LECs based on the well-characterized $[Ir(ppy)_2(dtb\text{-}bpy)]^+(PF_6)^-$ iTMC (where ppy is 2-phenylpyridinato and dtb-bpy is 4,4'-di(tert-butyl)-2,2'-bipyridine)[56] in presence of four different lithium salts, namely lithium perchlorate ($LiClO_4$), lithium hexafluorophosphate ($LiPF_6$), lithium tetrafluoroborate ($LiBF_4$) and lithium bis(trifluoromethane) sulfonamide (LiTFSI) (Figure 3.5a and 3.5b). With respect to an additive-free device, we observed a general improvement of both the turn-on time and the lifetime of the LECs.

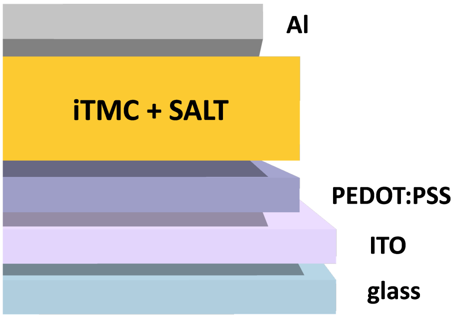

Figure 3.6.: Structure of the LECs used in this work.

3.2.2. Experimental methods

Glass substrates with pre-patterned transparent ITO electrodes were ultrasonically cleaned in detergent, milliQ water and isopropanol and finally exposed to an O_2 plasma as the last cleaning step, to remove all the possible organic contaminants.

In order to smooth the ITO surface and to enhance charge injection into the organic active layers, a thin film of the transparent conducting polymer poly(3,4-ethylenedioxythiophene) doped with polystyrene sulfonate (PEDOT:PSS, Clevios P VP AI 4083) was deposited on the substrate by spin coating and subsequently annealed at 150 °C. The final thickness of the PEDOT:PSS layer, measured by an AMBIOS XP-1 profilometer, was 80 nm. Stock solutions of the lithium salts in acetonitrile were prepared, $10\,\mathrm{mg\,mL^{-1}}$ for $LiBPF_6$, $LiBF_4$ and $13\,\mathrm{mg\,mL^{-1}}$ for $LiClO_4$, LiTFSI. The iTMC complex $[Ir(ppy)_2(dtb\text{-}bpy)]^+(PF_6)^-$ was dissolved in acetonitrile and lithium salts from the stock solutions were added up to a 9:1 molar ratio (complex:salt). The final iTMC concentration was adjusted to $20\,\mathrm{mg\,mL^{-1}}$. The solutions were filtered through a 0.22 µm filter and deposited by spin coating onto the PEDOT:PSS. The final thickness of the iTMC films was 80–90 nm. Finally, the substrates were transferred into a vacuum chamber integrated in an N_2-filled glovebox and the devices were finished by depositing a 100 nm thick aluminum cathode. The devices had four pixels, with an area of $6.535 \times 10^{-2}\,\mathrm{cm}^2$ each. Reference devices without the addition of salt were fabricated from a $20\,\mathrm{mg\,mL}^{-1}$ solution of the iTMC in acetonitrile, following the same protocol. The final structure of the LECs is shown in Figure 3.6.

The device testing took place in a glovebox using a BoTest OLT OLED Lifetime Test System. The LECs were driven in a pulsed current regime with an average current density of $100\,\mathrm{A\,m}^{-2}$ and a 50 % duty cycle (1 kHz, $200\,\mathrm{A\,m}^{-2}$ peak current density).

3.2.3. Results and discussion

The addition of the lithium salts to the iTMC has a beneficial effect on the turn-on time of LECs (t_{100}) as, with the exception of $LiBF_4$, t_{100} is greatly diminished by the addition of lithium salts, going from 76 s for the pristine device to only 8 s in the case of $LiPF_6$ additive (Figure 3.7a and Table 3.1[b]). The improvement in the turn-on time follows the same trend of the ionic conductivity of the additives, shown in Figure 3.7b and obtained for the salts in a 1 M solution in ethylene carbonate:dimethyl carbonate.[78] $LiBF_4$, besides being the salt with the lightest anion among those tested, has the lowest ionic conductivity and its effect on t_{100} is negligible, meaning that $LiBF_4$ doesn't play a relevant role in the first phases of the device operation. This is confirmed by the slow transient of the luminance visible in Figure 3.7a and it is likely due to the slow dissociation of the $LiBF_4$ salt, which has also the lowest dissociation constant among the tested additives.[79]

An indirect confirmation of this hypothesis comes from the analysis of the luminance characteristic up to 500 s. When plotted in a logarithmic time scale, all

Additive	L_{max} [a]	t_{100} [b]	$t_{1/2}$ [c]	Efficacy [d]	PCE [e]	Slope [f]
	cd m^{-2}	s	h	cd A^{-1}	lm W^{-1}	cd m^{-2} dec^{-1}
None	735	76	48	7.3	4.4	624.00
$LiClO_4$	937	14	18	9.4	4.9	639.85
$LiPF_6$	953	8	1263	9.5	5.4	908.86
$LiBF_4$	970	92	1973 [g]	9.7	6.0	1080.31
LiTFSI	1019	20	356	10.2	5.6	844.89

Table 3.1.: Parameters for the LECs under examination. [a] Maximum luminance; [b] time to reach 100 cd m^{-2} (turn-on time); [c] time to reach half of the maximum luminance (lifetime); [d] current efficiency; [e] power conversion efficiency; [f] slope of the linear increase of the luminance in the range 1–500 s; [g] extrapolated by a single exponential decay fitting.

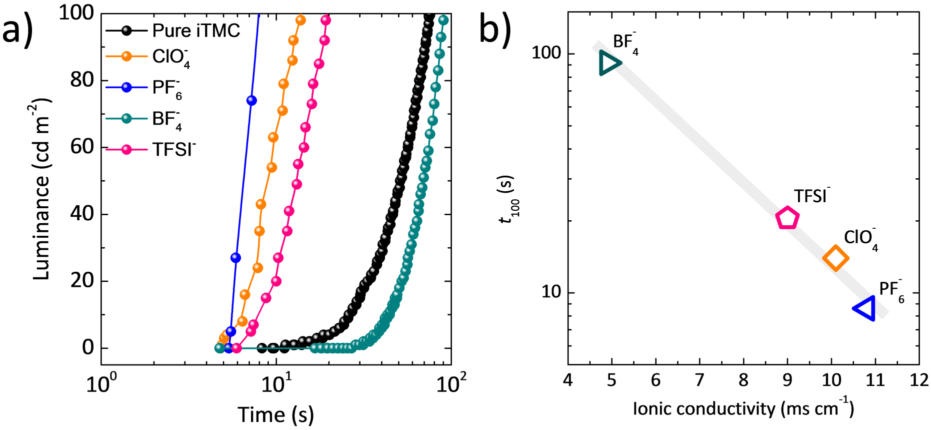

Figure 3.7.: a) Turn-on time phase for the series of LECs with and without lithium additives. b) Ionic conductivity of the lithium salts, in solution (1 M in ethylene carbonate:dimethyl carbonate).[78]

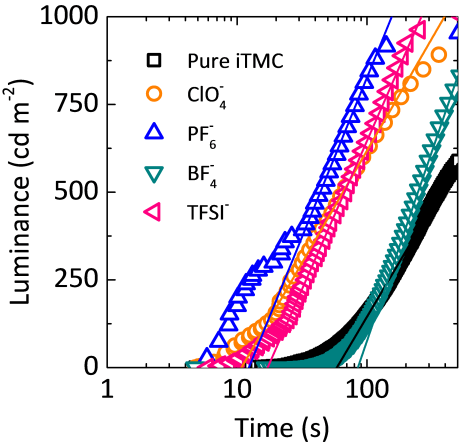

Figure 3.8.: Increase of the luminance in the time range 1–500 s.

of the devices present a linear increase of the luminance in a given timeframe. The slope relative to the LEC with $LiBF_4$ is the highest among the tested device (Figure 3.8 and Table3.1[f]). Most likely, $LiBF_4$ is not completely dissociated at the beginning of the device operation but the dissociation is slowly allowed by the electric field across the active layer. Once dissociated, the superior mobilities of Li^+ and BF_4^- allow for a faster ion redistribution and charge injection. Another confirmation of this hypothesis can be found in the work of Rudmann *et al.*, on pure iTMC LECs based on the tris(4,4'-di-tert-butyl-2,2'-bipyridyl) ruthenium(II) complex coupled with various anions. The authors report an "instantaneous" turn-on when the BF_4^- anion is used, due to its high mobility. Moreover, the ionic conductance measured in the film in the case of the BF_4^- ions is up to two orders of magnitude higher than that reported for ClO_4^- or PF_6^-.[73] As the separation of such anions from the bulky iTMC cation is expected to be relatively easy, the limiting factor in the case of our LECs is likely the dissociation of the strongly bound $LiBF_4$ salt.

The maximum luminance L_{max} is also profoundly influenced by the addition of lithium salts. In particular, the use of lithium additives results in an increase of about 20–30 % in L_{max} with respect to the pristine device (Table 3.1[a]). L_{max} in a LEC depends on the emitting species as well as on the current density and the symmetry of the *p*- and the *n*-doped zones. In fact, an unbalanced injection of electron or holes could displace the intrinsic zone (where radiative recombination occurs) towards one of the electrodes, where non-radiative recombination would limit the electroluminescence. In our case, the average current density and the electroluminescent complex are the same for all devices. For the pristine device the only available cations are not mobile and the accumulation of positive charges near the cathode is mainly due to the depletion of hexafluorophosphate ions, which migrate towards the anode. Hence, due to the steric hindrance of the iTMC cations, the ionic charge density near the cathode is much lower than that at the PEDOT:PSS/iTMC interface (Figure 3.4), leading to an asymmetrical growth of the doped zones and to a lower luminance. This issue is mitigated by the addition of the lithium salts. The presence of the small Li^+ cation allows for the formation of a compact EDL at the cathode to assist the electron injection/transport. In this way, the recombination zone is shifted towards the center of the electroluminescent layer, where non-radiative recombinations are less probable. The almost identical values of L_{max} among the LECs' series with lithium additives is mainly due to the improved electron injection, resulting from the presence of highly mobile Li^+ ions.

The addition of lithium salts is generally beneficial for the lifetime of the LECs, here defined as $t_{1/2}$, the time to reach $^1/_2 L_{\mathrm{max}}$ (Table3.1[c]). While the pristine device shows a lifetime of about 48 h, the devices with LiTFSI improves it 7-fold; $LIPF_6$ increases the stability up to almost 1300 h and an extrapolated lifetime of

Anion	**M.W.**	$t_{1/2}$
	$\mathrm{g\,mol^{-1}}$	h
$\mathbf{ClO_4^-}$	99.45	18
$\mathbf{PF_6^-}$	144.96	1263
$\mathbf{BF_4^-}$	86.80	1973
$\mathbf{TFSI^-}$	280.15	356

Table 3.2.: Comparison of the molecular weight of the lithium counterion and the lifetime of the corresponding LEC.

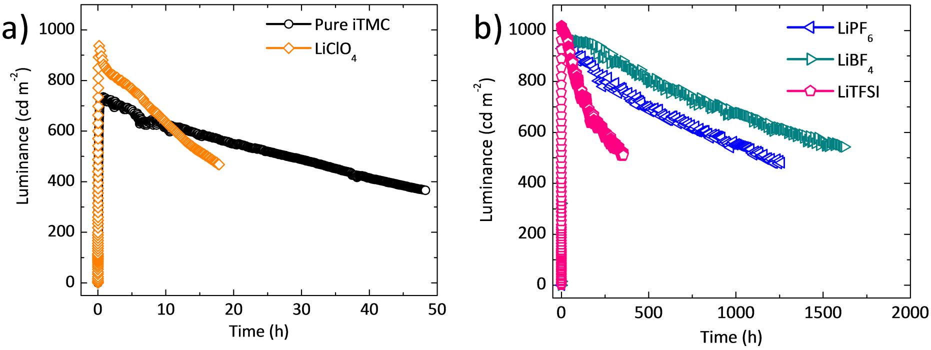

Figure 3.9.: Lifetime of the LEC series with luminance monitored over time until approximately $t_{1/2}$, for a) short-lived devices (pristine device and LEC with $LiClO_4$) and b) long-lived devices (employing $LiPF_6$, $LiBF_4$ and LiTFSI).

about 2000 h is achieved when using $LiBF_4$ (Figure 3.9). In analogy to what described for L_{max}, this improvement is attributed to a more symmetrical build-up of the ELDs at the PEDOT:PSS/iTMC and iTMC/Al interfaces. In this situation, the symmetry delays the degradation due to the overgrowth of the doped zones, which cause non-radiative recombination. In this respect, it is interesting to note that there is a correlation between the size of the anion and the corresponding device, i.e. the lighter the anion, the larger the improvement of $t_{1/2}$ (Table 3.2). The exception is represented by the $LiClO_4$ salt that, while substan-

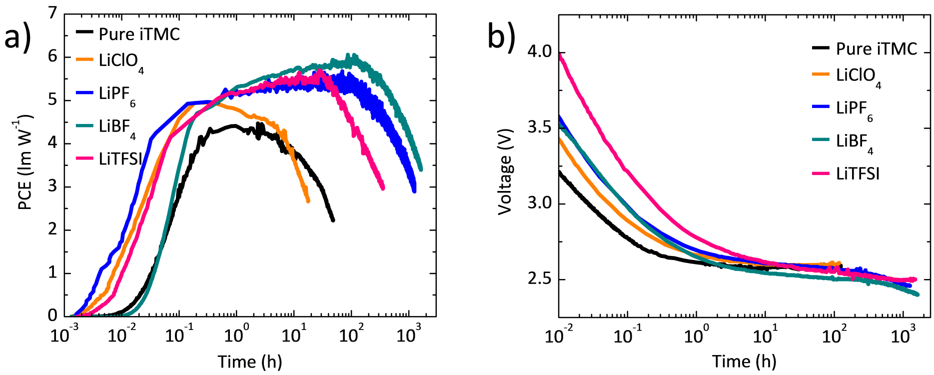

Figure 3.10.: a) Power conversion efficiency and b) voltage bias for the LECs under examination.

tially improving t_{100}, also drastically reduces the lifetime of the corresponding LEC with respect to the pristine device (from 48 h to 18 h). This behavior cannot be explained solely considering the dissociation constant of the salt or the mobility of the ions. Most likely, being ClO_4^- a strong oxidant, under high current conditions it can induce degradation of the iTMC, leading to the reduced lifetime.[80]

The efficacy of the LECs follows the same trend as the maximum luminance (Table 3.1[d]), since the devices are driven with the same average current density. On the other hand, PCE (Table 3.1[e]) is a more meaningful parameter, as it also depends on the voltage needed to sustain the current density. Both external voltage and PCE are reported as a function of time in Figure 3.10. The device with the lowest PCE, 4.4 lm W^{-1}, is that with the pure iTMC layer, because of the low maximum luminance. The PCE increases with the addition of the lithium salts, reaching a maximum of 6.0 lm W^{-1} for the LEC using $LiBF_4$ additive (Figure 3.10a). The voltage profile is similar for all of the devices, with a high initial external voltage (> 3.0 V) that slowly converges to 2.5 V, in agreement with the band gap of the electroluminescent complex, $E_g = 2.7\,\mathrm{eV}$. This suggests that at steady state the charge injection for all LECs is nearly ohmic (Figure 3.10b).

3.2.4. Conclusions

We have investigated the effect of the addition of various lithium salt to the active layer of iTMC-LECs and showed that the presence of the Li^+ cation improves the luminance by enhancing the electron injection from the cathode, allowing the formation of an intrinsic recombination zone situated near to the center of the active layer. This same argument explains also the extended lifetime of the LECs with added salts. The high mobility of the lithium cation is also responsible for a reduced turn-on time.

Two extreme cases are represented by $LiClO_4$ and $LiBF_4$. In particular, $LiClO_4$ has a beneficial effect on the turn-on phase but causes premature degradation of the organic emitter, most likely due to its strong oxidant character. $LiBF_4$, on the other hand, has negligible effect on the turn-on time of the LECs, because of its low dissociation constant, but enhances the device lifetime up to about 2000 h, a 40-fold improvement over the pure iTMC device.

3.3. Contribution of the author

E. Bandiello, M. Sessolo, H. J. Bolink, "*Lithium salt additives and the influence of their counterion on the performances of light-emitting electrochemical cells*". Journal of Materials Chemistry C, 2016, **4**, 10781-10785. DOI:10.1039/C6TC03597C

Reproduced by permission of The Royal Society of Chemistry

Journal of
Materials Chemistry C

COMMUNICATION

View Article Online
View Journal | View Issue

Cite this: *J. Mater. Chem. C*, 2016, **4**, 10781

Received 20th August 2016, Accepted 29th October 2016

DOI: 10.1039/c6tc03597c

www.rsc.org/MaterialsC

Lithium salt additives and the influence of their counterion on the performances of light-emitting electrochemical cells†

E. Bandiello, M. Sessolo* and H. J. Bolink

In this work we study the effect of the addition of lithium salts to light-emitting electrochemical cells (LECs), and in particular the effect of the lithium counterion. We found that the chosen lithium salts can substantially improve the device turn-on time as well as the overall lifetime, with respect to reference LECs using the pure emitter. A correlation between the lithium counterion and the corresponding device performance is established, and efficient LECs with lifetimes approaching 2000 hours are presented.

Since their introduction by Pei *et al.*,[1] light-emitting electrochemical cells (LECs) have been regarded as a potential alternative to the more developed organic light-emitting diodes (OLEDs). While very suited for high-end products such as displays, OLEDs production costs are still not competitive for lighting applications. OLEDs are multi-layer devices prepared by sequential vacuum deposition, and they need to be rigorously encapsulated to avoid exposure of the materials to oxygen or moisture. In contrast, LECs consist of an ionic light-emitting layer sandwiched in between two electrodes, and can be prepared using simple and potentially inexpensive solution processing methods.[2,3] Furthermore, because of the ionic-assisted charge injection mechanism,[4] their performances depend only weakly on the work function of the electrodes and stable metal cathodes can be used, requiring less stringent encapsulation as compared to OLEDs. In LECs, following the application of an external bias, ions accumulate at the active layer/electrode interface promoting charge injection. The injected charges lead to the oxidization and reduction of the semiconducting material, which is stabilized by the uncompensated ions of opposite sign present at the electrode interfaces, in analogy to what is obtained by chemical oxidation and reduction in doped organic devices.[5] Such doped zones are highly conductive regions that slowly grow toward each other, separated by an intrinsic region where electroluminescence takes place. The progressive growth of the doped zones eventually reduces the thickness of the intrinsic region, and leads to a reduction of the electroluminescence of the device.[4] The main disadvantages of LECs are their slow turn-on time, due to their reliance on ionic processes, and the relatively short lifetime which is limited by the only partially reversible electrochemical reactions following doping of the active material.[1,4,6] Interestingly, the lifetime and the turn-on time in LECs are often inversely proportional, *i.e.* slower LECs are more stable as compared to fast devices, which in turn have usually shorter lifetimes. This limitation is often observed when driving LECs at a fixed voltage (DC), and it can be partially overcome by the optimization of the emitting molecules,[7,8] by using a different driving mode such as constant or pulsed current,[9–12] or with the addition of salts or polymeric electrolytes to the active layer.[13–16] The latter approach has been widely adopted by using ionic liquids, which increase the ionic conductivity of the active layer. In most common iTMC-based LECs the electroluminescent complex has a rather bulky cation and a relatively small and light anion. As a consequence, the ion redistribution under bias is asymmetric since, while conserving the global net charge, the density of positive ions near the cathode is much lower than that of anions near the anode. This can lead to unbalanced charge injection, displacing the intrinsic zone from the center of the active layer and causing quenching of the electroluminescence, limiting the device lifetime.[17] These phenomena can take place even in the presence of common ionic liquids, whose cations are usually much bigger than the anions. Recently, Shen and coworkers made use of lithium hexafluorophosphate ($LiPF_6$), with a more balanced anion and cation size/mobility ratio, and demonstrated high performance devices, in terms of lifetime and brightness.[18] However, the screening of different counterions for lithium and their effect on the device performance have not yet been reported. In this work we study LECs based on the $[Ir(ppy)_2(dtb\text{-}bpy)](PF_6)$ (where ppy is 2-phenylpyridinato and dtb-bpy is 4,4′-di(*tert*-butyl)-2,2′-bipyridine),[19] and compare the behavior of a reference device with the pure iTMC active layer to that of devices containing lithium salts, in particular $LiPF_6$, $LiClO_4$, $LIBF_4$ and LiTFSI, where TFSI is bis(trifluoromethane)sulfonimidate.

Instituto de Ciencia Molecular, Universidad de Valencia, Catedrático José Beltrán Martínez 2, Paterna, 46980, Valencia, Spain. E-mail: michele.sessolo@uv.es

† Electronic supplementary information (ESI) available. See DOI: 10.1039/c6tc03597c

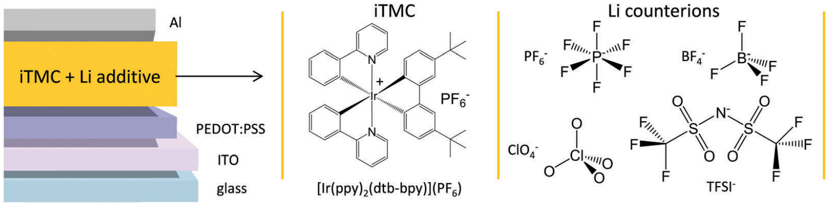

Fig. 1 Structure of the LECs and of the materials used in the active layer.

We found that the counterion of Li^+ has a dramatic effect on the performance and lifetime of the LECs. In particular, the ionic conductivity and the dissociation constant have a strong impact on the turn-on time and overall lifetime of the LECs using iTMC as the active material.

The structures of the device and materials used are depicted in Fig. 1. Glass substrates with pre-patterned indium tin oxide (ITO) electrodes, were cleaned using chemical and plasma methods. A thin layer of poly(3,4-ethylenedioxythiophene) doped with polystyrene sulfonate (PEDOT:PSS) was coated on top of the ITO electrode in order to smooth the surface and improve the iTMC film formation. Stock acetonitrile solutions of the lithium salts were prepared and added to the solution of the complex in a 1 : 9 molar ratio with respect to the iTMC. Pure acetonitrile was then added to obtain a 20 mg mL^{-1} concentration in iTMC. The solutions were filtered through a 0.20 μm filter and spin coated directly on the PEDOT:PSS to a thickness of 100 nm. A 70 nm-thick aluminum cathode was thermally deposited on top. Importantly, the aluminum cathode is in direct contact with the active layer and no electron injection layers (such as LiF) are used. As such, electron injection is assisted exclusively by ionic processes.

LECs were driven with a pulsed current at an average current density of 100 A m^{-2} (200 A m^{-2} peak current density, 1 kHz, 50% duty cycle). All characterizations were performed in a nitrogen filled glove box. As mentioned before, an important parameter which is related to the ionic conductivity of the active layer is the turn-on time, defined here as the time at which the luminance L of a device exceeds 100 cd m^{-2} (t_{100}). The definition of the turn-on time here is different from others previously used in the literature, where the turn-on time is chosen to be the time at which the luminance L reaches its maximum value, t_{max}. When comparing different devices, however, the choice of t_{100} as a figure of merit allows for a more direct comparison of the beginning of the LEC operation, when the ionic effects are predominant.

The addition of lithium salts, with the exception of $LiBF_4$, greatly diminishes the turn-on time with respect to the pure iTMC LECs (Fig. 2a). The fastest device is the one with $LiPF_6$, with a t_{100} of 8 s, while slightly higher values are found for the $LiClO_4$ and LiTFSI (see Table 1 for the values of representative

Table 1 Parameters for the LECs under examination for chosen representative devices

Additive	L_{max}[a] (cd m^{-2})	t_{100}[b] (s)	$t_{1/2}$[c] (h)	Efficacy[d] (cd A^{-1})	PCE[e] (lm W^{-1})
None	735	76	48	7.3	4.4
$LiClO_4$	937	14	18	9.4	4.9
$LiPF_6$	953	8	1263	9.5	5.4
$LiBF_4$	970	92	1973[f]	9.7	6.0
LiTFSI	1019	20	356	10.2	5.6

[a] Maximum luminance. [b] Time to reach 100 cd m^{-2} (turn-on time). [c] Time to reach half of the maximum luminance (lifetime). [d] Current efficiency. [e] Power conversion efficiency. [f] Extrapolated from the luminance data by a single exponential decay fitting.

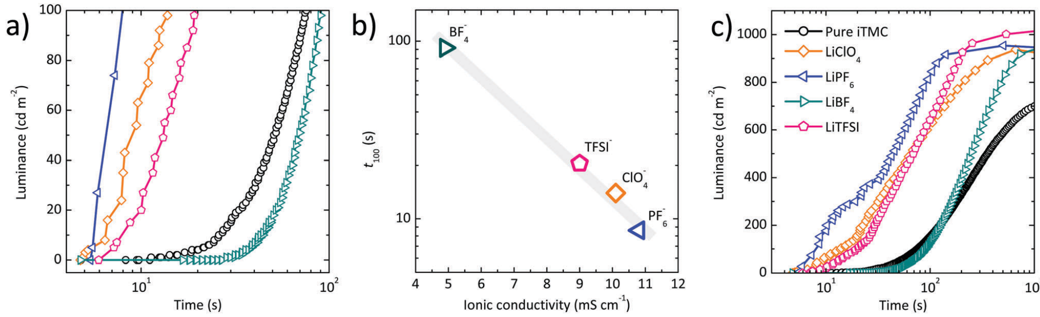

Fig. 2 (a) Turn-on time phase for the series of LECs with and without lithium additives. (b) Turn-on time t_{100} *versus* ionic conductivity for the series of lithium additives used. The conductivity values for different salts were obtained on 1 M solutions in a 1 : 1 mixture of ethylene carbonate : carbonate. Values taken from ref. 20. (c) Device operation in the range 0–1000 s. The slope of the $LiBF_4$ luminance in the range from 100 s to 500 s is the highest among the studied LECs.

devices; average values are reported in Table S2, ESI†). The curves for the LECs incorporating these three salts show a steep slope since the beginning, whereas in the case of the devices employing the pure iTMC and that with $LiBF_4$, a slow transient is visible. This is most likely due to the slow dissociation of $LiBF_4$ as it has the lowest dissociation constant among the tested salts.[21] Thus, despite $LiBF_4$ being the lithium salt with the lightest anion, its effect on the turn-on of the LEC is negligible. Interestingly, we found a clear correlation between t_{100} and the ionic conductivity of the lithium salts measured in solution (Fig. 2b), in agreement with previous reports on 1-butyl-3-methylimidazolium ionic liquids.[22] The difference between the t_{100} for the pure iTMC LEC and the one with $LiBF_4$ (76 s *vs.* 91 s) is hardly significant, meaning that $LiBF_4$ does not play a relevant role during the turn-on process of the device. On the other hand, analyzing the luminance characteristics in the timescale from 100 s to 1000 s, the slope of the luminance for the device containing $LiBF_4$ increases fast and surpasses that of any of the other LECs (Fig. 2c and Fig. S1, Table S1 in the ESI†).

This is an indirect confirmation that the $LiBF_4$ salt is not completely dissociated at the beginning of the device operation, while after dissociation the lithium ion can drift and charge injection takes place. Interestingly, in this second regime the LECs with $LiBF_4$ show a very high luminance growing rate, due to the high mobility of the BF_4^- anion. This behavior is reminiscent of what is observed when BF_4^- or ClO_4^- are used as the counterions of the tris(4,4′-di-*tert*-butyl-2,2′-bipyridyl)ruthenium(II) complex. In those works, instantaneous turn-on was observed due to the high mobility of the anions after dissociation.[13,23] Another figure of merit for LECs is the maximum achievable luminance L_{max}. In the device series studied here, the addition of lithium additives into the active layer increases L_{max} a 20–30% with respect to the device employing the pure iTMC (Table 1). The absolute L_{max} value does not change significantly between the LECs with different lithium additives, and a very high brightness is observed for all the Li-containing devices with maximum exceeding 1000 cd m^{-2} for those employing LiTFSI. For a fixed emitting species in an LEC, L_{max} depends both on the current flowing through the device and on the degree of symmetry associated with the build-up of the p and n doped zones. In fact, an unbalanced charge injection would cause the intrinsic zone to be displaced towards one of the electrodes, where the probability of non-radiative recombination increases. In our case the average current density as well as the hole injection interface are the same for all devices, hence it is the electron injection that determines the electroluminescence rate. In the device employing the pure iTMC, the only available cations are not mobile and their density near the cathode is limited by the iTMC steric hindrance. This translates into a low charge density at the cathode, which is mainly a consequence of the displaced anions, and hence in an inefficient electron injection. Therefore, for the pure iTMC LECs the carrier injection is likely to be asymmetric, with the intrinsic zone shifted towards the cathode, with augmented non-radiative recombination. In the presence of the very mobile Li^+ cation, the charge density near to the cathode (and thus the electric field) is larger, which improves the electron injection enhancing the device brightness. Direct evidence of this effect in iTMC LECs employing lithium salts has been reported recently.[17,24]

A direct effect of the symmetry, distribution and width of the intrinsic zone is on the device lifetime $t_{1/2}$, defined here as the time at which the luminance decays to $\frac{1}{2}L_{max}$. In general, we found the addition of lithium salts to be beneficial for the LEC lifetime. In the extreme cases, the pure iTMC device has $t_{1/2}$ of 48 hours (Fig. 3a) while the device employing $LiBF_4$ shows an extrapolated lifetime of approximately 2000 hours (Fig. 3b), a 40-fold increase with an almost identical turn-on time. The longer lifetime can be explained on the basis of a rather symmetrical build-up of the doped zones within the active layer, consequence of the more balanced mobility between the cation and the anion. In the case of TFSI, due to its relatively large size, the ionic distribution among the anode and cathode interface might be less symmetrical, leading to the observed reduced lifetimes. On the other hand, the device with $LiClO_4$ degrades rapidly ($t_{1/2}$ = 18 hours), a behavior which cannot be rationalized with simple considerations on the ionic dissociation constant or conductivity. Most likely, the strong oxidant character of the perchlorate ion can lead to side reactions with the iTMC under high-current conditions, thus strongly limiting the LEC lifetime.[25]

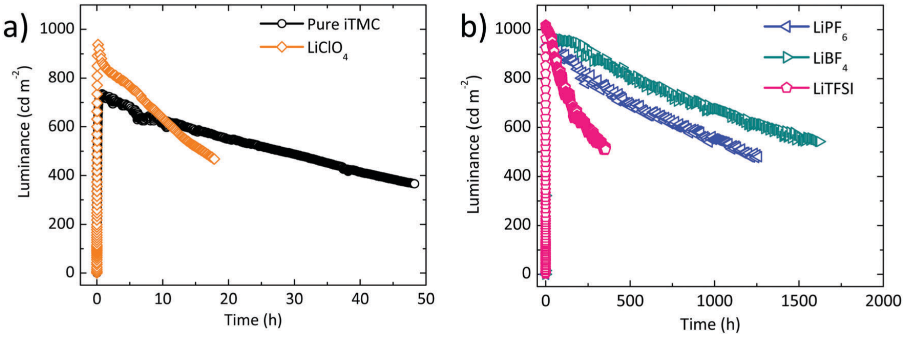

Fig. 3 Lifetime evaluation of the LEC series with luminance monitored over time until approximately $t_{1/2}$, for (a) short-lived devices (pure iTMC and those with $LiClO_4$) and (b) long-lived devices (employing $LiPF_6$, $LiBF_4$ and LiTFSI).

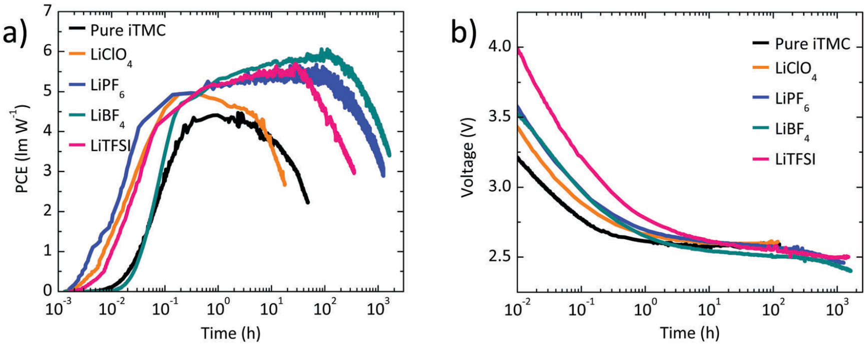

Fig. 4 (a) Power conversion efficiency and (b) external bias measured for the LEC series.

Finally, we calculated the current efficiency (efficacy, in cd A^{-1}) of the devices, whose trend essentially follows the luminance characteristics, being the LECs driven with the same pulsed current density. It is more interesting to look at the power conversion efficiency (PCE, Fig. 4a), which takes into account the voltage needed to sustain the current density flowing through the device (Fig. 4b). Plots are now reported on a log scale in order to highlight the otherwise sudden drop of the potential at the beginning of the device operation.

As expected, the PCE is lower for the device using the pure iTMC and for the one employing $LiClO_4$ (4.4 and 4.9 lm W^{-1}, respectively). On the other hand, LECs where $LiPF_6$, $LiBF_4$ or LiTFSI are added into the active layer show higher PCEs, with a maximum of 6.0 lm W^{-1} for the device using $LiBF_4$ as the additive. Besides leading to the highest absolute luminance, the device with LiTFSI shows a higher voltage profile compared to the other LECs, which in turns limits the overall PCEs. All applied voltage decrease rapidly converging to a value of approximately 2.5 V, in agreement with the iTMC bandgap energy of approximately 2.7 eV and suggesting a nearly ohmic charge injection form the external electrodes for all devices.

Conclusions

In summary, we studied the effect of the incorporation of lithium salts into the active layer of light-emitting electrochemical cells employing ionic transition metal complexes. We determine the devices with pure iTMC active films to be electron-injection limited, at least in the first tens of seconds after biasing, a limitation that can be overcome with the addition of the highly mobile lithium cation in the active layer. Furthermore, we identified the ionic conductivity and dissociation constant of the lithium salts as the main parameters determining the device turn-on time. A higher tendency to dissociate into free ions is in fact responsible for an earlier ionic accumulation at the electrode interfaces and hence of a faster charge injection. Faster turn-on times were in fact observed for devices containing $LiClO_4$, $LiPF_6$ and LiTFSI, while $LiBF_4$, due to its low dissociation constant, has a negligible effect on the turn-on. Besides this effect, $LiBF_4$ is found to be the most suitable additive if high efficiency and stable devices are desired. Maximum luminance values of about 1000 cd m^{-2}, with power conversion efficiency reaching 6 lm W^{-1}, and lifetime of 2000 hours have been obtained, making lithium salts the most promising additives for applications in light-emitting electrochemical cells.

Acknowledgements

We acknowledge financial support from the European Union H2020 project INFORM (grant 675867), the Spanish Ministry of Economy and Competitiveness (MINECO) *via* the Unidad de Excelencia María de Maeztu MDM-2015-0538, MAT2014-55200 and PCIN-2015-255 and the Generalitat Valenciana (Prometeo/2012/053). M. S. and E. B. thank the MINECO for their post-doctoral (JdC) and pre-doctoral grants, respectively.

Notes and references

1 Q. Pei, G. Yu, C. Zhang, Y. Yang and A. J. Heeger, *Science*, 1995, **269**, 1086–1088.
2 R. D. Costa, E. Orti, H. J. Bolink, F. Monti, G. Accorsi and N. Armaroli, *Angew. Chem.*, 2012, **51**, 8178–8211.
3 A. Sandström and L. Edman, *Energy Technol.*, 2015, **3**, 329–339.
4 S. van Reenen, P. Matyba, A. Dzwilewski, R. A. Janssen, L. Edman and M. Kemerink, *J. Am. Chem. Soc.*, 2010, **132**, 13776–13781.
5 K. Walzer, B. Maennig, M. Pfeiffer and K. Leo, *Chem. Rev.*, 2007, **107**, 1233–1271.
6 M. Lenes, G. Garcia-Belmonte, D. Tordera, A. Pertegás, J. Bisquert and H. J. Bolink, *Adv. Funct. Mater.*, 2011, **21**, 1581–1586.
7 E. Zysman-Colman, J. D. Slinker, J. B. Parker, G. G. Malliaras and S. Bernhard, *Chem. Mater.*, 2008, **20**, 388–396.
8 A. M. Bunzli, E. C. Constable, C. E. Housecroft, A. Prescimone, J. A. Zampese, G. Longo, L. Gil-Escrig, A. Pertegas, E. Orti and H. J. Bolink, *Chem. Sci.*, 2015, **6**, 2843–2852.

9 S. B. Meier, W. Sarfert, J. M. Junquera-Hernández, M. Delgado, D. Tordera, E. Ortí, H. J. Bolink, F. Kessler, R. Scopelliti, M. Grätzel, M. K. Nazeeruddin and E. Baranoff, *J. Mater. Chem. C*, 2013, **1**, 58–68.

10 D. Tordera, J. Frey, D. Vonlanthen, E. Constable, A. Pertegás, E. Ortí, H. J. Bolink, E. Baranoff and M. K. Nazeeruddin, *Adv. Energy Mater.*, 2013, **3**, 1338–1343.

11 D. Tordera, M. Lenes and H. J. Bolink, *J. Nanosci. Nanotechnol.*, 2013, **13**, 5170–5174.

12 N. M. Shavaleev, R. Scopelliti, M. Grätzel, M. K. Nazeeruddin, A. Pertegás, C. Roldán-Carmona, D. Tordera and H. J. Bolink, *J. Mater. Chem. C*, 2013, **1**, 2241.

13 H. Rudmann, S. Shimada and M. F. Rubner, *J. Am. Chem. Soc.*, 2002, **124**, 4918–4921.

14 S. T. Parker, J. D. Slinker, M. S. Lowry, M. P. Cox, S. Bernhard and G. G. Malliaras, *Chem. Mater.*, 2005, **17**, 3187–3190.

15 J. D. Slinker, C. Y. Koh, G. G. Malliaras, M. S. Lowry and S. Bernhard, *Appl. Phys. Lett.*, 2005, **86**, 173506.

16 J. Mindemark, S. Tang, J. Wang, N. Kaihovirta, D. Brandell and L. Edman, *Chem. Mater.*, 2016, **28**, 2618–2623.

17 K.-Y. Lin, L. D. Bastatas, K. J. Suhr, M. D. Moore, B. J. Holliday, M. Minary-Jolandan and J. D. Slinker, *ACS Appl. Mater. Interfaces*, 2016, **8**, 16776–16782.

18 Y. Shen, D. D. Kuddes, C. A. Naquin, T. W. Hesterberg, C. Kusmierz, B. J. Holliday and J. D. Slinker, *Appl. Phys. Lett.*, 2013, **102**, 203305.

19 J. D. Slinker, A. A. Gorodetsky, M. S. Lowry, J. Wang, S. Parker, R. Rohl, S. Bernhard and G. G. Malliaras, *J. Am. Chem. Soc.*, 2004, **126**, 2763–2767.

20 R. Younesi, G. M. Veith, P. Johansson, K. Edström and T. Vegge, *Energy Environ. Sci.*, 2015, **8**, 1905–1922.

21 V. Aravindan, J. Gnanaraj, S. Madhavi and H. K. Liu, *Chem. – Eur. J.*, 2011, **17**, 14326–14346.

22 R. D. Costa, A. Pertegás, E. Ortí and H. J. Bolink, *Chem. Mater.*, 2010, **22**, 1288–1290.

23 F. G. Gao and A. J. Bard, *J. Am. Chem. Soc.*, 2000, **122**, 7426–7427.

24 L. D. Bastatas, K. Y. Lin, M. D. Moore, K. J. Suhr, M. H. Bowler, Y. Shen, B. J. Holliday and J. D. Slinker, *Langmuir*, 2016, **32**, 9468–9474.

25 K. Xu, *Chem. Rev.*, 2004, **104**, 4303–4418.

4. Ionic-Electronic Conductivity in Hybrid Perovskites

4.1. Hybrid perovskites for photovoltaics

In the following sections hybrid perovskite materials will be introduced, explaining the reasons behind their popularity in photovoltaics applications and the main issues affecting their optoelectronic behavior. In particular, the effects related to the presence of mobile ions in the perovskite will be investigated by means of current–voltage measurement.

4.1.1. Introduction

Perovskite solar cells (PSCs, in the following) are photovoltaic devices based on hybrid crystalline perovskite materials constituted by an organic cation intercalated in an inorganic framework. The name *perovskite* refers to a well-defined crystal structure and not to a particular material. The most studied compound among hybrid perovskites is the methylammonium lead iodide, $CH_3NH_3PbI_3$ or $MAPbI_3$, which at room temperature adopts the tetragonal structure shown in Figure 4.1. The Pb ion occupies the center of an octahedron formed by the six nearest iodine atoms while the methylammonium ion resides in the free space

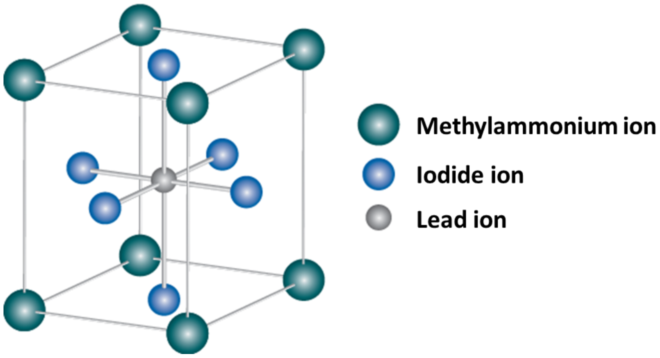

Figure 4.1.: Tetragonal crystal structure at RT of the methylammonium lead iodide perovskite $CH_3NH_3PbI_3$.

between the octahedra. In only seven years since their introduction in 2009, PSCs have increased their efficiency from 3.81 % up to today's certified efficiencies exceeding 20 %.[18,81,82] What makes $MAPbI_3$ such an attractive material for photovoltaics is the unique combination of favorable characteristics such as:

- ▷ The high optical absorption, which allows the harvesting of a large amount of photons with relatively thin films.[83]
- ▷ The narrow band gap ($Eg = 1.55\,\mathrm{eV}$), which makes $MAPbI_3$ capable of absorbing light through the whole visible spectrum.[84] The band gap can be further decreased by the partial substitution of methylammonium cation with the formamidinium cation.[85] This allows the harvesting of additional photons in the near-infrared spectral region. It is interesting to note that hybrid perovskites with wider bang gap, based on other halides such as bromide ($MAPbBr_3$), are being studied to be employed as the main component in efficient light-emitting devices.[86–89]
- ▷ The low exciton binding energy (around 10–16 meV).[90,91] $MAPbI_3$ is a non-excitonic material, meaning that photogenerated electrons and holes

are present mostly as free charges even at RT.

- ▷ The long-range carrier diffusion length, in excess of 1 µm.[92] This implies an efficient carrier extraction in a solar cells even from relatively thick perovskite layers.[93]
- ▷ The defects due to grain boundaries do not generate trap states in the band gap that might limit the charge diffusion.[83]
- ▷ The high carrier mobility, in the range between 60 to 500 $\mathrm{cm^2\,V^{-1}\,s^{-1}}$.[94,95]
- ▷ The precursor materials for $MAPbI_3$ or analogue perovskites are inexpensive and perovskite thin films can be processed by simple solution or vacuum deposition methods.

Typically, PCSs are fabricated by depositing a perovskite film with a thickness of about 500 nm between an electron transport layer (ETL) and a hole transport layer (HTL). Transport layers are chosen to block charges of opposite the sign by means of proper band alignment (i.e. ETL is a hole-blocker, HTL is an electron-blocker). ETLs can be either an organic material, or a planar or mesoporous metal oxide, in particular TiO_2 or Al_2O_3, while conventional HTLs are organic semiconductors such as Spiro-OMeTAD or arylamine derivatives.[84,93,96,97] Recently, fully evaporated PSCs employing doped and intrinsic small molecular weight organic semiconductors as the ETL and the HTL have been presented, with an efficiency approaching 20 % for the best performing devices.[98] The complete stack always includes a transparent conducting oxide (ITO, FTO) on top of a glass substrate and a metal electrode prepared by thermal vacuum deposition. Depending on the type of transport material (*p*- or *n*-type) deposited on the transparent substrate, two structures with opposite polarity, *n*-*i*-*p* or *p*-*i*-*n*, are commonly employed (Figure 4.2).

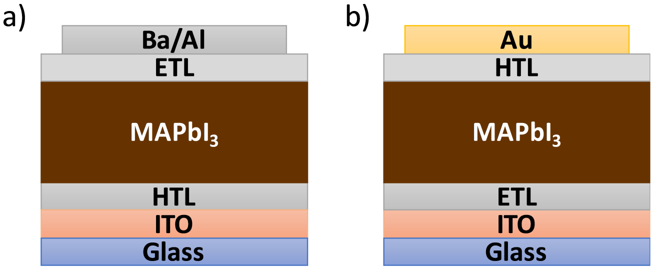

Figure 4.2.: Complete stack for a PSC in the a) *p*-*i*-*n* and b) *n*-*i*-*p* configuration. The classification depends on the order of the deposition of the HTL and ETL. A low work function metal (Ba) is used as the anode in the *p*-*i*-*n* case, while a high work function electrode (Au) acts as the cathode in the *n*-*i*-*p* configuration.

Despite perovskite's outstanding performances, some issues need to be addressed before PSCs become interesting from the point of view of commercial, real-life applications. First of all, $MAPbI_3$ is rather unstable in ambient conditions, as oxygen and moisture degrade it rapidly. Within this view, many research efforts are being devoted to understand the degradation mechanism of the material and to overcome its instability.[99–104] Another important issue is that simple J–V sweeps in $MAPbI_3$ cells may be not indicative of the real device performances, as they are often affected by a certain degree of hysteresis and dependence on the sweep direction and speed.[105] Moreover, transient phenomena regarding the photocurrent or the photovoltage on time scales on the order of tens or hundreds or seconds are visible during the measurements. Among the hypotheses explaining these phenomena, effects such as the interaction between the perovskite and the charge transport material,[106] electronic trapping at the interface of the perovskite or at the grain boundaries,[107] the light-aided polarization of the MA^+ cations under a voltage bias[20] or the presence of mobile ions in the perovskite have been investigated.[19] While probably all of the aforementioned effects contribute to the peculiar behavior of PSCs, the consensus is that mobile ions are indeed present in the bulk of perovskite. This hypothesis is interesting because it opens the door to the possibility of tuning the performances of photovoltaic devices by means of the interaction of these ions with the photogenerated carriers, as we will see in the following sections. As an extreme example, cells with symmetric electrodes showed a completely switchable photovoltaic behavior when biased for a few minutes.[108]

Despite the large number of studies devoted to the ionic character of $MAPbI_3$, it is still not completely clear which ionic species is responsible for the slow electronic processes observed during simple current–voltage sweeps. Due to a low activation energy, the most mobile ion in $MAPbI_3$ is predicted to be I^- and indirect and direct evidences of its motion have been reported.[109,110] Nonetheless, iodine vacancies and interstitial defects have been show to migrate through a 300 nm thick perovskite layer in nanosecond, hence they are unlikely to play any relevant role in the observed hysteretic behavior or transient phenomena, which develop on much longer timescales (tens of seconds). Similar considerations exclude the motion of the slow Pb_2^+ vacancies to be the cause of the observed effects, which are then attributed mainly to the motion of methylammonium vacancies.[111] Independently on the actual migrating species in $MAPbI_3$, mobile ions can be generated by the non-perfect initial stoichiometry of the perovskite film or by its degradation, which creates defects and vacancies in the layer. Also, reversible decomposition of the $MAPbI_3$ under bias at a moderate temperature of 330 K has been demonstrated, implying that similar processes can likely take place at RT, even if on a longer time scale.[112]

The following sections will mainly focus on the optoelectronic properties of the $MAPbI_3$ material and will include an evaluation of the performances of typical

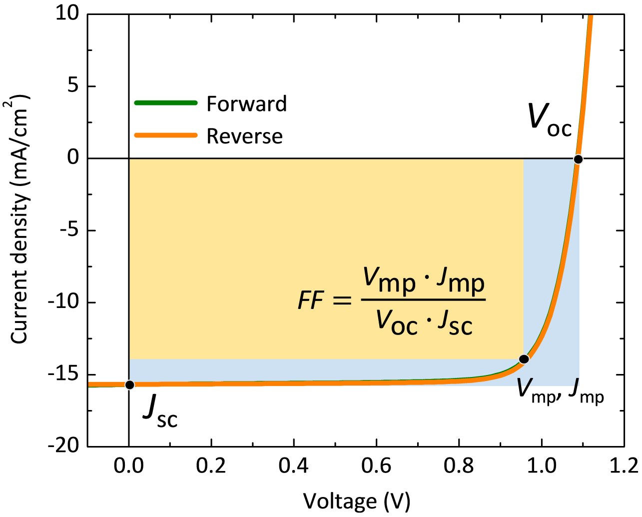

Figure 4.3.: Typical J–V curve of a p-i-n PSC with a 300 nm-thick $MAPbI_3$ layer and the structure described in Section 4.2.1. The main parameters used in the characterization of a solar cell are indicated. The product of V_{mp} and J_{mp} is the maximum power that the solar cell can deliver.

p-i-n perovskite solar cells. For this reason, the parameters used to calculate the efficiency of such a device, extracted from the J–V curves of the device measured under standard AM 1.5 G illumination,[113] are reported here as a reference (Figure 4.3):

The current density at short circuit, J_{sc}**.** Measured in $mA\,cm^{-2}$, is the current density generated by the solar cell when the external voltage V_{sweep} is 0 V. Values of J_{sc} for state-of-the-art PSCs are in excess of $20\,mA\,cm^{-2}$.

The open circuit voltage, V_{oc}**.** Measured in V or mV, this value represents the maximum voltage attainable from the photovoltaic device and is measured when the current through the cell is 0 A. The value of V_{oc} depends on the band gap of the perovskite, the energy levels of the charge transport layers, and the work function of the electrodes. Record values of V_{oc} for a PSC based on MAPbI$_3$ are in excess of 1.1 V.

The fill factor, FF. Reported as %, it essentially measures the efficiency of the charge extraction in a solar cell. It is calculated as $(V_{\mathrm{mp}} \cdot J_{\mathrm{mp}})/(V_{\mathrm{oc}} \cdot J_{\mathrm{sc}})$, where V_{mp} and J_{mp} are, respectively, the voltage and the current of the cell when it is delivering its maximum power output. In short, FF is the ratio of the actual power delivered by the solar cell to its theoretical maximum power and measures the "squareness" of the J–V curve. Graphically, it is the ratio between the areas of the yellow rectangle and the cyan rectangle in Figure 4.3. State-of-the-art PSC solar cells have $FF \geqslant 80\,\%$.

The actual efficiency η of a SC (also known as power conversion efficiency or PCE) is expressed in % and calculated using the formula:

$$\eta = \frac{FF \cdot J_{\mathrm{sc}} \cdot V_{\mathrm{oc}}}{P_{\mathrm{in}}} \times 100\,\% \tag{4.1}$$

in which P_{in} is incident light power ($100\,\mathrm{mW\,cm^{-2}}$ for standard AM 1.5 G illumination).

4.2. Effect of mobile ions on the electroluminescence of MAPbI$_3$ diodes

In this work we compare the electrical and electroluminescent behavior of an ambipolar and a single-carrier (i.e. hole only) planar diodes based on MAPbI$_3$. Using a combination of DC bias and fast J–V sweeps we show that, while the ambipolar device is dominated by the electronic processes, the current injection and the electroluminescence in the single-carrier device are strongly time- and bias-dependent. We attribute this behavior to the ionic-assisted improved injection, with a mechanism analogue to that already seen in LECs (see Section 3.1). As a further confirmation of this hypothesis, we show that the efficiency of a degraded PSC can be partially recovered when a voltage bias is applied to it, because of the improved charge extraction due to ionic effects.

4.2.1. Experimental methods

For this work, two devices were fabricated, both in the *p*-*i*-*n* configuration: a reference ambipolar PSC (device A) and a hole-only device (device B). Both were fabricated on a glass substrate with pre-patterned ITO electrodes. For device A, a thin film (50 nm) of the organic transparent conductor poly(3,4-ethylenedioxythiophene) polystyrene sulfonate (PEDOT:PSS) was deposited on top of the ITO and annealed at 150 °C for 15 min. Subsequently, a thin layer ($<$ 20 nm) of poly(N,N'-bis(4-butylphenyl)-N,N'-bis(phenyl)benzidine) hole transport layer/electron-blocker (poly-TPD), was deposited on top of the PEDOT:PSS by spin coating from a 7 mg mL^{-1} solution in chlorobenzene. The $MAPbI_3$ films were deposited by a dual source vapor deposition method described elsewhere.[97] The thickness of the $MAPbI_3$ was kept at 100 nm, to enhance the effect of the applied field at low voltages. The ETL/hole-blocker indene-C_{60}-propionic acid hexyl ester (IPH), a fullerene derivative, was deposited on top of the perovskite layer by spin-coating (40 nm) from a 20 mg mL^{-1} solution in chlorobenzene. The device was finished with a Ba/Ag electrode, deposited by thermal vacuum evaporation.

In device B the PEDOT:PSS layer was removed, because of its ionic nature which might interfere with the electrical measurements on the ionic properties of the perovskite. In order to obtain a single carrier, hole-only device, the IPH layer

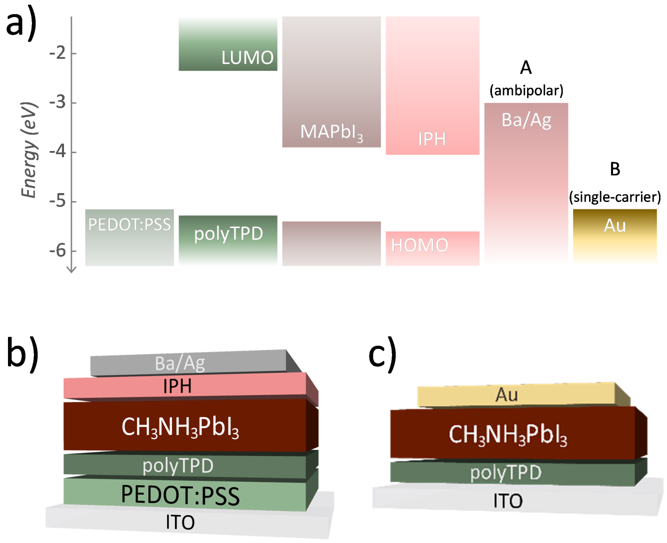

Figure 4.4.: a) Flat band energy diagram for the materials used in the ambipolar device A (Ba/Ag electrode) and the unipolar device B (Au electrode). b) Structure of the reference (ohmic) device with the PEDOT:PSS as the hole injection layer and the Ba/Ag anode. c) Structure of the single carrier device, without PEDOT:PSS and with the Au anode

was removed and the top electrode was replaced by gold. Given the large work function of Au, a high energy barrier for the electron injection is created at the Au/perovskite interface. The energy levels of the materials and the structure of the devices are reported in Figure 4.4

The measurements performed on the devices consisted in rapid J–V sweeps (V_{sweep}, $2\,\text{V}\,\text{s}^{-1}$) taken at regular intervals (30 s), while biasing them in DC over time at different voltages (V_{bias}). The slow and the fast component of the current density J where later decoupled to highlight the ionic contributions and the electronic process. The J–V scan are fast enough to avoid perturbing the ion distribution, and the minimum V_{sweep} has been kept at 1 V, in order to avoid

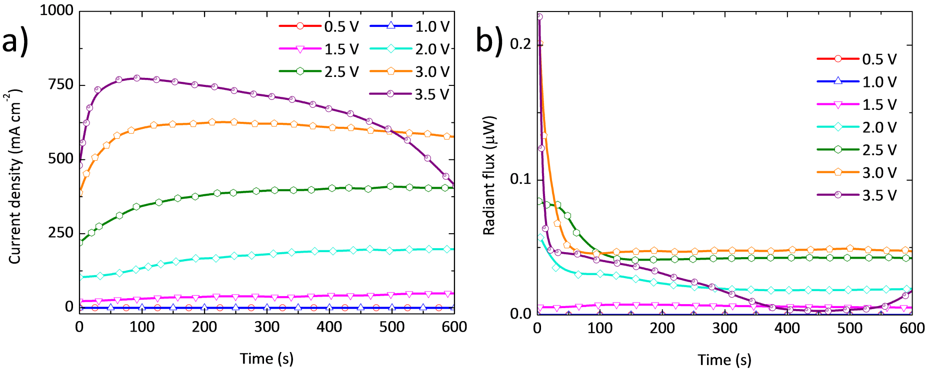

Figure 4.5.: a) current density and b) radiant flux versus time for the perovskite diode A (ambipolar) for increasing voltage (V_{bias}) (DC component).

the complete relaxation of the system.[114] The near infrared electroluminescence was monitored with a Si photodiode.

All the experiments have been performed in the dark on non-encapsulated samples in an inert N_2 atmosphere. A reference cell (device A) was then allowed to degrade in air for few days and its performances as a solar cell were measured with a solar simulator, limiting the illuminated area to 10^{-2} cm^2 with a shadow mask. The photovoltaics characterization was repeated after positively biasing the cell in the dark for 300 s at various V_{bias}.

4.2.2. Results and discussion

The DC component of the current density and the electroluminescence emission from device A at various values of V_{bias} are shown in Figure 4.5. For $V_{\text{bias}} \leqslant 1.0$ V the current density is low and no electroluminescence can be detected. When $V_{\text{bias}} > 1.0$ V the current density slowly increases over time and with increasing applied voltage. Independently on the value of V_{bias}, the current density shows a transient behavior with a slow increase, until a constant value is reached. This can

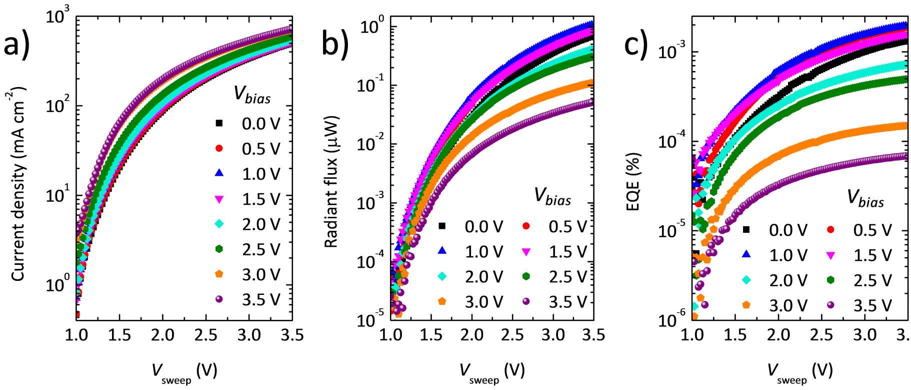

Figure 4.6.: a) Current, b) radiant flux and c) external quantum efficiency of the device A during the fast J–V_{sweep} scan after 30 s biasing at different voltages V_{bias}.

be due either due to the decrease of the injection barriers or to an enhancement of the conductivity of the perovskite layer. Given the long time scale of this transient, it can be attributed to ionic migration, with a mechanism similar to that observed in LECs.[1,6,114] When $V_{\text{bias}} \geqslant 3.0\,\text{V}$ the current reaches a maximum and then it decreases steadily. No light emission was observed for $V_{\text{bias}} < 1.5\,\text{V}$, while for higher bias values the electroluminescence decays sharply in the first 30–60 s. The reason of this decay is the formation of quenching species near the recombination zone, probably as a consequence of the decomposition of $MAPbI_3$ due to the strong electrical field[112] (which is over $9\,\text{V}\,\mu\text{m}^{-1}$ for $V_{\text{bias}} > 1.5\,\text{V}$).

To further investigate the changes in the current density and the electroluminescence, these parameter were monitored during the fast J–V_{sweep} scans, with $1.0\,\text{V} \leqslant V_{\text{sweep}} \leqslant 3.5\,\text{V}$ (Figure 4.6a and 4.6b, respectively). The current density does not change significantly with higher values of V_{bias}, except for a slight increase in the built-in voltage V_{bi} of the diode (measured as the value of V_{sweep} where J deviates from the exponential dependence). At the same time, the electroluminescence has a turn-on voltage of 1.0 V and a constant maximum value both independent of the value of V_{bias}. A decrease in the electroluminescence is observed for $V_{\text{sweep}} > 2.0\,\text{V}$, as well as for the external quantum efficiency (EQE, Figure 4.6c). This means that, despite the high current passing through the device, fewer electron-hole pairs actually recombine radiatively. While the higher current may be due to the formation of zones with a high density of charge near to the electrodes, the ion migration due to the external bias can create defects in the bulk of the perovskite, which enhance non-radiative recombination. Biasing device A has overall limited effect on the current density and electroluminescence, except for the degradation of the perovskite itself at high voltages. This is somehow expected since in device A there are virtually no injection barriers for electrons and holes (Figure 4.4a) and the ionic processes are masked by the high current density through the device. The slight increase in the current density in the first few seconds of the biasing process might be due to the doping of the IPH ETL by I^- anions, as recently reported.[109]

The same measurements on device B led to very different results. In DC, the current density begins to drop over time for $V_{\text{bias}} > 1.25\,\text{V}$ and suddenly falls for $V_{\text{bias}} = 1.75\,\text{V}$ (Figure 4.7a) while virtually no electroluminescence could be obtained from the device (Figure 4.7b). This is attributed to the large injection barrier between the Au and the perovskite, which causes the applied bias to drop almost entirely at the Au/MAPbI_3 interface leading to local degradation of the semiconductor. The initial rise of the current density at low bias occurs in the same time scale as for device A, hence it is attributed to the same ionic migration processes. More interestingly, the current density and the electroluminescence during the J-V_{sweep} show a strong dependence on the bias voltage. For moderate values of V_{bias} the current density is low and does not follow the expected diode characteristics, while the electroluminescence is extremely weak. However, for

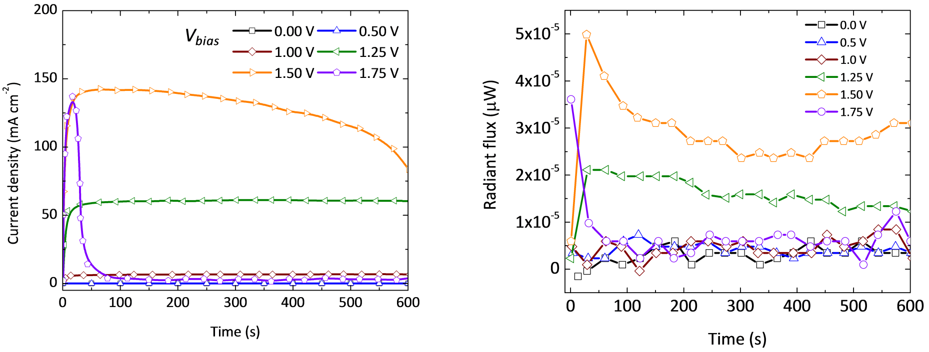

Figure 4.7.: a) Current density and b) electroluminescence in DC from device B for different values of V_{bias}.

$V_{\text{bias}} > 1.0\,\text{V}$ the shape of the current density becomes similar to that observed for the ambipolar device. Importantly, the electroluminescence increases with V_{bias} and its turn-on voltage decreases, shifting towards 1.0 V (Figure 4.8a and 4.8b). This indicates that the charge transport becomes ambipolar and, at the same time, the charge injection is enhanced, because of the applied positive bias. The electroluminescence in device B is rather low (when compared to device A), because of the unfavorable energy level alignment causing the recombination zone to be shifted towards the Au electrode, where non-radiative recombination occurs.

From the above results, it is evident that forward biasing a perovskite diode leads to an improvement in the charge injection in injection-limited devices. The time scale of the observed phenomena (30–50 s) being compatible with the expected migration rate of the ions in perovskite,[111] the mechanism responsible for the improved performances is likely to be analogous to that observed in LECs (see Section 3.1). In particular, the accumulation of ions at the interfaces between the perovskite and the electrodes assists the injection of holes and electrons, indepen-

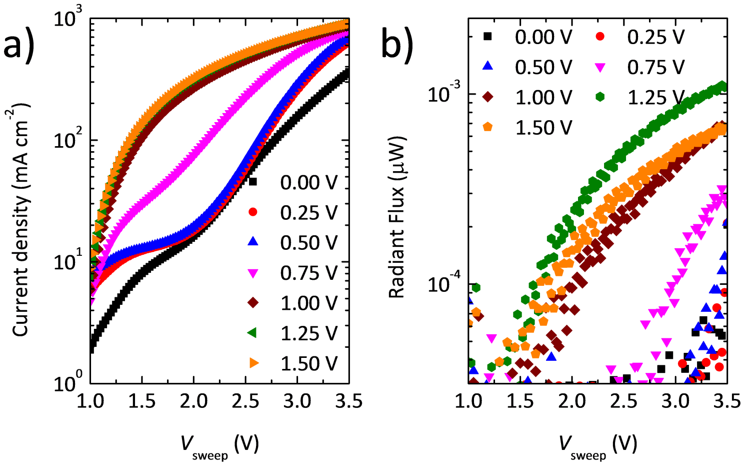

Figure 4.8.: a) Current density and (b) electroluminescence for device B during the fast J–V_{sweep} scans.

dently of the work function of the electrodes (Figure 4.9). It is still unknown if the "perovskite LEC" follows the electrodynamical or the electrochemical model, however, as discussed in the following, the decrease of the photocurrent in a solar cell under bias may indicate that, at some extent, electrochemical doping takes place.

In order to check if the bias-dependent electrical behavior can improve the performances also of an injection-limited photovoltaic device, we studied the behavior of a solar cell (a device of type A) after its exposure to air, which is known to degrade the perovskite absorber. The device had an initial poor efficiency (PCE = 3.15 %), mainly due to its low fill factor (FF = 28.53 %). The short circuit current J_{sc} and the V_{oc} were 11.53 mA cm^2 and 957 mV respectively. The J–V curve presented a typical s-shape around V_{oc}, substantially limiting the FF, indicative of hindered charge extraction (Figure 4.10a). The s-shape feature is often present when the maximum V_{oc} of a solar cell is higher than its built-in volt-

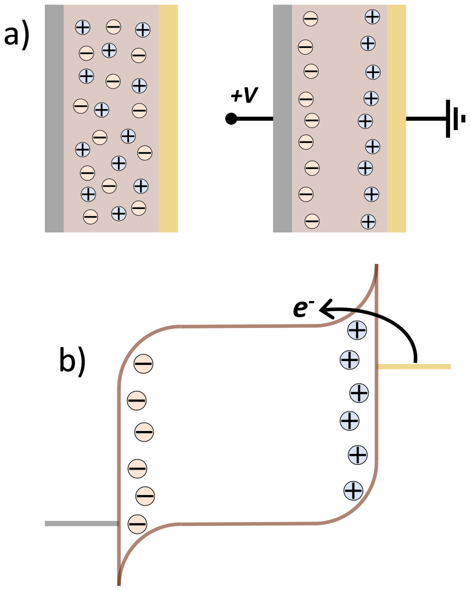

Figure 4.9.: a) Ionic redistribution following the application of an external bias. b) Simplified energy diagram of the unipolar device B after biasing.

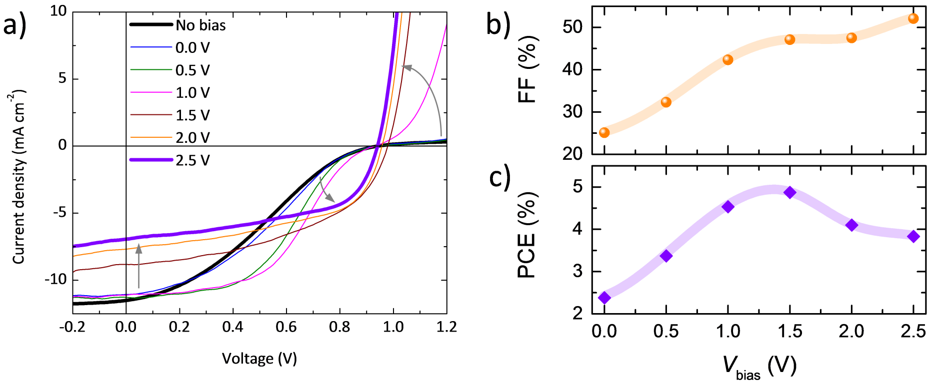

Figure 4.10.: a) Evolution of the J–V curve of a degraded solar cell after 300 s biasing in dark for different values of V_{bias}. b) Evolution of the fill factor and c) evolution of the PCE.

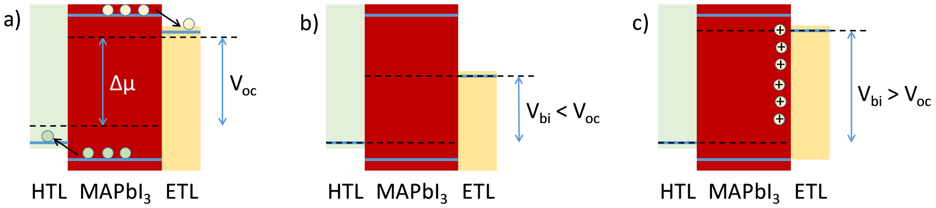

Figure 4.11.: a) Simplified band diagram indicating the maximum attainable V_{oc} as related to the quasi-Fermi level splitting $\Delta\mu$. b) In a degraded solar cells, an extraction barrier is present at least at one of the interfaces (here the ETL), reducing the device built-in voltage and causing s-shaped J–V characteristics. c) Forward biasing the device reduces the barrier for the electron injection (extraction), hence recovering the V_{bi} and the device *FF*.

age, V_{bi}.[115] Biasing the solar cells eliminates the s-shape and increases its *FF* and PCE (Figure 4.10b and c). This behavior can be explained with a reduction of the difference in energy between the conduction band of the perovskite and the LUMO of the ETL as a consequence of the ion accumulation at the electrode interface. In this way, V_{bi} is recovered along with the *FF*. In this picture, we assumed that an extraction barrier is present at least at one of the interfaces, i.e. the ETL (Figure 4.11). The s-shape completely disappears only when $V_{\mathrm{bias}} \geqslant 2.0\,\mathrm{V}$ while the maximum efficiency is reached at $V_{\mathrm{bias}} = 1.5\,\mathrm{V}$, due to a trade-off between J_{sc} and *FF*. This observation is reminiscent of what happens in LECs working in electrochemical regime. The p- and n-doped regions are separated by an intrinsic zone where the recombination of the charge carrier occurs. In our case, the loss in J_{sc} may thus be explained by the formation of such doped zone, which act as quenchers for the photogenerated charges and reduce the effective perovskite absorber thickness. The width of the undoped zone can be estimated assuming a linear relationship between the photocurrent and the thickness of the absorbing layer. In our case, the thickness of the perovskite layer for the unbiased device was 100 nm and the initial photocurrent was $11.53\,\mathrm{mA\,cm^{-2}}$. After 300 s biasing at 2.5 V, the current density decreased to $7.69\,\mathrm{mA\,cm^{-2}}$, corresponding to $\approx$ 67 nm of intrinsic perovskite absorber. Interestingly, this is in agreement with values reported in planar iTMC-LECs at steady state, where the intrinsic region was estimated to be $\approx$ 60 % of the total active layer.[116] Finally, the power conversion efficiency of the degraded device improved in the range 1.5–2.0 V up to a value of 4.87 %, more than a 50 % relative increase.

4.2.3. Conclusions

We have demonstrated that it is possible to enhance the charge injection in diodes based on $MAPbI_3$ by means of forward bias voltage, even in presence of injection energy barriers. This was confirmed by the detection of electroluminescence from an initially single-carrier device. This behavior is similar to that observed in light-emitting electrochemical cells and it is attributed to the presence of mobile ions in the perovskite. A further confirmation of this mechanism was deduced from a degraded solar cell which can be partially recovered when biased in dark for a few minutes. The enhanced PCE is due to a higher FF, i.e. to an improved charge extraction, consequence of the accumulation of ions near one of the interface of the perovskite with the charge transport material. Finally, the reduced J_{sc} of the biased solar cell points towards an electrochemical doping mechanism responsible for the improved extraction/injection of holes and electrons.

4.3. Contribution of the author

E. Bandiello, J. Avila, L. Gil-Escrig, E. Tekelenburg, M. Sessolo, H. J. Bolink, "*Influence of mobile ions on the electroluminescence characteristics of methylammonium lead iodide perovskite diodes*". Journal of Materials Chemistry A, 2016, **4**, 18614-18620. DOI: 10.1039/C6TA06854E

Reproduced by permission of The Royal Society of Chemistry

Journal of
Materials Chemistry A

PAPER

Cite this: J. Mater. Chem. A, 2016, 4, 18614

Influence of mobile ions on the electroluminescence characteristics of methylammonium lead iodide perovskite diodes†

Enrico Bandiello,[a] Jorge Ávila,[a] Lidón Gil-Escrig,[a] Eelco Tekelenburg,[b] Michele Sessolo*[a] and Henk J. Bolink[a]

Received 10th August 2016
Accepted 1st November 2016

DOI: 10.1039/c6ta06854e

www.rsc.org/MaterialsA

In this work, we study the effect of voltage bias on the optoelectronic behavior of methylammonium lead iodide planar diodes. Upon biasing the diodes with a positive voltage, the turn-on voltage of the electroluminescence diminishes and its intensity substantially increases. This behavior is reminiscent of that observed in light-emitting electrochemical cells (LECs), single-layer electroluminescent devices in which the charge injection is assisted by the accumulation of ions at the electrode interface. Because of this mechanism, performances are largely independent from the work function of the electrodes. The similarities observed between planar perovskite diodes and LECs suggest that mobile ions in the perovskite do play an important role in device operation. Besides enhanced electroluminescence, biasing these devices can also result in improved photovoltaic performance.

Introduction

In only a few years, organic–inorganic (hybrid) perovskites, such as the archetype compound methylammonium lead iodide ($MAPbI_3$), have become the most promising materials for future photovoltaic applications, following the demonstration of power conversion efficiencies (PCE) exceeding 20%.[1–3] This PCE could be achieved because of the unique combination of characteristics such as high optical absorption,[4] low bandgap,[5] low exciton binding energy (mainly free carriers are present at room temperature),[6,7] and long-range carrier diffusion length.[8] Hybrid perovskites with wider bandgap have been also used in electroluminescent devices, showing promising efficiencies and electroluminescence intensity.[9–12] High-quality hybrid perovskite thin films can be processed by simple solution or sublimation methods, allowing the preparation of simple and potentially inexpensive photovoltaic devices. Despite such important advantages, some issues need to be addressed before perovskite solar cells can be commercialized. Most perovskites are very sensitive to oxygen and moisture and degrade rapidly in ambient conditions; hence, many studies are devoted to mitigating this instability.[13] Another important aspect is that simple current–voltage sweeps in $MAPbI_3$ solar cells are characterized by a certain degree of hysteresis, and slow transient phenomena often affect the measurements.[14] Several mechanisms responsible for the hysteretic behavior of perovskites have been proposed, *i.e.* capacitive effects due to the interaction between the perovskite and charge transport materials,[15] electronic traps at the interface or grain boundaries of the perovskite,[16] the light-activated reorientation of the MA^+ cations under bias,[17] or a mixed electronic–ionic conductivity, which would imply that mobile ions are present in the bulk of perovskites.[18,19] Theoretical calculations predicted iodide to be the most mobile ion in $MAPbI_3$ thin films (due to lower activation energy for ion migration). The actual I^- motion under external bias has been observed through indirect evidence,[20] and recently, deQuilettes *et al.* also demonstrated that iodide migration can take place in perovskite under illumination.[21] Iodine vacancies and interstitial defects, on the other hand, would play a relevant role only on a timescale of nanoseconds, many orders of magnitude shorter than that of a conventional current density–voltage (J–V) scan.[22] Also, recent experimental observations of ionic redistribution within a perovskite active layer under external bias suggested the migrating species to be the methylammonium ion.[23] Independently from their nature, free ions may originate from non-perfect initial stoichiometry or degradation of the active layer, which leads to the presence of defects and vacancies in the film. Decomposition of the perovskite and reversible generation of free ions due to an external electric field have been also demonstrated at the moderate temperature of 330 K;[24] hence, an analogue effect can be expected at RT, perhaps with a slower time constant. While all these phenomena are most likely, to different extents, responsible for the anomalous hysteresis observed in perovskite devices, the general consensus is that mobile ions are indeed present in perovskites and affect

---

[a] Instituto de Ciencia Molecular, Universidad de Valencia, C/Catedrático J. Beltrán 2, 46980 Paterna, Spain. E-mail: michele.sessolo@uv.es

[b] Faculty of Mathematics and Natural Sciences, University of Groningen, Nijenborgh 4, 9747 AG, Groningen, Netherlands

† Electronic supplementary information (ESI) available. See DOI: 10.1039/c6ta06854e

the device behavior. As an example, an almost-complete switchable photovoltaic behavior in cells with symmetrical electrodes has been demonstrated after biasing the device for a sufficiently long time.[23] In this work, we examine and compare the electrical and electroluminescent characteristics of ambipolar and single-carrier $MAPbI_3$ planar diodes. By means of a combination of direct current (DC) voltage bias and fast J–V sweeps, we show that in ambipolar devices with ohmic charge injection, the electronic processes dominate over the ionic contribution, whereas in hole-only devices, both the current injection and electroluminescence have a strong time- and bias-dependent behavior. The ion redistribution promoted by the applied bias seems to favor the electronic carrier injection by a mechanism already identified in light-emitting electrochemical cells (LECs).[25] The beneficial effect of biasing on a degraded solar cell is shown as a proof of concept.

Results and discussion

The reference $MAPbI_3$ solar cell (device A, energy diagram reported in Fig. 1a) was built on glass slides coated with a pre-patterned indium tin oxide (ITO) electrode. The substrate is coated with a thin (50 nm) film of poly(3,4-ethylenedioxythiophene):polystyrene sulfonate (PEDOT:PSS), followed by a 20 nm thick layer of the electron-blocking material poly(*N*,*N*′-bis(4-butylphenyl)-*N*,*N*′-bis(phenyl)benzidine) (polyTPD). The $MAPbI_3$ perovskite films (100 to 350 nm) were deposited by dual-source vapor deposition using previously published protocols.[26] The fullerene derivative indene–C_{60}–propionic acid hexyl ester (IPH) was then deposited on top by spin-coating, thus acting as the electron transport layer (ETL, 50 nm).[27] The device is finished with a barium/silver anode in the case of the ambipolar devices (Fig. 1b). The hole-only device (device B) does not contain the PEDOT:PSS and IPH layers, and the top electrode is replaced with gold (Fig. 1c). Given the large work function of Au with respect to Ba, a high energy barrier for electron injection is created.

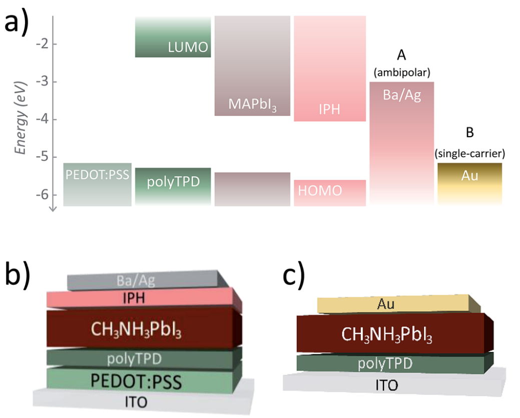

Fig. 1 (a) Flat-band energy diagram for the materials used in device A (Ba/Ag electrode, ambipolar injection) and device B (Au electrode, single-carrier diode). (b) Structure of the reference (ohmic) device with the PEDOT:PSS as the hole injection layer and the Ba/Ag anode. (c) Structure of the single-carrier device, without PEDOT:PSS and with the Au anode.

The reference device A, with a $MAPbI_3$ absorber thickness of 350 nm, shows the expected photovoltaic behavior (Fig. S1†), with a high fill factor (80%, Table S1†), negligible hysteresis in the J–V scans, and a power conversion efficiency (PCE) of 13.7%. For the biasing experiments, a thinner $MAPbI_3$ absorber was used (100 nm) in order to enhance the effect of the applied field at low bias voltage. The measurements consist of biasing the devices with a constant voltage over time and monitoring the current density evolution. At regular intervals (30 s) during the constant voltage operation, the voltage is changed rapidly ($2\ V\ s^{-1}$), and the resulting current density is measured, leading to J–V curves. The fast J–V scans allow decoupling of the electronic processes from other slower phenomena affecting the devices. During these J–V scans, the minimum sweep voltage V_{sweep} has been kept at 1 V in order to avoid the complete relaxation of the system.[25] All the biasing experiments have been performed in the dark to exclude interferences with photogenerated charge carriers. The near-infrared (NIR) electroluminescence has been measured with a Si photodiode.

The current density and radiant flux *versus* time for device A at various constant bias voltages (V_{bias}) is reported in Fig. 2a and 2b. Below a bias of 1 V, the current density is very small, and no substantial electroluminescence was detected. For $V_{bias} > 1.0$ V, a monotonic increase in the current density can be observed with increasing constant bias voltage (Fig. 2a). At each bias voltage, the current transient is monitored, showing a slow rise and then leveling off towards a plateau. For bias voltages above 3.0 V, a maximum current density is reached, after which the current density decreases, and no plateau is observed. The slow increase in current density (bias voltage dependent) is due to a decrease of the charge injection barrier, or an increase in the layer conductivity *versus* time, or to both these effects. The timescale of the current increase is similar to what has been observed in LECs, where ion migration has been identified as the origin of this effect.[25,28,29] The electroluminescence evolution was simultaneously monitored for the different voltages applied (Fig. 2b). The diodes that were biased at voltages above 1.5 V showed a strong decrease of the electroluminescence during the first 30–60 seconds. Such a sudden decrease of the electroluminescence might be due to the formation of quenching species in the proximity of the recombination zone, a consequence of the decomposition of $MAPbI_3$ under the strong electric field ($>9\ V\ \mu m^{-1}$ for $V_{bias} \geq 1.5$ V).[24]

To investigate the observed changes in current density and electroluminescence, fast J–V scans ($1.0\ V \leq V_{sweep} \leq 3.5$ V) were performed after 30 s of biasing for the different V_{bias} values (Fig. 2c–e). With increasing V_{bias}, a small increase in the maximum current density and in the diodes' built-in voltage V_{bi} (estimated as the point where J deviates from the exponential dependence with V_{sweep}, ref. 30) is observed (Fig. 2c). The turn-on voltage for light emission is low and remains constant at about 1.0 V independently from V_{bias} (Fig. 2d). Interestingly, for $V_{bias} \geq 2.0$ V we do observe a decrease of the

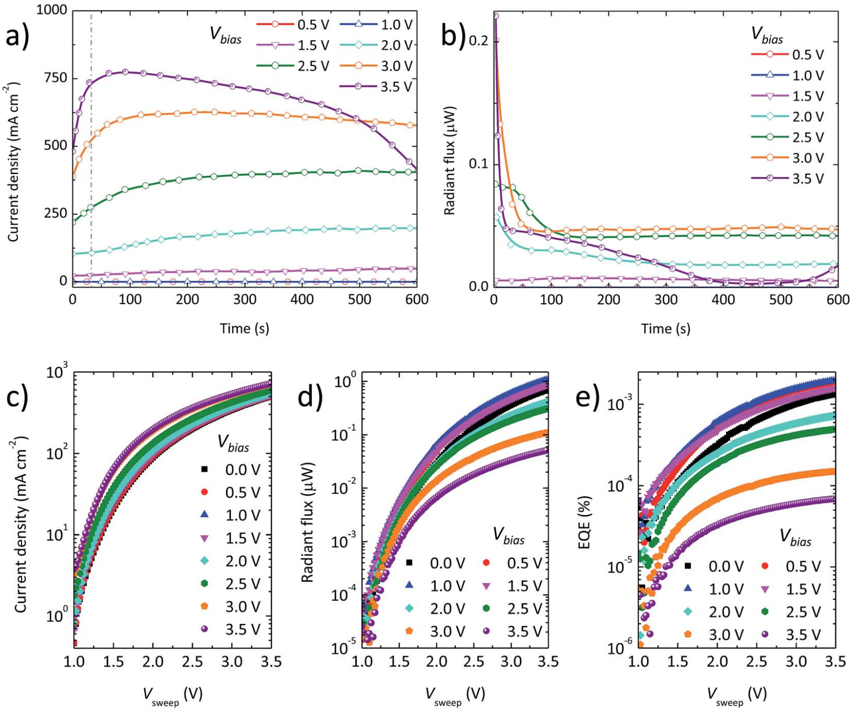

Fig. 2 (a) DC component of the current density and (b) radiant flux *versus* time for the perovskite diode A (ambipolar) for increasing voltage (V_{bias}). (c) Current density, (d) radiant flux and (e) external quantum efficiency (EQE) *versus* applied voltage during fast scans, (V_{sweep}) measured after 30 s biasing at different constant bias voltages.

electroluminescence intensity. Such a performance decrease is very clearly observed from the trend of the external quantum efficiency for electroluminescence *versus* V_{bias} (EQE, Fig. 2e). The increased current density and the simultaneous decrease in electroluminescence at large V_{bias} may be due to the formation of regions with a high density of charge carriers adjacent to the electrode interfaces. At the same time, migration of ions promoted by relatively high values of voltage bias can introduce vacancy defects in the perovskite framework, which can act as traps, giving place to non-radiative recombination for the electrons and holes. In the type A devices, due to the presence of energetically matched electrodes and charge transport materials (Fig. 1), virtually no injection barriers are present. Hence, the ionic effects within the perovskite layer are largely masked by the high current density passing through the device. Also, the slight increase in the current density might be attributed to the interaction between I^- anions and the fullerene acceptor IPH, as recently reported.[20] For the above reasons and to put in evidence the role of the ionic charges in $MAPbI_3$, we prepared single-carrier devices (device B) by replacing the IPH/Ba–Ag with a bare Au electrode and by removing the PEDOT:PSS film. The PEDOT:PSS layer was removed to avoid any transient contribution from the PSS polyelectrolyte.

As expected from the energy level alignment of device B, the current density measured over time for different V_{bias} (Fig. 3a) is much lower with respect to type A devices, and no electroluminescence could be detected in the voltage range used. In type B devices, we observed degradation for $V_{\text{bias}} > 1.5$ V, as can be seen by the fast rise and drop of the current density when the device is biased constantly at $V_{\text{bias}} = 1.75$ V. Due to the large energy barrier at the $MAPbI_3$/Au interface, the applied bias is likely to drop almost entirely at this interface, causing degradation of the perovskite and hence a drastic decrease of the current density. Also for the single-carrier devices, a slow component in the transient current density is present in the first 50 s of the measurement, suggesting that similar processes are occurring for both types of devices (A and B). Hence, we analyzed the fast *J*–*V* scans obtained for $V_{\text{bias}} \leq 1.5$ V after biasing the device for 30 s. For moderate forward-constant biases ($V_{\text{bias}} \leq 0.5$ V), the current density is low and does not show the expected exponential increase as for the diode A (Fig. 3b). In the same voltage range, only very weak electroluminescence is detected, with turn-on voltages as high as 3.0 V (Fig. 3c). With increasing applied constant bias ($V_{\text{bias}} > 0.75$ V), however, the slope of the fast *J*–*V* scan becomes steeper, and for $V_{\text{bias}} \geq 1.0$ V, the current density behavior becomes essentially

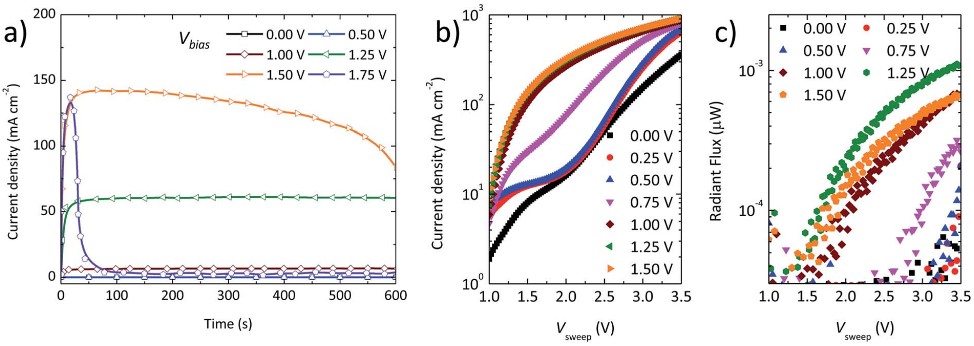

Fig. 3 (a) DC component of the current density for the perovskite diode B (single-carrier device) for increasing constant driving voltage (V_{bias}). (b) Current density and (c) radiant flux *versus* applied voltage during fast scans (V_{sweep}) measured after 30 s bias at different voltages.

analogous to that observed for the ambipolar device (Fig. 2c). Importantly, the radiant flux also increases, and the turn-on voltage gradually shifts towards 1.2 V (Fig. 3c). This, therefore, indicates that the charge carrier injection becomes ambipolar and the injection efficiency is strongly enhanced, as a consequence of positively biasing the device.

In device B, due to a favorable band alignment throughout the ITO/polyTPD/$MAPbI_3$ layers, holes are more efficiently injected than electrons into the perovskite, and the recombination zone is likely to be closer to the perovskite/gold interface, where non-radiative recombination can occur. Biasing device B for a longer time (~300 s) shows no substantial changes in the current density. Nevertheless, electroluminescence can be detected even for $V_{\mathrm{bias}} = 0$ V (Fig. S2†), meaning that the processes assisting electron injection take place even under a very low electric field opposing the built-in potential. It is worth mentioning how the current density before and after the fast *J–V* sweep is essentially equal (Fig. S4†), meaning that the energetics at the interfaces (*i.e.* the ionic distribution) is maintained for short times even when the system is driven out of equilibrium.

From the results presented so far, it is evident that forward-biasing the perovskite diodes leads to an improvement in the charge transport in injection-limited devices. As the time scale of the observed phenomena (30–300 s) is compatible with the expected migration rate of the mobile ions in perovskite,[22] and since no other ionic materials can influence the transient behavior observed for device B, the mechanism underlying the incremented performance is similar to the working principle of LECs. These simple luminescent devices consist of a single electroluminescent layer, either an ionic transition metal complex or an electroluminescent polymer added with ionic species, sandwiched between two electrodes.[31,32] When driven in DC, mobile ions in the bulk of the electroluminescent material accumulate towards the interfaces with the electrodes, forming ionic double layers that facilitate the injection of charge carriers, independently of the work function of the electrodes.

Initially, two modes of operation had been proposed for LECs: the electrochemical model (ECM), in which the charge injection is facilitated by the p- and n-doping of the material near the electrodes,[33–36] and the electrodynamic model (EDM), in which the accumulation of ions lowers the barrier for the charge injection without involving any kind of electrochemical doping.[37,38] Nonetheless, these models seem to be the two extremes of one single mixed mechanism that leans towards EDM or ECM depending on the injection-limited or non-injection-limited character of the device, respectively.[29] Independently of the preferential injection and transport process, the charges in a LEC recombine in the bulk of the emissive layer to give light. The same mechanism is able to explain the behavior of our perovskite diodes. As shown in Fig. 4a, in open-circuit conditions, the ions of opposite signs are uniformly distributed within the active layer. When a constant bias is applied, the ions redistribute, drifting towards the respective electrodes. The ionic accumulation at the perovskite/metal interface is able to assist the electron injection even in a single-carrier device,

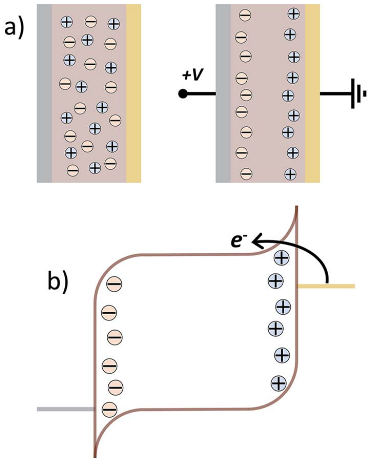

Fig. 4 (a) Schematics of the ionic redistribution following the application of an external bias within a planar diode and (b) simplified energy diagram of the single-carrier device B after biasing.

leading to electroluminescence after biasing. While the injection for holes is nearly ohmic, electrons can tunnel through the injection barrier when enough ions are accumulated at the interface (Fig. 4b). Therefore, the recombination zone is shifted towards the gold cathode, where quenching due to the presence of the metal or due to high ion density reduces the electroluminescence with respect to a device of type A, in which the recombination is expected to take place closer to the center of the perovskite layer. Whether the easier electron injection under bias is due to the lowering of the injection barrier or to an electrochemical doping process is still unknown, but, as we will see in the following, the decrease of the photocurrent for a solar cell under bias may indicate that to some extent, electrochemical doping takes place. It is interesting to note that the turn-on of DC voltage-driven LECs with a comparable thickness of the active layer ~100 nm can be very slow, from many minutes to hours in their simplest configuration,[39] and in any case, it needs electric fields of about 30 V μm^{-1} even for the faster LECs.[40] In the case of hybrid perovskites, this process appears to be much faster, and the fields needed to actually displace the ions from equilibrium can be <4.5 V μm^{-1} (device B, with an inter-electrode spacing of 115 nm, shows light emission after 30 s at 0.5 V bias). Some reports for the analogue bromide perovskite $CH_3NH_3PbBr_3$ suggest that ion migration can be triggered by fields as low as 0.5 V μm^{-1}.[41]

Vacuum-deposited perovskite films, as those used in this work, are composed by densely packed grains with size of about 100–200 nm,[42] which is on the same order of magnitude of the thickness of the films used here (100 nm). In these conditions, ion migration can take place through the grain, as well as through highly defective zones such as grain boundaries.[43] Independently of the actual ionic channel, ions can locally drift, accumulating or depleting at the interfaces between the perovskite emitter and the charge transport materials (modulating the interfacial charge transfer), leaving the light-emitting zone unaffected. In order to see whether the bias-dependent behavior can be applied to improve injection-limited devices, a degraded, air-exposed perovskite solar cell with strong s-shaped *J*–*V* characteristic was used. Such aged cell initially showed an open-circuit voltage (V_{oc}) of 957 mV, a short-circuit current (J_{sc}) of 11.53 mA cm^{-2} and a poor fill factor (FF) of 28.53%, resulting in a power conversion efficiency (PCE) of 3.15%. As can be seen in Fig. 5a, the unbiased device shows a marked s-shape around V_{oc} associated with hindered charge extraction and causing the low FF. The s-shaped feature is present when the maximum V_{oc} of a solar cell is higher than the built-in voltage V_{bi}.[44] Interestingly, the positive biasing of the perovskite diode actually improves the charge extraction and eliminates the s-shaped feature. This phenomenon can be understood by taking into account the reduction of the energy difference between the perovskite and ETL LUMO levels associated with forward-biasing the device (as observed by measuring the electroluminescence). This, in turn, recovers the device V_{bi} and hence the solar cell FF (Fig. S5†). After 300 s biasing in the dark at voltages ranging from 0.0 V to 2.5 V, the s-shape gradually disappears and the FF steadily increases (Fig. 5b). Even if the s-shape completely vanishes only at 2.0 V, the maximum gain in efficiency is reached at a bias of 1.5 V because of a decrease of the current density. The decrease of the current density can be explained again considering the accepted working mechanism of LECs, where ion redistribution under the applied field leaves an intrinsic zone in the middle of the active layer, hence reducing the effective thickness of the perovskite absorber. As anticipated, this may be an indication of the formation of electrochemical doped zones acting as quenchers for the electroluminescence. The thickness of the intrinsic (undoped) zone can be estimated by the linear relation between the photocurrent and the effective thickness of the absorbing layer: the initial 11.53 mA cm^{-2} photocurrent for the device without applied bias (100 nm perovskite thickness) decreases to 7.69 mA cm^{-2} after 300 s biasing in the dark at 2.5 V. This leads to a value of ~67 nm for the thickness of the intrinsic zone, where charge carriers are photo-generated. This is in agreement with the value reported by Meier *et al.* for the thickness of the undoped zone in ionic transition metal complex-based LECs (iTMC-LECs) at steady state (around 60% of the total active layer).[45] In general, the efficiency of the degraded device increases in the range of 1.5–2.0 V applied bias, reaching a maximum value of 4.87%, more than a 50% relative increase (Fig. 5c).

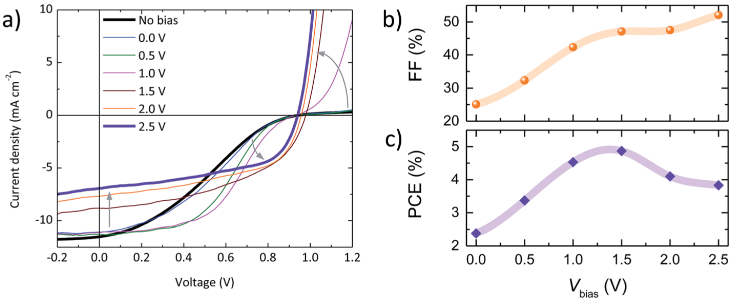

Fig. 5 (a) Evolution of the *J*–*V* characteristics with increasing applied voltages (V_{bias}) for a degraded solar cell biased in the dark (thick black line refers to the pristine device, the thick purple line to the device after biasing at 2.5 V for 300 s). (b) Trend of the fill factor and of the (c) PCE extracted from the same curves.

Conclusions

By means of a combination of forward-DC biasing and fast *J*–*V* scans, we have demonstrated that it is possible to enhance the charge injection into the bulk of perovskite diodes. A device with misaligned energy levels behaves under DC bias as a light-emitting electrochemical cell, suggesting the presence of free ions in the perovskite, which are able to assist the current injection. This is confirmed by monitoring the electroluminescence of single-carrier devices, which gradually appears with lower turn-on voltages and increasing biasing voltage and time.

We show that a degraded solar cell can be partially recovered upon biasing in the dark. The relative efficiency gain is over 50%, mainly due to the increased FF, *i.e.* to the better charge extraction. The decrease of the photocurrent for the same device points toward an electrochemical doping mechanism similar to that already observed in LECs, in which it is responsible for the enhanced charge injection and extraction.

Experimental section

Device fabrication

ITO-covered glass substrates were purchased from Naranjo Substrates. Poly(3,4-ethylenedioxythiophene):poly(styrenesulfonic acid) (PEDOT:PSS) CLEVIOS P VP AI 4083 was purchased from Hereaus Holding and used as received. Poly[*N*,*N*′-bis(4-butylphenyl)-*N*,*N*′-bis(phenyl)benzidine (polyTPD) was purchased from American Dye Source. Indene–C_{60}–propionic acid hexyl ester (IPH) was purchased from Solenne B.V. For their application, polyTPD and IPH were dissolved in chlorobenzene at 7 mg mL^{-1} and 20 mg mL^{-1}, respectively. PbI_2 was purchased from TCI, and CH_3NH_3I from Lumtec; both were used as received.

Devices were prepared on cleaned ITO substrates by spin-coating a thin layer (70 nm) of PEDOT:PSS. On top of this, a thin film of polyTPD (20 nm) was deposited from its chlorobenzene solution. The perovskite was synthesized using a vacuum chamber (1×10^{-6} mbar) integrated in an MBraun glovebox filled with inert gas N_2. The starting materials, CH_3NH_3I and PbI_2, were placed in ceramic crucibles and heated up to 70 °C and 250 °C, respectively. The perovskite layer was then thermally evaporated using a protocol described previously.[26] The IPH layer (40 nm) was deposited from its chlorobenzene solution by spin coating. The metal electrode Ba was thermally evaporated under a base pressure of 2×10^{-6} mbar to a thickness of 10 nm. The devices were then finished by evaporating a 100 nm Ag layer immediately after the Ba.

Device characterization

Diode characterization was performed using a mini sun simulator with a halogen lamp designed by ECN and calibrated with a Si reference cell. The non-encapsulated solar cells were measured in a N_2-filled glovebox. The current density (*J*) *versus* voltage (*V*) characteristics were measured in the dark and under illumination using a 10^{-2} cm^2 shadow mask to prohibit lateral current collection from outside the active area. The bias-sweep experiments were performed on fresh, non-encapsulated devices in a glovebox filled with N_2. A Keithley 2636B Voltage Meter unit, driven by a custom-made LabView program, was used as the voltage source and for the measurement of the current-*versus*-voltage and photocurrent-*versus*-voltage characteristics. The photocurrent was measured directly as the response to the IR emission from a Hamamatsu Si photodiode. The experiments on the aged cell were performed in air on unencapsulated samples kept for a week in air. The tests were performed using a solar simulator calibrated with a Si solar cell. The biasing of the perovskite diodes was performed in the dark, while the *J*–*V* curves were measured under AM 1.5 illumination on a Keithley 2636B Voltage Meter unit using a custom-made LabView program. A shadow mask with an aperture of 10^{-2} cm^2 was used to limit the illuminated area to the central part of the device.

Acknowledgements

We acknowledge financial support from the European Union H2020 project INFORM (grant 675867), the Spanish Ministry of Economy and Competitiveness (MINECO) *via* the Unidad de Excelencia María de Maeztu MDM-2015-0538, MAT2014-55200 and PCIN-2015-255, and the Generalitat Valenciana (Prometeo/2012/053). M. S. and E. B. thank the MINECO for their post-doctoral (JdC) and pre-doctoral grants, respectively. J. A. thanks the Spanish Ministry of Education, Culture and Sport for his pre-doctoral grant.

Notes and references

1 W. S. Yang, J. H. Noh, N. J. Jeon, Y. C. Kim, S. Ryu, J. Seo and S. I. Seok, *Science*, 2015, **348**, 1234–1237.

2 M. Saliba, T. Matsui, J.-Y. Seo, K. Domanski, J.-P. Correa-Baena, M. K. Nazeeruddin, S. M. Zakeeruddin, W. Tress, A. Abate, A. Hagfeldt and M. Grätzel, *Energy Environ. Sci.*, 2016, **9**, 1989–1997.

3 Y. Zhao, J. Wei, H. Li, Y. Yan, W. Zhou, D. Yu and Q. Zhao, *Nat. Commun.*, 2016, **7**, 10228.

4 W. J. Yin, T. Shi and Y. Yan, *Adv. Mater.*, 2014, **26**, 4653–4658.

5 M. M. Lee, J. Teuscher, T. Miyasaka, T. N. Murakami and H. J. Snaith, *Science*, 2012, **338**, 643–647.

6 A. Miyata, A. Mitioglu, P. Plochocka, O. Portugall, J. T.-W. Wang, S. D. Stranks, H. J. Snaith and R. J. Nicholas, *Nat. Phys.*, 2015, **11**, 582–587.

7 K. Galkowski, A. Mitioglu, A. Miyata, P. Plochocka, O. Portugall, G. E. Eperon, J. T.-W. Wang, T. Stergiopoulos, S. D. Stranks, H. J. Snaith and R. J. Nicholas, *Energy Environ. Sci.*, 2016, **9**, 962–970.

8 S. D. Stranks, G. E. Eperon, G. Grancini, C. Menelaou, M. J. Alcocer, T. Leijtens, L. M. Herz, A. Petrozza and H. J. Snaith, *Science*, 2013, **342**, 341–344.

9 Y. H. Kim, H. Cho, J. H. Heo, T. S. Kim, N. Myoung, C. L. Lee, S. H. Im and T. W. Lee, *Adv. Mater.*, 2015, **27**, 1248–1254.

10 H. Cho, S. H. Jeong, M. H. Park, Y. H. Kim, C. Wolf, C. L. Lee, J. H. Heo, A. Sadhanala, N. Myoung, S. Yoo, S. H. Im, R. H. Friend and T. W. Lee, *Science*, 2015, **350**, 1222–1225.

11 M. Sessolo, L. Gil-Escrig, G. Longo and H. J. Bolink, *Top. Curr. Chem.*, 2016, **374**, 52.

12 Y.-H. Kim, H. Cho and T.-W. Lee, *Proc. Natl. Acad. Sci. U. S. A.*, 2016, **113**, 11694–11702.

13 J. S. Manser, M. I. Saidaminov, J. A. Christians, O. M. Bakr and P. V. Kamat, *Acc. Chem. Res.*, 2016, **49**, 330–338.

14 E. L. Unger, E. T. Hoke, C. D. Bailie, W. H. Nguyen, A. R. Bowring, T. Heumüller, M. G. Christoforo and M. D. McGehee, *Energy Environ. Sci.*, 2014, **7**, 3690–3698.

15 H. S. Kim, I. H. Jang, N. Ahn, M. Choi, A. Guerrero, J. Bisquert and N. G. Park, *J. Phys. Chem. Lett.*, 2015, **6**, 4633–4639.

16 Y. Shao, Z. Xiao, C. Bi, Y. Yuan and J. Huang, *Nat. Commun.*, 2014, **5**, 5784.

17 R. Gottesman, E. Haltzi, L. Gouda, S. Tirosh, Y. Bouhadana, A. Zaban, E. Mosconi and F. De Angelis, *J. Phys. Chem. Lett.*, 2014, **5**, 2662–2669.

18 H. J. Snaith, A. Abate, J. M. Ball, G. E. Eperon, T. Leijtens, N. K. Noel, S. D. Stranks, J. T. Wang, K. Wojciechowski and W. Zhang, *J. Phys. Chem. Lett.*, 2014, **5**, 1511–1515.

19 J. M. Frost and A. Walsh, *Acc. Chem. Res.*, 2016, **49**, 528–535.

20 M. De Bastiani, G. Dell'Erba, M. Gandini, V. D'Innocenzo, S. Neutzner, A. R. S. Kandada, G. Grancini, M. Binda, M. Prato, J. M. Ball, M. Caironi and A. Petrozza, *Adv. Energy Mater.*, 2016, **6**, 1501453.

21 D. W. deQuilettes, W. Zhang, V. M. Burlakov, D. J. Graham, T. Leijtens, A. Osherov, V. Bulovic, H. J. Snaith, D. S. Ginger and S. D. Stranks, *Nat. Commun.*, 2016, **7**, 11683.

22 J. M. Azpiroz, E. Mosconi, J. Bisquert and F. De Angelis, *Energy Environ. Sci.*, 2015, **8**, 2118–2127.

23 Y. Yuan, J. Chae, Y. Shao, Q. Wang, Z. Xiao, A. Centrone and J. Huang, *Adv. Energy Mater.*, 2015, **5**, 1500615.

24 Y. Yuan, Q. Wang, Y. Shao, H. Lu, T. Li, A. Gruverman and J. Huang, *Adv. Energy Mater.*, 2016, **6**, 1501803.

25 M. Lenes, G. Garcia-Belmonte, D. Tordera, A. Pertegás, J. Bisquert and H. J. Bolink, *Adv. Funct. Mater.*, 2011, **21**, 1581–1586.

26 M. Liu, M. B. Johnston and H. J. Snaith, *Nature*, 2013, **501**, 395–398.

27 L. Gil-Escrig, C. Momblona, M. Sessolo and H. J. Bolink, *J. Mater. Chem. A*, 2016, **4**, 3667–3672.

28 Q. Pei, G. Yu, C. Zhang, Y. Yang and A. J. Heeger, *Science*, 1995, **269**, 1086–1088.

29 S. van Reenen, P. Matyba, A. Dzwilewski, R. A. Janssen, L. Edman and M. Kemerink, *J. Am. Chem. Soc.*, 2010, **132**, 13776–13781.

30 G.-J. A. H. Wetzelaer and P. W. M. Blom, *NPG Asia Mater.*, 2014, **6**, e110.

31 S. Tang and L. Edman, *Top. Curr. Chem.*, 2016, **374**, 40.

32 S. B. Meier, D. Tordera, A. Pertegás, C. Roldán-Carmona, E. Ortí and H. J. Bolink, *Mater. Today*, 2014, **17**, 217–223.

33 J. Gao and J. Dane, *Appl. Phys. Lett.*, 2004, **84**, 2778.

34 D. J. Dick, A. J. Heeger, Y. Yang and Q. Pei, *Adv. Mater.*, 1996, **8**, 985–987.

35 C. V. Hoven, H. Wang, M. Elbing, L. Garner, D. Winkelhaus and G. C. Bazan, *Nat. Mater.*, 2010, **9**, 249–252.

36 P. Matyba, K. Maturova, M. Kemerink, N. D. Robinson and L. Edman, *Nat. Mater.*, 2009, **8**, 672–676.

37 J. C. deMello, N. Tessler, S. C. Graham and R. H. Friend, *Phys. Rev. B: Condens. Matter Mater. Phys.*, 1998, **57**, 12951–12963.

38 G. G. Malliaras, J. D. Slinker, J. A. DeFranco, M. J. Jaquith, W. R. Silveira, Y.-W. Zhong, J. M. Moran-Mirabal, H. G. Craighead, H. D. Abruna and J. A. Marohn, *Nat. Mater.*, 2008, **7**, 168.

39 S. T. Parker, J. D. Slinker, M. S. Lowry, M. P. Cox, S. Bernhard and G. G. Malliaras, *Chem. Mater.*, 2005, **17**, 3187–3190.

40 E. Zysman-Colman, J. D. Slinker, J. B. Parker, G. G. Malliaras and S. Bernhard, *Chem. Mater.*, 2008, **20**, 388–396.

41 S. Chen, X. Wen, R. Sheng, S. Huang, X. Deng, M. A. Green and A. Ho-Baillie, *ACS Appl. Mater. Interfaces*, 2016, **8**, 5351–5357.

42 C. Momblona, L. Gil-Escrig, E. Bandiello, E. M. Hutter, M. Sessolo, K. Lederer, J. Blochwitz-Nimoth and H. J. Bolink, *Energy Environ. Sci.*, 2016, **9**, 3456–3463.

43 Y. Shao, Y. Fang, T. Li, Q. Wang, Q. Dong, Y. Deng, Y. Yuan, H. Wei, M. Wang, A. Gruverman, J. Shield and J. Huang, *Energy Environ. Sci.*, 2016, **9**, 1752–1759.

44 M. Lenes and H. J. Bolink, *ACS Appl. Mater. Interfaces*, 2010, **2**, 3664–3668.

45 S. B. Meier, D. Hartmann, A. Winnacker and W. Sarfert, *J. Appl. Phys.*, 2014, **116**, 104504.

5. General conclusions

In this thesis we have demonstrated the importance of the interplay between ions and electrons in the working principle of some optoelectronic devices and sensors. Given the broadness of the topic, this has been achieved with reference to some representative cases.

Firstly, we have shown how an electrolyte-gated transistor, which takes advantage of the electrostatic doping operated on an inorganic semiconductor by the ions accumulating at its surface, can be easily converted in an ion sensor or a glucose sensor with a minimal effort. The use of an aqueous electrolyte as the gate insulator allows the transistor to reach its peak performances at a gate voltage lower than that of the electrolysis of the water. Moreover, given that the detection range of both sensors is compatible with the range of K^+ and glucose in humans, such a simple device can in principle be used for the monitoring *in vivo* or *in vitro* of ions of interest and glucose in biomedical applications.

Secondly, the performances of iTMC-based light-emitting electrochemical cells have been studied when inorganic lithium-based salt are used as additives. The characterizing parameters of the LECs are heavily dependent on the chosen additive. In particular, besides the expected changes in the turn-on time due to the presence of ions with very high mobility, also the lifetime and the overall efficiency of the devices show a general improvement, depending on the lithium counterion.

This finding may stimulate the interest towards the use of inorganic lithium salt in light-emitting electrochemical cells, for which ionic liquids are currently the preferred additives.

Finally, the study of the electroluminescence of injection-limited devices based on $CH_3NH_3PbI_3$ perovskite proves that the injection barriers for holes and electrons can be lowered by the same mechanism operating in LECs, due to the presence of mobile ions in the material. This is demonstrated by the increase of the electroluminescence and the decrease of its turn-on voltage when the devices are positively biased for few seconds at increasing voltages. The same experiments, when performed on a degraded solar cell with a poor fill factor, show that the efficiency of the device is partially recovered due to an improved charge extraction. Again, this is attributed to the accumulation of ions at the interface of the perovskite with the hole-transport and electron-transport materials, which improves the fill factor of the device by lowering the extraction barrier for the charge carriers.

6. Resumen en Castellano

6.1. Introducción

En este trabajo se estudian las interacciones entre cargas electrónicas e iónicas y sus aplicaciones en sensores y dispositivos optoelectrónicos. El mecanismo de funcionamiento de los dispositivos optoelectrónicos actualmente más comunes, como los transistores de efecto de campo de capa fina (TFTs), los diodos emisores de luz (LEDs) y las células solares se basa solamente en procesos electrónicos, lo que significa que los efectos de cargas *iónicas* están ausentes, son irrelevantes o incluso perjudiciales para el propósito de dichos dispositivos. Sin embargo, muchas aplicaciones se benefician de la presencia de iones en la estructura de un dispositivo. Un ejemplo típico en el campo de investigación para la búsqueda de fuentes de luz eficientes y baratas son las *células electroquímicas emisoras de luz* (en inglés *light-emitting electrochemical cells*, con acrónimo LECs). Estos dispositivos están basados en una única capa activa de un material electroluminiscente iónico intercalada entre dos electrodos, uno de los cuales es transparente. En los p-LECs (basados en polímeros electroluminiscentes) los iones en la capa activa se añaden en forma de sales, mientras que en los iTMC-LECs (basados en compuesto iónicos de metales de transición, *ionic transition metal complex*, iTMCs) forman parte del complejo electroluminiscente. A menudo, al complejo electroluminiscente se añaden también líquidos iónicos con el fin de mejorar las prestaciones del dispositivo. Cuando se aplica un voltaje V_{bias} a los contactos externos del dispositivo, los iones en la capa activa migran hacia los electrodos, donde generan un campo interfacial que disminuye la barrera de inyección de cargas electrónicas desde los mismos electrodos. Como consecuencia, electrones y huecos son inyectados en los niveles LUMO y HOMO del polímero o del complejo electroluminiscente (HOMO es el acrónimo de *highest occupied molecular level*, e indica el nivel de energía molecular ocupado más elevado, el análogo para los semiconductores orgánicos de la banda de valencia de los semiconductores inorgánicos; asimismo, LUMO, acrónimo de *lowest unoccupied molecular orbital* indica el nivel energético molecular libre más bajo, el análogo para conductores orgánicos de la banda de conducción de los semiconductores inorgánicos). Las cargas inyectadas difunden en el volumen de la capa activa, donde se recombinan radiativamente emitiendo fotones (luz). La inyección de carga asistida por iones se auto-regula, permitiendo la fabricación de un dispositivo emisor de luz sencillo y potencialmente barato, cuyo comportamiento es prácticamente independiente de la función de trabajo de los electrodos.

El equivalente “no iónico” de los LECs son los más conocidos, y ya comercializados, *diodos orgánicos emisores de luz* (*organic light-emitting diodes*, OLEDs). Los OLEDs actualmente más avanzados son dispositivos multicapa cuya fabricación requiere procesos de deposición en múltiples pasos por medio de técnicas de vacío. Estas técnicas son lentas y costosas y limitan la viabilidad comercial de los OLEDs como alternativa económica para el mercado de la iluminación. Las técnicas de deposición por disolución en múltiples pasos son difíciles de poner en práctica, porque el disolvente necesario para depositar una capa puede dañar las capas subyacentes o ser incompatible con ella, generando problemas de uniformidad durante la deposición. En el caso de los OLEDs, el enfoque multicapa es necesarios, a fin de integrar en la estructura del dispositivo materiales para la inyección y el transporte de electrones y huecos y facilitar su transporte y su confinamiento hasta el interior de la capa electroluminiscente. Además, a diferencia de los LECs, los OLEDs a menudo requieren una encapsulación rigurosa (es decir, el contacto con el aire y la humedad tiene que ser eliminado o reducido al extremo), no sólo para proteger el material orgánico, sino también porque metales muy reactivos como Ba o Ca, con función de trabajo baja, son necesarios para asegurar una eficiente inyección de electrones desde el cátodo. Como mencionado anteriormente, estos requisitos no son indispensables en el caso de los LECs. Por lo tanto, en relación a la facilidad de fabricación y a la necesidad de encapsulación, el diferente principio de funcionamiento de los LECs los favorece respecto a los OLEDs, disminuyendo el coste final del dispositivo. Sin embargo, es importante puntualizar que mientras los LECs son un campo de investigación casi exclusivamente académico, los OLEDs representan una tecnología ya madura que se está usando en aplicaciones comerciales, como por ejemplo pantallas para televisores y teléfonos móviles. Por otro lado, la presencia de iones móviles en los LECs hace que éstos puedan potencialmente competir en un futuro en aplicaciones prácticas en las cuales el coste final sea un factor predominante a la hora de elegir entre las tecnologías disponibles.

En muchos casos, la interacción entre los electrones y los iones puede mejorar las prestaciones de dispositivos ya existentes, como en el caso de los *transistores de puerta electrolítica* (*electrolyte-gated transistors*, EGTs). Estos dispositivos son los homólogos de los transistores de película delgada de estado sólido (*thin-film transistors*, TFTs). Los EGTs y los TFTs comparten el mismo principio de funcionamiento, siendo ambos transistores de efecto de campo, pero en los EGTs el aislante de la puerta se substituye por un electrolito líquido o polimérico en contacto directo con el canal semiconductor. Por medio de la aplicación de un voltaje de la puerta V_g, los iones en el electrolito se acumulan en la interfaz con el semiconductor, formando lo que se conoce como una doble capa eléctrica (*electrical double layer*, EDL). Dado que la capacitancia de dicha EDL es mucho más alta que la de los aislantes comúnmente usados en los TFTs, y teniendo en cuenta que la corriente I_d en un transistor es proporcional a dicha capacitancia, la corriente en los EGTs se puede modular usando voltajes de puerta extremadamente bajos (por lo general, $V_\mathrm{g} \leqslant 3\,\mathrm{V}$). Además, la capacitancia del EDL y las prestaciones de un EGT son en principio independientes del grosor del electrolito, simplificando la fabricación del transistor. Lo que es aún más importante, el hecho de que el electrolito esté en contacto directo con el semiconductor implica que éste puede ser modificado o funcionalizado, o que la misma arquitectura del transistor se puede variar, para que el dispositivo funcione come sensor de iones o moléculas en ambiente acuoso o fisiológico.

Más recientemente, otra clase de dispositivos cuyo comportamiento está profundamente influenciado por las interacciones entre iones y electrones está recibiendo mucha atención por parte de la comunidad científica. Estos dispositivos son las células solares basadas en *perovskitas híbridas orgánicas-inorgánicas* (*perovskite solar cells*, PSCs), materiales con la estructura cristalina de tipo perovskita y compuestos por cationes orgánicos intercalados en una estructura inorgánica. La perovskita más comúnmente utilizada es la de ioduro de plomo y metilamonio ($CH_3NH_3PbI_3$ o $MAPbI_3$, donde MA indica el catión orgánico metilamonio). La popularidad de las células solares basadas en estos materiales se debe a su extraordinaria eficiencia (que hoy en día supera el 20 %), unida a la simplicidad y flexibilidad de los métodos de preparación, que van desde la deposición por técnicas de vacío al procesado por disolución. Por otro lado, pese a sus excepcionales eficiencias, las PSCs son dispositivos peculiares que, a diferencia de los dispositivos fotovoltaicos de estado sólido u orgánicos, a menudo muestran un cierto grado de histéresis en las medidas de densidad de corriente–voltaje (J–V), dependiendo de la velocidad y dirección del barrido. También son frecuentes *fenómenos transitorios* en la escala de tiempo de decenas o centenares de segundos, como por ejemplo un incremento *gradual* de la fotocorriente como consecuencia de la exposición a luz. Todo esto complica la obtención unívoca de la efectiva eficiencia de dichos dispositivos, que se determina normalmente a partir de simple barridos J–V. Una de las hipótesis que ha sido barajada para explicar este comportamiento contempla la presencia de iones móviles en la misma perovskita. Estos iones tienen efectos relevantes en el comportamiento de las PSCs y en principio podrían ser usados para mejorar su rendimiento

6.2. Objeto de la tesis

Este trabajo desarrolla tres temas relacionados con los dispositivos mencionados en la Sección 6.1.

1. La fabricación de un sensor de iones potasio K^+ y de un sensor de glucosa a partir de un EGT basado en nanopartículas de ZnO como semiconductor.

2. El estudio del efecto de la adición de sales de litio con diferentes aniones en las prestaciones y el tiempo de vida de iTMC-LECs. Algunas de dichas sales contribuyen a disminuir el tiempo de encendido y a aumentar el tiempo de vida de los dispositivos.

3. El estudio de la electroluminiscencia en diodos basados en la perovskita

$CH_3NH_3PbI_3$. Por medio de la polarización del material, los iones presentes en la perovskita se desplazan y facilitan la inyección de electrones en dispositivos con alta barriera de inyección. Esto conlleva un aumento de la electroluminiscencia, análogamente a lo que pasa para los LECs. Además, se demuestra la recuperación de la eficiencia de una célula solar degradada debido a la polarización externa, como consecuencia de la mejora en la extracción de cargas.

6.3. Transistores de puerta electrolítica como sensores para iones potasio y glucosa

Como se ha mencionado anteriormente, los EGTs pueden ser utilizados como transductores en sensores para iones o moléculas por medio de la funcionalización del semiconductor y/o de modificaciones de la estructura del transistor. En este contexto, se define *sensor* como un dispositivo que permite medir de forma *selectiva* la concentración de una sustancia dada en una disolución. En este trabajo se ha realizado un EGT usando como semiconductor nanopartículas de óxido de zinc (ZnO) depositadas en un sustrato de cristal con electrodos transparentes pregrabados de óxido de indio-estaño (*indium tin oxide*, ITO), que son la fuente y el drenaje del transistor. El electrolito usado es una solución acuosa de cloruro potásico (KCl). Como puerta del transistor se ha usado un electrodo no polarizable de Ag/AgCl, al fin de maximizar la capacitancia del EDL en contacto con el semiconductor. El uso de nanopartículas de ZnO permite obtener una capa con una superficie estructurada que maximiza el área de contacto con el electrolito, al fin de aumentar la modulación de la corriente I_d

El transistor se ha empleado como sensor de iones acoplándolo a una *membrana* *selectiva de iones* (*ion-selective membrane*, ISM). En una membrana de este tipo se origina una diferencia de potencial cuando sus dos caras entran en contacto con disoluciones con diferentes concentraciones de un mismo ion. El término *selectiva* se refiere al hecho de que esta diferencia de potencial en principio se origina sólo en presencia de una determinada especie iónica, en función de la composición de la membrana, aunque cabe añadir que otros iones del mismo signo pueden generar interferencias. Dicha diferencia de potencial se suma algébricamente al voltaje V_g aplicado a la puerta del transistor y modula I_d. La membrana usada para los experimentos en este trabajo incluye en su composición una molécula que enlaza selectivamente a los iones potasio K^+. Al fin de usar el transistor como un sensor de iones, una disolución acuosa con una concentración fija de KCl se ha puesto en contacto directo con la capa de ZnO y con la membrana. La otra cara de la membrana está en contacto con disoluciones de diferentes concentraciones de nitrato potásico $\mathrm{KNO_3}$ y con la puerta de Ag/AgCl. La calibración del sensor se ha llevado a cabo fijando el voltaje de puerta V_g y el voltaje entre la fuente y el drenaje V_d, y midiendo las variaciones de I_d al variar la concentración de $\mathrm{KNO_3}$.

La fabricación del sensor de glucosa se ha llevado a cabo mediante funcionalización directa del semiconductor ZnO con el enzima *oxidasa de glucosa* (GOD). En presencia de una disolución acuosa de glucosa en un electrolito, el enzima cataliza una reacción química que culmina con la producción y sucesiva oxidación de peróxido de hidrógeno $\mathrm{H_2O_2}$ en la superficie de un electrodo de platino (Pt), usado como puerta en lugar del de Ag/AgCl. La oxidación de $\mathrm{H_2O_2}$ transfiere un electrón al Pt, lo que causa una redistribución iónica en el electrolito que modula I_d, habiendo fijado V_g y V_d. La calibración del sensor de glucosa se ha llevado a cabo midiendo la corriente en el semiconductor en función de la concentración de glucosa en una disolución acuosa salina.

6.3.1. Metodología

Una suspensión del 5 % en peso de nanopartículas de ZnO en alcohol etílico se ha depositado por *spin coating* en sustratos de cristal con electrodos pregrabados de ITO. El diámetro medio de las nanopartículas utilizadas es $\leqslant 35\,\mathrm{nm}$. Antes de la deposición, la suspensión ha sido filtrada a través de una membrana de politetrafluoroetileno (PTFE) con poros de 0.22 µm. Debido al bajo punto de ebullición del etanol (78 °C), el proceso de *spin coating* se ha llevado a cabo en una atmósfera saturada del mismo disolvente, para ralentizar su evaporación y obtener capas más uniformes. Después de la deposición las capas han sido sometidas a un tratamiento térmico a una temperatura de 450 °C durante 30 min, con el objetivo de eliminar los ligandos orgánicos que estabilizan las nanopartículas. El grosor final de la capa de nanopartículas, medido per medio de un perfilómetro Ambios XP-1, es de 60 nm. Ningún aislante ha sido depositado entre los contactos de fuente/drenaje y el electrolito. Todo el proceso de fabricación se ha llevado a cabo en una sala limpia de Clase 10000.

Las prestaciones del transistor y las respuestas de los sensores han sido medidas por medio de un potenciostato-amperímetro KEYTHLEY 2636B y un programa en LabView hecho a medida, usando una disolución 10^{-1} M de KCl como electrolito. La capacitancia de las EDLs ha sido medida por espectroscopia de impedancia usando un potenciostato GAMRY INTERFACE 1000. La capacitancia de los EDLs de la capa de nanopartículas se ha comparado con la de una capa de ZnO compacta (obtenida por un método SOL-GEL, disolviendo acetato de zinc dihidrato en una solución 3:1 en volumen de etanol y agua, añadiendo una pequeña cantidad de ácido acético). La disolución ha sido depositada por *spin coating* y luego sometida a un tratamiento térmico a 450 °C para convertir los precursores en ZnO.

La membrana selectiva de iones K^+ se ha fabricado por *drop casting* a partir de una disolución de tetrahidrofurano conteniente cloruro de polivinilo (PVC), diisodecil adipato como plastificante, un ionóforo para iones K^+ y el intercambiador iónico tetrakis(4-clorofenil)-borato. La calibración del sensor se ha realizado por medio de una disolución de referencia en contacto con el semiconductor y con una cara de la ISM (10^{-2} M KCl) y usando disoluciones con concentraciones variables de KNO_3 (10^{-7}–10^{-1} M) para testear la respuesta del sensor. Los voltajes V_g y V_d se han mantenido fijos durante las medidas.

Para funcionalizar el ZnO a fin de fabricar el sensor de glucosa, una disolución de (3-glicidiloxipropil)-trimetoxisilano (GOPS) en isopropanol (alcohol isopropílico) has sido depositada por *spin coating* sobre el ZnO y la capa ha sido calentada a 100 °C durante 10 min. El exceso de GOPS ha sido eliminado enjuagando la capa con una disolución acuosa de KCl 10^{-1} M. Posteriormente, una disolución acuosa de oxidasa de glucosa (GOD) ha sido depositada sobre el transistor y se ha dejado reaccionar durante 12 h a una temperatura de 4 °C, para permitir al GOPS enlazarse con el GOD. El sensor ha sido calibrado como se ha explicado anteriormente, usando disoluciones acuosas de KCl 10^{-1} M con diferentes concentraciones de glucosa. La puerta de Ag/AgCl ha sido sustituida por una de Pt. También en este caso, los valores de V_g y V_d se han mantenido fijos durante las medidas.

6.3.2. Resultados y discusión

El transistor de ZnO presenta una elevada modulación de la corriente a voltajes V_g compatibles con el de electrolisis de agua ($\leqslant 1.2$ V). El voltaje de encendido del transistor es de sólo $V_\mathrm{th} = 0.57$ V e I_d varía en un rango de tres órdenes de magnitud para $0.0\,\mathrm{V} \leqslant V_\mathrm{g} \leqslant 1.2\,\mathrm{V}$. Esto confirma que el transistor funciona en un régimen electrolítico. La capacitancia específica de la EDL medida para la capa de nanopartículas de ZnO es el doble de la medida para la capa compacta ($8.04\,\mu\mathrm{F\,cm}^2$ vs. $4.14\,\mu\mathrm{F\,cm}^2$). Dado que el ZnO es ligeramente soluble en agua, se ha efectuado un test para determinar el tiempo de vida del transistor. En dicho test, el rango de corriente I_d se ha mantenido por encima del 60 % de su valor inicial por un tiempo de 2.5 h, lo que indica una buena estabilidad del dispositivo en ambiente acuoso.

El sensor de iones ha sido capaz de medir la concentración de iones K^+ con un límite de detección de 4.7×10^{-4} M y un incremento linear de I_d de hasta 30 veces entre el límite de detección y la concentración 10^{-1} M de K^+. La sensibilidad del transistor, calculada por medio de la curva de transferencia, es de 44.5 mV por década de concentración de K^+, en línea con valores obtenidos anteriormente para sensores análogos basados en transistores electroquímicos. La falta de aislamiento entre drenaje/fuente y el electrolito seguramente influencia de manera negativa los valores obtenidos, que en todo caso son aceptables para un dispositivo tan sencillo. El tiempo de respuesta del sensor, definido como el tiempo empleado por I_d en alcanzar el 90 % de su valor máximo después de cada variación en la concentración de K^+, es inferior a los 20 s. Finalmente, la selectividad del sensor (es decir, su comportamiento en presencia de iones interferentes como por ejemplo Na^+) sólo depende de la ISM. Una manera de medir dicha selectividad es calcular el logaritmo de la proporción entre las concentraciones de K^+ y Na^+ que generan la misma respuesta en el sensor. Este parámetro se llama coeficiente de selectividad y en nuestro caso vale $-\log\big([\mathrm{K}^+]/[\mathrm{Na}^+]\big) = 2.7$, lo que implica que hace falta una concentración de Na^+ 500 veces más alta que la de K^+ para que el sensor responda de la misma forma a los dos iones

Para fabricar el sensor de glucosa, se ha usado como catalizador una una puerta de Pt, en lugar de la de Ag/AgCl. Siendo el electrodo de platino polarizable, esto causa un descenso general de las prestaciones del dispositivo. El rango de variación de I_d baja a dos órdenes de magnitud, mientras que el voltaje de encendido del transistor aumenta hasta $V_\mathrm{th} = 0.66\,\mathrm{V}$. El sensor es capaz de medir la concentración de glucosa con una respuesta lineal en el rango 7×10^{-4}–$10^{-1}\,\mathrm{M}$, compatible con el contenido de glucosa en la sangre de pacientes sanos (4×10^{-3}–$8 \times 10^{-3}\,\mathrm{M}$) y con diabetes ($2 \times 10^{-3}$–$3 \times 10^{-2}\,\mathrm{M}$).

6.3.3. Conclusiones

Se ha demostrado que es posible la fabricación de un EGT por medio de métodos de disolución a partir de una suspensión de nanopartículas de ZnO. Usando un electrolito acuoso, el transistor presenta los rasgos típicos de los EGTs, como un bajo V_th y una amplia modulación de la corriente I_d. Por medio de la integración de un ISM, se ha podido utilizar el transistor como un sensor de iones K^+ en un amplio rango de concentraciones y con un tiempo de respuesta inferior a los 20 s. Sucesivamente, mediante la funcionalización del ZnO por medio de la enzima oxidasa de glucosa, se ha realizado como prueba de concepto un sensor capaz de detectar la presencia de glucosa en un rango de concentraciones compatible con el contenido de glucosa en la sangre humana. Los resultados anteriores son un ejemplo práctico de la potencialidad de dispositivos de bajo coste y de fácil fabricación basados en EGTs en aplicaciones de detección de iones o de moléculas de interés biológico.

6.4. Influencias del contra anión de sales de litio sobre las prestaciones de las células electroquímicas emisoras de luz

En esta sección se describen las prestaciones de un iTMC-LEC cuando se añaden sales de litio al complejo electroluminiscente.

Como se ha mencionado anteriormente, los LECs son dispositivos que consisten en una capa delgada de material iónico electroluminiscente (de unos 100 nm de grosor) intercalada entre dos electrodos, uno de los cuales es transparente. Su principio de funcionamiento se basa en la presencia de iones móviles en la capa activa. Cuando un voltaje externo es aplicado a los electrodos, los iones de diferentes signos se acumulan en las interfaces entre la capa activa y los electrodos, formado EDLs que bajan las barreras de inyección para electrones y huecos. Dos modelos teóricos se han utilizado para explicar el funcionamiento de los LECs:

- ▷ El *modelo electrodinámico* (ED), según el cual huecos y electrones, una vez inyectados, difunden en el volumen de la capa electroluminiscente. En este modelo la caída de potencial se observa sólo en las EDLs, mientras que en el resto del material el campo es nulo. Los electrones y los huecos están compensados por la diferente concentración local de cationes y aniones.

- ▷ El *modelo electroquímico* (EC), en el cual el potencial sólo cae en las EDLs lo suficiente para permitir la inyección de los portadores de carga. Después de la inyección, los electrones (huecos) en el volumen del iTMC están compensados por cationes (aniones) y llegan a formar zonas dopadas de tipo n y de tipo p, respectivamente, cerca de los electrodos. Las regiones dopadas

> favorecen el transporte de carga y están físicamente separadas por una zona intrínseca, en la cual se ultima la caída de potencial y donde los electrones y los huecos se recombinan dando luz.

Dado que ambos modelos son compatibles con los resultados experimentales, en la comunidad científica tuvo lugar un debate muy intenso sobre cuál de los dos era el "verdadero" modelo que explicaba el funcionamiento de los LECs. Finalmente, en 2010 se estableció que ambos modelos coexisten, lo que significa que los LECs funcionan según un modelo u otro dependiendo del carácter de la interfaz entre el material electroluminiscente y los electrodos. En el caso de contactos casi-óhmicos, el LEC opera según el modelo EC; mientras que en el caso de contactos que limitan la inyección de carga, el LEC opera según el modelo ED. Además, LECs que inicialmente operan según el modelo EC, pueden con el tiempo llegar a operar según el modelo ED a causa de reacciones electroquímicas o parcial oxidación de los electrodos.

Las principales desventajas de los LECs con respecto a los OLEDs están relacionadas con su eficiencia y con su tiempo de vida. Además, el mecanismo de funcionamiento de los LECs depende de la conductividad iónica en la capa activa, así que su tiempo de encendido está determinado por el tiempo necesario para que los iones formen las EDLs en las interfaces con los electrodos. Los iTMCs poseen por norma general una conductividad iónica relativamente baja y, cuando son alimentados a voltaje constante (DC), el tiempo de encendido de los LECs puede ser muy largo, incluso de horas.

Para superar esta limitación se adoptan técnicas diferentes, como la adición de líquidos iónicos a la capa activa, el diseño de complejos optimizados, la introducción de polímeros inertes para facilitar el transporte de iones o el uso de voltajes elevados. Sin embargo, una elevada movilidad iónica causa también un crecimiento muy rápido de las zonas dopadas, lo que reduce el grosor de la zona de recombinación y causa la degradación del dispositivo. En otras palabras, cuando un LEC es alimentado en DC, un bajo tiempo de encendido y un elevado tiempo de vida son mutuamente exclusivos. Una manera de superar esta limitación es alimentar los LECS con una corriente pulsada (con frecuencia $\approx 1\,\mathrm{kHz}$) en forma de onda rectangular, lo que permite obtener bajos tiempos de encendido ($< 1\,\mathrm{s}$) y elevados tiempos de vida ($> 4000\,\mathrm{h}$). El bajo tiempo de encendido se debe al alto voltaje inicial, que permite la rápida redistribución de los iones. En cambio, el largo tiempo de vida se debe a la estabilización de las zonas dopadas: los iones se desplazan hacia los respectivos electrodos durante el intervalo de corriente positiva, mientras que el sistema se relaja durante el resto del ciclo, cuando la corriente es nula. Recientemente, se ha especulado que el bajo tiempo de vida y la baja luminancia en iTMC-LECs sin aditivos se debe a la inyección no equilibrada de electrones y huecos, lo que implica que la zona intrínseca se forme cerca de uno de los electrodos, donde la probabilidad de recombinaciones no radiativas es más elevada. A su vez, esto se debe a que los iTMCs son sales con un catión voluminoso y poco móvil frente a un anión ligero y con alta movilidad (PF_6^-, BF_4^-, ClO_4^-, etc.). En estas condiciones, la densidad de aniones en las EDLs cerca del ánodo es mucho más elevada que la densidad de cationes cerca del cátodo, lo que a su vez favorece la inyección de huecos con respecto a la de electrones. En cierta medida, el mismo problema se presenta también en presencia de líquidos iónicos, que normalmente sufren de una análoga asimetría entre las dimensiones de anión y catión. Una manera de obviar este problema es utilizar sales con una relación de tamaño de catión y anión más balanceada. En particular, LECs con tiempos de encendido muy bajos y alta luminancia se han obtenido añadiendo hexafluorofosfato de litio ($LiPF_6$) a un iTMC. La alta movilidad del ion Li^+, con respecto a la de los cationes normalmente presentes en los iTMCs, permite su rápida redistribución. No obstante, ningún estudio hasta la fecha ha investigado el efecto de diferentes aniones de las sales de litio para su incorporación en iTMC-LECs. En este trabajo se estudia precisamente cómo sales de litio con diferentes aniones afectan las prestaciones de LECs basados en un dado iTMC, $[Ir(ppy)_2(dtb\text{-}bpy)]^+(PF_6)^-$, donde ppy es 2-fenilpiridinato y dtb-bpy es 4,4'-di(tert-butil)-2,2'-bipiridina. En particular los aniones usados para los experimentos han sido: perclorato (ClO_4^-), hexafluorofosfato (PF_6^-), tetrafluoroborato (BF_4^-) y bis(trifluorometano) sulfonamida ($TFSI^-$).

6.4.1. Metodología

Los dispositivos se han fabricado en sustratos de cristal con electrodos de ITO pregrabados, que han sido limpiados por medios químicos (sonicación en agua y jabón y enjuague en agua milliQ y alcohol isopropílico) y físicos (plasma de oxígeno).

Una capa delgada del polímero conductor PEDOT:PSS (80–90 nm) ha sido depositada en el sustrato por *spin coating*, para mejorar la formación de la capa activa y la reproducibilidad de los dispositivos, y sucesivamente sometida a tratamiento térmico (15 min, 150 °C). La suspensión de PEDOT:PSS ha sido filtrada a través de una membrana con poros de 0.45 µm de diámetro antes de la deposición.

Las capas activas se han depositado por *spin coating* a partir de disoluciones en acetonitrilo de $[Ir(ppy)_2(dtb\text{-}bpy)]^+(PF_6)^-$ ($20\,mg\,mL^{-1}$). Cada sal de litio ha sido añadida a la disolución en la proporción de 1 mol de sal cada 9 mol de complejo. Las disoluciones han sido filtradas a través de una membrana con poros de 0.22 µm de diámetro antes de su deposición. El grosor final de la capa de iTMC (y sal) es de 80–90 nm. El grosor de las capas de PEDOT:PSS y de la capa activa ha sido determinado por medio de un perfilómetro mecánico Ambios XP-1. Todo el proceso se ha llevado a cabo en una sala limpia de clase 10000. Los dispositivos se han finalizado con la deposición por evaporación de un cátodo de aluminio de 100 nm de grosor, directamente en contacto con la capa activa. Cada dispositivo constan de cuatro píxeles, con un área de $6.535 \times 10^{-2}\,\mathrm{cm}^2$ cada uno. Un dispositivo adicional basado únicamente en el iTMC, sin sales añadidas, se ha fabricado siguiendo el mismo protocolo y se ha usado como referencia.

Los dispositivos han sido caracterizados en atmósfera inerte de N_2 en una caja de guantes usando un equipo BoTEST OLT OLED Lifetime-Test System. Los LECs han sido alimentados en corriente pulsada, con una densidad de corriente promedio de $100\,\mathrm{A\,m^{-2}}$ ($200\,\mathrm{A\,m^{-2}}$ de pico, 1 kHz y 50 % de ciclo de trabajo).

6.4.2. Resultados y discusión

El dispositivo de referencia muestra una luminancia máxima L_max de $735\,\mathrm{cdm^{-2}}$, un tiempo de encendido t_{100} (tiempo necesario para alcanzar una luminancia de $100\,\mathrm{cd\,m^{-2}}$) de 76 s y un tiempo de vida $t_{1/2}$ (tiempo que emplea la luminancia para bajar a $1/2 L_\mathrm{max}$) de 48 h. En general, la adición de sales de litio mejora todos estos parámetros, con algunas excepciones que se detallarán a continuación. El valor de t_{100} baja hasta los 8 s en el caso de $LiPF_6$ y se mantiene $\leqslant 20$ s en el caso de $LiClO_4$ y LiTFSI. Sin embargo, en el caso de $LiBF_4$, t_{100} se mantiene en el orden de unos 90 s. Se ha encontrado una relación directa entre la disminución del tiempo de encendido y la conductividad iónica de las sales de litio en disolución. El caso del $LiBF_4$ es peculiar, ya que esta sal no aporta ningún beneficio en las fases iniciales del funcionamiento del dispositivo, pese a ser el aditivo con el anión más ligero. Esto se debe a que $LiBF_4$ posee la constante de disociación más pequeña entre las sales usadas, lo que compensa la alta movilidad de sus iones. Sin embargo, en las fases más avanzadas del funcionamiento (100–500 s), la electroluminiscencia del LEC con $LiBF_4$ aumenta más rápidamente que la de cualquier otro dispositivo. La disociación de la sal se ve favorecida por el campo eléctrico aplicado y, después de la disociación, la movilidad superior del Li^+ y del BF_4^- se manifiesta en el rápido crecimiento de la electroluminiscencia.

Con respecto a la luminancia, en todos los casos L_{max} mejora en un 20–30 % con la adición de las sales de litio, superando el valor de $1000\,\mathrm{cd\,m^{-2}}$ en el caso de LiTFSI. Dado que el complejo y la densidad de corriente empleados son los mismos para todos los LECs, este cambio se debe a una mejorada simetría en la formación de las zonas dopadas p y n, en particular permite que la zona intrínseca donde las cargas se recombinan se encuentre en una posición más cercana al centro de la capa activa, donde las recombinaciones no radiativas son menos probables. En el caso del dispositivo de referencia el único ion móvil es el PF_6^- y la densidad de aniones cerca del ánodo es mucho más elevada que la de cationes cerca de la interfaz con el cátodo metálico. Eso favorece la inyección de huecos con respecto a la de electrones y causa que la zona de recombinación esté desplazada hacia el cátodo, lo que propicia recombinaciones no radiativas.

En general, $t_{1/2}$ incrementa con la adicción de las sales de litio. Con la notable excepción del $LiClO_4$, $t_{1/2}$ crece al decrecer el peso molecular del anión. Eso sugiere que también en este caso la mayor simetría en la inyección de carga ralentiza el crecimiento de las zonas dopadas, favoreciendo el aumento de $t_{1/2}$ hasta casi las 2000 horas en el caso de $LiBF_4$, frente a las 48 horas del dispositivo de referencia. El reducido valor de $t_{1/2}$ en el caso de $LiClO_4$ (18 horas) es probablemente debido al carácter fuertemente oxidante del ClO_4^-, que en condiciones de corrientes elevadas puede degradar el complejo orgánico.

La eficiencia de conversión energética de los LECs (PCE) también aumenta como consecuencia de la adicción de las sales de litio. La mejora es más pronunciada en el caso de $\mathrm{LiBF_4}$ ($6.0\,\mathrm{lm\,W^{-1}}$ con respecto a $4.4\,\mathrm{lm\,W^{-1}}$ en el caso del dispositivo de referencia) y más modesta en el caso del $\mathrm{LiClO_4}$ ($4.9\,\mathrm{lm\,W^{-1}}$). Por último, el perfil de voltaje es similar para todos los dispositivos, con un voltaje externo inicial superior a 3.0 V que converge gradualmente hacia 2.5 V. Este valor es comparable con el *band gap* del complejo iónico ($E_\mathrm{g} = 2.7\,\mathrm{eV}$), lo que implica que para todos los LECs la inyección de carga es prácticamente óhmica en su estado estacionario.

6.4.3. Conclusiones

Se ha investigado el efecto de diferentes sales de litio en la capa activa de un iTMC-LEC y se ha demostrado que éstas son aditivos prometedores para dichos dispositivos. La presencia del catión $\mathrm{Li^+}$ mejora la luminancia favoreciendo una mejor inyección desde el cátodo, lo que permite que la formación de la zona de recombinación se sitúe cerca del centro de la capa activa. El mismo razonamiento explica el incremento del tiempo de vida de los dispositivos. La alta movilidad del catión $\mathrm{Li^+}$ es también responsable de la mejora en el tiempo de encendido. Los casos extremos están representados por el $\mathrm{LiClO_4}$, que a pesar de un efecto beneficioso sobre t_{100} reduce drásticamente $t_{1/2}$, y del $\mathrm{LiBF_4}$, que extiende el tiempo de vida del LEC hasta casi las 2000 h sin influir sobre el tiempo de encendido. Resultados intermedios, que en todo caso mejoran los del dispositivo de referencia, se han obtenido usando el $\mathrm{LiPF_6}$ y el LiTFSI.

6.5. Influencia de los iones móviles sobre la electroluminiscencia de diodos basados en perovskita MAPbI$_3$

En esta sección se introducen las perovskitas usadas en células solares, explicando sus propiedades y los aspectos que aún dificultan la comercialización de los dispositivos fotovoltaicos basados en ellas. En particular, el efecto de la presencia de iones móviles en la perovskita de iodo $CH_3NH_3PbI_3$ se ha investigado por medio de medidas de corriente-voltaje.

En los últimos años, una clase de células solares basadas en perovskitas ha suscitado un gran interés en muchos grupos de investigación. Dichas perovskitas son materiales híbridos compuestos por un catión orgánico intercalado en una red inorgánica. Desde su introducción en 2009, las PSCs han alcanzado eficiencias superiores al 20 %, compitiendo así con las células solares inorgánicas. La perovskita más comúnmente utilizada es el ioduro de plomo y metilamonio, con fórmula $CH_3NH_3PbI_3$ ($MAPbI_3$) y en este trabajo nos referiremos a ésta simplemente como *perovskita*. Las razones por las cuales este material es tan atractivo para aplicaciones en dispositivos fotovoltaicos son:

- ▷ Su alto coeficiente de absorción, que les permite absorber una gran cantidad de luz incluso en el caso de capas delgadas ($< 1\,\mu m$).
- ▷ Su bajo *band gap* (1.55 eV), que permite absorber fotones a lo largo de todo el espectro visible.
- ▷ La baja energía de enlace de los excitones (10–16 meV), lo que implica que los electrones y los huecos fotogenerados sean esencialmente libres a

temperatura ambiente

- ▷ La larga distancia de difusión, que supera 1 µm, que permite un transporte y extracción de carga muy eficientes, incluso en presencia de capas relativamente gruesas de perovskita.

- ▷ Los defectos debidos a los bordes de los cristales no crean trampas para las cargas en el *band gap*. En otras palabras, a pesar de ser materiales policristalinos, las perovskitas se comportan como materiales de alta cristalinidad, con respecto al transporte de carga.

- ▷ La alta movilidad de las cargas (60–$500\,\mathrm{cm^2\,V^{-1}\,s^{-1}}$)

- ▷ Los precursores para $MAPbI_3$ son extremadamente baratos y pueden ser procesados tanto por disolución como por métodos de deposición de vacío.

En su configuración más básica, las PSCs se fabrican intercalando una capa de perovskita de unos 500 nm entre un material transportadores de huecos (HTL) y uno transportador de electrones (ETL). Cada uno de estos materiales se elige de forma que bloquee las cargas de signo opuesto por medio de una alineación oportuna de las bandas energéticas. El dispositivo completo siempre incluye un óxido conductor transparente (ITO) y un electrodo de metal que se deposita por evaporación.

A pesar de sus atractivas características y de las eficiencias que se pueden conseguir, la perovskita posee algunas peculiaridades que de momento limitan su uso en aplicaciones prácticas. En primer lugar, es un material que se degrada muy rápidamente en contacto con el aire y la humedad, y por esto muchos estudios están enfocados a mitigar este problema. En segundo lugar, las simples medidas de corriente–voltaje (J–V) en una PSC no siempre dan indicaciones fiables sobre la eficiencia de los dispositivos, dado que a menudo se presentan histéresis y fenómenos transitorios en escalas de tiempo de decenas o centenares de segundos. Una de las explicaciones que se han propuesto para describir este comportamiento atribuye dichos fenómenos a la presencia de iones móviles en la perovskita. En particular estudios teóricos indican iones vacantes MA^+ como responsables de las propiedades observadas, dado que la movilidad de otros iones es demasiado alta (I^-) o demasiado baja ($\mathrm{Pb_2}^+$) para justificar su actuación en las escalas de tiempo observadas. Independientemente de cuáles sean los iones móviles en la perovskita, su origen puede tener lugar en una no perfecta estequiometria o en la degradación del material. Asimismo, se ha demostrado que la perovskita se puede descomponer reversiblemente como consecuencia de un campo eléctrico a una temperatura de tan sólo 300 K, lo que implica que dicha descomposición también puede tener lugar a temperatura ambiente, aunque con una constante de tiempo más baja.

Para estudiar cómo la presencia de iones móviles en la perovskita afecta sus propiedades optoelectrónicas, hemos efectuado una serie de experimentos combinando medidas de densidad de corriente-voltaje y luminancia (en el infrarrojo cercano, *near infrared*, NIR) con voltaje constante (DC), alternadas a barridos rápidos J–V. Se han comparado las medidas realizadas para dos tipos de dispositivos: un diodo óhmico (dispositivo A), es decir por el cual la inyección de cargas no está limitada por los electrodos y por los ETL/HTL, y un dispositivo con una alta barrera de inyección para los electrones (dispositivo B). Además, se ha estudiado el efecto de un voltaje constante aplicado a una célula solar degradada, demostrando los beneficios de la polarización en la eficiencia del dispositivo.

6.5.1. Metodología

Dos tipos de dispositivos han sido fabricados para los experimentos. Los dispositivos de tipo A (de referencia) son diodos ambipolares óhmicos, mientras que los dispositivos de tipo B son unipolares (sólo conducen huecos). Ambos tipos de dispositivos han sido fabricados en sustratos de cristal con electrodos de ITO pregrabados.

Para el dispositivo de tipo A, una capa de PEDOT:PSS de 50 nm ha sido depositada por *spin coating* encima del ITO y luego tratada térmicamente a 150 °C por 15 min. Una capa de 20 nm del HTL/bloqueador de electrones poly(N,N'-bis(4-butilfenil)-N,N'-bis(fenil)benzidina) (polyTPD) ha sido depositada encima del PEDOT:PSS a partir de una disolución en clorobenceno. La capa de $\mathrm{MAPbI_3}$ (100 nm) ha sido depositada por un método de vacío sublimando sus precursores ($\mathrm{CH_3NH_3I}$ y $\mathrm{PbI_2}$) de manera controlada y estequiométrica. El ETL/bloqueador de huecos es un derivado del fullereno (IPH) y se ha depositado sobre la perovskita por *spin coating* a partir de una disolución en clorobenceno (40 nm). El dispositivo se ha completado evaporando un ánodo de Ba/Ag (10 nm/100 nm).

El dispositivo de tipo B ha sido fabricado siguiendo el mismo protocolo, omitiendo las capas de PEDOT:PSS (por su contenido en moléculas cargadas) y de IPH y remplazando el electrodo de Ba/Ag con uno de Au. Siendo la función de trabajo del Au mucho más alta que la del Ba, su nivel de Fermi no está alineado con la banda de conducción de la perovskita, así que el dispositivo B se caracteriza por tener una alta barrera de inyección para los electrones. La fabricación de los dispositivos se ha llevado a cabo en una sala limpia de clase 10000.

Las medidas efectuadas consisten en barridos rápidos J–V_{sweep} ($2\,\mathrm{V\,s^{-1}}$), donde J es la densidad de corriente y V_{sweep} el voltaje durante el barrido. Estos barridos se han efectuado a intervalos regulares ($\approx 30\,\mathrm{s}$) durante la aplicación de un voltaje en DC (V_{bias}). Las medidas en DC proporcionan información sobre los procesos lentos (iónicos) mientras que los barridos rápidos ponen de manifiesto cómo cambian las propiedades de transporte electrónico debido a la polarización. Las medidas de J–V_{sweep} son lo bastante rápidas como para no perturbar la distribución de los iones y, para evitar la relajación completa del sistema, se ha mantenido $V_{\text{sweep}} \leqslant 1\,\text{V}$. En todo momento se ha monitoreado la electroluminiscencia L de los dispositivos, por medio de un fotodiodo de Si. Todos los experimentos han sido llevados a cabo en ausencia de luz en una caja de guantes, bajo atmosfera inerte de N_2. Posteriormente, un dispositivo de referencia (tipo A) se ha dejado al aire libre varios días para permitir su degradación y sus características fotovoltaicas se han medido por medio de un simulador solar bajo una iluminación estándar AM 1.5 G. Por medio de una máscara de sombra, el área iluminada se ha limitado a $10^{-2}\,\text{cm}^2$. Para estudiar el efecto de un voltaje externo, las medidas se han repetido después de polarizar la celda durante 300 s en ausencia de luz a diferentes valores de V_{bias}.

6.5.2. Resultados y discusión

Con la aplicación de $V_{\text{bias}} \leqslant 1\,\text{V}$ la densidad de corriente J en el dispositivo A y su luminancia L son prácticamente nulas. Cuando $V_{\text{bias}} > 1\,\text{V}$, J aumenta lentamente con el tiempo hasta alcanzar un valor fijo en unos 100 s mientras que la componente DC de L decae rápidamente a partir un valor máximo inicial. En este rango de voltaje, la densidad de corriente en los barridos rápidos después de 30 s con $1.0\,\text{V} \leqslant V_{\text{sweep}} \leqslant 3.5\,\text{V}$ muestra el típico aspecto de una curva de diodo, con un crecimiento exponencial y un régimen de saturación. El valor de J y la forma de la curva correspondiente no varían significativamente con V_{bias} y la electroluminiscencia muestra un voltaje de encendido fijo de 1.0 V y un valor máximo prácticamente constante, ambos independientes de V_{bias}. Para valores de $V_{\text{bias}} > 2.0\,\text{V}$, la electroluminiscencia en los barridos decae, aunque J aumente ligeramente. Esto indica que en la perovskita tiene lugar una recombinación no radiativa por interacción de las cargas con defectos en el retículo cristalino causados por el voltaje externo, lo que explica también la rápida disminución de la electroluminiscencia en DC. Para valores de $V_{\text{bias}} > 3.0\,\text{V}$ la componente DC de la corriente alcanza un máximo y luego decrece, a causa de la degradación del material.

En resumen, la aplicación de un bias externo al dispositivo de tipo A, compatiblemente con la estabilidad del material, tiene un efecto casi nulo sobre la densidad de corriente y la electroluminiscencia. La razón se encuentra en el hecho de que la alta densidad de corriente que fluye por el dispositivo enmascara los efectos iónicos. La ligera subida de la corriente en DC en los primeros 100 s puede ser debida al doping del IPH por parte de los iones I^-, como se ha demostrado en trabajos anteriores.

Las mismas medidas, efectuadas en el dispositivo B, muestran resultados completamente diferentes. En este caso, no hay electroluminiscencia en DC, independientemente del valor de V_{bias} y aunque la densidad de corriente al principio se comporte como en el caso del dispositivo A, para valores de $V_{\text{bias}} > 1.25\,\text{V}$ empieza a decaer después de un ascenso inicial, alcanzando valores nulos en ≈ 50 s para $V_{\text{bias}} > 1.75\,\text{V}$. Lo anterior se debe a la alta barrera de inyección entre el Au y la perovskita, que hace que todo el potencial aplicado caiga en la interfaz entre los dos materiales, causando la degradación local del semiconductor híbrido. El inicial incremento de J en DC se desarrolla en la misma escala de tiempo que en el caso del dispositivo A y se atribuye al mismo proceso de migración iónica. Más interesante es el análisis de las curvas J–V_{sweep} después de 30 s de aplicación del voltaje. Para $V_{\text{bias}} < 0.75\,\text{V}$ la densidad de corriente es baja y no sigue el habitual patrón de una corriente de diodo. Sin embargo, cuando $V_{\text{bias}} > 1.0\,\text{V}$, la forma de J es idéntica a la del dispositivo ambipolar. Además, la electroluminiscencia empieza a crecer en intensidad y presenta voltajes de encendido que bajan al aumentar V_{bias}, hasta alcanzar el mismo valor de 1.0 V observado para el dispositivo óhmico. Todo esto confirma que la inyección de cargas es ahora bipolar también en el dispositivo B y que la inyección de electrones es facilitada cuanto más alto sea V_{bias}. La escala de tiempo de los fenómenos (30–50 s) es compatible con la velocidad de migración de los iones en la perovskita. Dado que no hay otros materiales iónicos en el dispositivo B que puedan influenciar su comportamiento, el mecanismo que explica la mejora de las prestaciones es análogo a lo que se observa en los LECs: la acumulación de iones en la interfaz MAPbI$_3$/Au facilita la inyección de electrones independientemente de la función de trabajo del metal.

Para confirmar ulteriormente los resultados anteriores, se ha demostrado que una célula solar degradada (dispositivo tipo A) puede mejorar su eficiencia en un 50 % en términos relativos (desde 3.15 % hasta 4.78 %). La mejora de la eficiencia viene sobre todo del aumento del factor de llenado o de forma (*FF*), directamente relacionado con la eficiencia de la extracción de carga. En este caso, se asume que la célula solar degradada presenta por lo menos en una de las interfaces una barrera de extracción, por ejemplo para los electrones. La acumulación de iones en esta interfaz reduce esa barrera, aumentando el *FF*. Es interesante notar que la densidad de corriente de circuito cerrado J_{sc} proporcionada por la célula solar disminuye con V_{bias}. Esto puede indicar que, de la misma forma que ocurre en un LEC, un proceso de dopaje electroquímico tiene lugar en el volumen de la perovskita cerca de los electrodos. Dado que las zonas dopadas no contribuyen a la foto-generación de cargas, el grosor efectivo de la zona de absorción de luz (zona intrínseca) disminuye con respecto a su valor inicial (100 nm), lo que lleva a disminución de J_{sc}. El valor calculado para el grosor de la zona intrínseca para $V_{\mathrm{bias}} = 2.5\,\mathrm{V}$ es de $\approx 67\,\mathrm{nm}$, compatible con el 60 % del total de la capa activa para iTMC-LECs en estado estacionario, como reportado en la literatura.

6.5.3. Conclusiones

Gracias a la presencia de iones móviles en las perovskitas, se puede mejorar la inyección de carga en $\mathrm{MAPbI_3}$ por medio de la aplicación de un voltaje positivo, análogamente a lo que se ha observado en los LECs. Una confirmación ulterior de este mecanismo viene de la mejora del *FF* (y por lo tanto de la eficiencia) de una célula solar degradada cuando se le aplica un voltaje positivo. Dicho aumento del *FF* está a su vez relacionado con la eliminación de la barrera de extracción de carga debido a la acumulación de iones en las interfaces de la perovskita con el ETL/HTL. Finalmente, la reducción de J_{sc} apunta a un proceso de dopaje electroquímico como responsable de la mejora en la inyección y la extracción de cargas.

6.6. Conclusiones generales

En esta tesis se ha demostrado la importancia de las interacciones entre electrones e iones en el funcionamiento de algunos dispositivos optoelectrónicos y sensores. Para eso, se ha hecho referencia a algunos casos representativos.

Primeramente, se ha demonstrado cómo un transistor de puerta electrolítica se puede fácilmente convertir en un sensor de iones $\mathrm{K^+}$ o de glucosa con mínimos cambios en su estructura. La presencia de un electrolito acuoso como aislante de la puerta permite que el transistor alcance el máximo de sus prestaciones a un voltaje de puerta más bajo que el voltaje de electrólisis del agua. Además, dado que el rango de detección de ambos sensores es compatible con el contenido de K^+ y de glucosa en humanos, este simple dispositivo puede en principio ser utilizado para medir la concentración de iones o moleculas de interés *in vivo* o *in vitro* en aplicaciones biomédicas.

En segundo lugar, se ha estudiado el efecto de la adición de sales inorgánicas de litio a la capa activa de LECs basados en complejos iónicos de metales de transición. Se ha visto que los parámetros de los LECs dependen fuertemente del aditivo. En particular, además de los esperados cambios en el tiempo de encendido debidos a la presencia de iones con muy alta mobilidad, también el tiempo de vida y la eficiencia de los dispositivos muestran una general mejora, en dependencia del anión de la sal de litio. Este descubrimiento puede estimular el interés hacia el uso de sales inorgánicas de litio en LECs, para los cuales los líquidos iónicos son actualmente los aditivos preferenciales.

Finalmente, el estudio de la electroluminiscencia en dispositivos de perovskita $CH_3NH_3PbI_3$ limitados en la inyección de carga, prueba que las barreras de inyección para electrones y huecos pueden ser reducidas por un mecanismo parecido al que actúa en los LECs, debido a la presencia de iones móviles en el material. Esto se demuestra debido al incremento de la electroluminiscencia y a la disminución de su voltaje de encendido cuando se aplica por pocos segundos un *bias* positivo constante a los dispositivos. El mismo experimento, cuando se efectúa sobre células solares degradadas, con un factor de llenado muy bajo, muestra que la eficiencia del dispositivo se recupera parcialmente debido a una mejora de la extracción de cargas. Nuevamente, este hecho se atribuye a la acumulación de iones en la interfases de la perovskita con los materiales transportadores de huecos y electrones, lo que mejora el factor de llenado debido a la reducción de las barreras de extracción para las cargas.

Bibliography

[1] Q. Pei, G. Yu, C. Zhang, Y. Yang, and A. J. Heeger. Polymer light-emitting electrochemical cells. *Science Magazine*, 269(August):1086–1088, 1995.

[2] R. D. Costa, E. Ortí, H. J. Bolink, F. Monti, G. Accorsi, and N. Armaroli. Luminescent ionic transition-metal complexes for light-emitting electrochemical cells. *Angewandte Chemie (International ed. in English)*, 51(33):8178–211, aug 2012.

[3] J. K. Lee, D. S. Yoo, E. S. Handy, and M. F. Rubner. Thin film light emitting devices from an electroluminescent ruthenium complex. *Applied Physics Letters*, 69(12):1686–1688, 1996.

[4] S. T. Parker, J. D. Slinker, M. S. Lowry, M. P. Cox, S. Bernhard, and G. G. Malliaras. Improved turn-on times of iridium electroluminescent devices by use of ionic liquids. *Chemistry of Materials*, 17(12):3187–3190, 2005.

[5] Y. Shen, D. D. Kuddes, C. A. Naquin, T. W. Hesterberg, C. Kusmierz, B. J. Holliday, and J. D. Slinker. Improving light-emitting electrochemical cells with ionic additives. *Applied Physics Letters*, 102(20):203305, 2013.

[6] S. van Reenen, P. Matyba, A. Dzwilewski, R. A. J. Janssen, L. Edman, and M. Kemerink. A Unifying Model for the Operation of Light-

Emitting Electrochemical Cells. *Journal of the American Chemical Society*, 132(39):13776–13781, oct 2010.

[7] D. Hohertz and J. Gao. How electrode work function affects doping and electroluminescence of polymer light-emitting electrochemical cells. *Advanced Materials*, 20(17):3298–3302, 2008.

[8] S. B. Meier, D. Tordera, A. Pertegás, C. Roldán-Carmona, E. Ortí, and H. J. Bolink. Light-emitting electrochemical cells: recent progress and future prospects. *Materials Today*, 17(5):217 – 223, 2014.

[9] R. H. Friend, R. W. Gymer, A. B. Holmes, J. H. Burroughes, R. N. Marks, C. Taliani, D. D. C. Bradley, D. A. D. Santos, J. L. Bredas, M. Logdlund, and W. R. Salaneck. Electroluminescence in conjugated polymers. *Nature*, 397(6715):121–128, jan 1999.

[10] T. Ozel, A. Gaur, J. A. Rogers, and M. Shim. Polymer electrolyte gating of carbon nanotube network transistors. *Nano Letters*, 5(5):905–911, 2005.

[11] M. J. Panzer and C. D. Frisbie. High charge carrier densities and conductance maxima in single-crystal organic field-effect transistors with a polymer electrolyte gate dielectric. *Applied Physics Letters*, 88(20):86–89, 2006.

[12] H. Shimotani, H. Asanuma, J. Takeya, and Y. Iwasa. Electrolyte-gated charge accumulation in organic single crystals. *Applied Physics Letters*, 89(20):203501, 2006.

[13] J. Takeya, K. Yamada, K. Hara, K. Shigeto, K. Tsukagoshi, S. Ikehata, and Y. Aoyagi. High-density electrostatic carrier doping in organic single-

crystal transistors with polymer gel electrolyte. *Applied Physics Letters*, 88(11):112102, 2006.

[14] M. J. Panzer and C. D. Frisbie. High carrier density and metallic conductivity in poly(3-hexylthiophene) achieved by electrostatic charge injection. *Advanced Functional Materials*, 16(8):1051–1056, 2006.

[15] S. H. Kim, K. Hong, W. Xie, K. H. Lee, S. Zhang, T. P. Lodge, and C. D. Frisbie. Electrolyte-gated transistors for organic and printed electronics. *Advanced Materials*, 25(13):1822–1846, apr 2013.

[16] C. Roldán-Carmona, P. Gratia, I. Zimmermann, G. Grancini, P. Gao, M. Graetzel, and Mohammad Khaja Nazeeruddin. High efficiency methylammonium lead triiodide perovskite solar cells: the relevance of non-stoichiometric precursors. *Energy Environ. Sci.*, 8(12):3550–3556, 2015.

[17] Yuchuan Shao, Yongbo Yuan, and Jinsong Huang. Correlation of energy disorder and open-circuit voltage in hybrid perovskite solar cells. *Nature Energy*, 1(1):15001, jan 2016.

[18] Michael Saliba, Taisuke Matsui, Ji-Youn Seo, Konrad Domanski, Juan-Pablo Correa-Baena, Mohammad Khaja Nazeeruddin, Shaik M. Zakeeruddin, Wolfgang Tress, Antonio Abate, Anders Hagfeldt, and Michael Grätzel. Cesium-containing triple cation perovskite solar cells: improved stability, reproducibility and high efficiency. *Energy Environ. Sci.*, 9(6):1989–1997, 2016.

[19] H. J. Snaith, A. Abate, J. M. Ball, G. E. Eperon, T. Leijtens, N. K. Noel, S. D. Stranks, J. Tse-Wei Wang, K. Wojciechowski, and W. Zhang. Anoma-

lous hysteresis in perovskite solar cells. *J. Phys. Chem. Lett.*, 5(9):1511–1515, may 2014.

[20] R. Gottesman, E. Haltzi, L. Gouda, S. Tirosh, Y. Bouhadana, A. Zaban, E. Mosconi, and F. De Angelis. Extremely slow photoconductivity response of $CH_3NH_3PbI_3$ perovskites suggesting structural changes under working conditions. *J. Phys. Chem. Lett.*, 5(15):2662–2669, aug 2014.

[21] J. A. Christians, J. S. Manser, and P. V. Kamat. Best practices in perovskite solar cell efficiency measurements. avoiding the error of making bad cells look good. *J. Phys. Chem. Lett.*, 6(5):852–857, mar 2015.

[22] J. M. Frost and A. Walsh. What is moving in hybrid halide perovskite solar cells? *Accounts of Chemical Research*, 49(3):528–535, mar 2016.

[23] S. M. Sze and K. K. Ng. *Physics of Semiconductor Devices.* John Wiley & Sons Inc, 3rd edition, 2006.

[24] J Zaumseil and H. Sirringhaus. Electron and ambipolar transport in organic field-effect transistors. *Chemical Reviews*, 107(4):1296–1323, apr 2007.

[25] I. Nausieda, K. Kyungbum Ryu, D. Da He, A. I. Akinwande, V. Bulovic, and C. G. Sodini. Dual threshold voltage organic thin-film transistor technology. *IEEE Transactions on Electron Devices*, 57(11):3027–3032, nov 2010.

[26] J. Tate, J. A. Rogers, C. D. W. Jones, B. Vyas, D. W. Murphy, W. Li, Z. Bao, R. E. Slusher, A. Dodabalapur, and H. E. Katz. Anodization and microcontact printing on electroless silver: solution-based fabrication procedures for low-voltage electronic systems with organic active components. *Langmuir*, 16(14):6054–6060, jul 2000.

[27] Y. Inoue, S. Tokito, K. Ito, and T. Suzuki. Organic thin-film transistors based on anthracene oligomers. *J. Appl. Phys.*, 95(10):5795, 2004.

[28] X. J. Yu, J. B. Xu, W. Y. Cheung, and N. Ke. Optimizing the growth of vanadyl-phthalocyanine thin films for high-mobility organic thin-film transistors. *Journal of Applied Physics*, 102(10):103711, 2007.

[29] S. A. DiBenedetto, D. Frattarelli, M. A. Ratner, A. Facchetti, and T. J. Marks. Vapor phase self-assembly of molecular gate dielectrics for thin film transistors. *J. Am. Chem. Soc.*, 130(24):7528–7529, jun 2008.

[30] H. Yan, Z. Chen, Y. Zheng, C. Newman, J. R. Quinn, F. Dötz, M. Kastler, and A. Facchetti. A high-mobility electron-transporting polymer for printed transistors. *Nature*, 457(7230):679–686, jan 2009.

[31] K. Melzer, M. Brändlein, B. Popescu, D. Popescu, P. Lugli, and G. Scarpa. Characterization and simulation of electrolyte-gated organic field-effect transistors. *Faraday Discuss.*, 174:399–411, jun 2014.

[32] L. Kergoat, L. Herlogsson, B. Piro, M. C. Pham, G. Horowitz, X. Crispin, and M. Berggren. Tuning the threshold voltage in electrolyte-gated organic field-effect transistors. *Proceedings of the National Academy of Sciences*, 109(22):8394–8399, may 2012.

[33] L. Herlogsson, Y.-Y. Noh, N. Zhao, X. Crispin, H. Sirringhaus, and M. Berggren. Downscaling of organic field-effect transistors with a polyelectrolyte gate insulator. *Advanced Materials*, 20(24):4708–4713, dec 2008.

[34] S. Ono, N. Minder, Z. Chen, A. Facchetti, and A. F. Morpurgo. High-performance n-type organic field-effect transistors with ionic liquid gates. *Appl. Phys. Lett.*, 97(14):143307, 2010.

[35] S. Park, S.. Lee, C.-H. Kim, I. Lee, W.-J. Lee, S. Kim, B.-G. Lee, J.-H. Jang, and M.-H. Yoon. Sub-0.5 v highly stable aqueous salt gated metal oxide electronics. *Sci. Rep.*, 5:13088, aug 2015.

[36] M. Hamedi, L. Herlogsson, X. Crispin, R. Marcilla, M. Berggren, and O. Inganäs. Fiber-embedded electrolyte-gated field-effect transistors for e-textiles. *Advanced Materials*, 21(5):573–577, dec 2008.

[37] K. Schmoltner, J. Kofler, A.Klug, and E. J. W. List-Kratochvil. Electrolyte-gated organic field-effect transistor for selective reversible ion detection. *Advanced Materials*, 25(47):6895–6899, sep 2013.

[38] C. Suspène, B. Piro, S. Reisberg, M.-C. Pham, H. Toss, M. Berggren, A. Yassar, and G. Horowitz. Copolythiophene-based water-gated organic field-effect transistors for biosensing. *Journal of Materials Chemistry B*, 1(15):2090, 2013.

[39] L. Kergoat, B. Piro, M. Berggren, M.-C. Pham, A. Yassar, and G. Horowitz. DNA detection with a water-gated organic field-effect transistor. *Organic Electronics*, 13(1):1–6, jan 2012.

[40] M. Magliulo, A. Mallardi, M. Y. Mulla, S. Cotrone, B. Rita Pistillo, P. Favia, I. Vikholm-Lundin, G. Palazzo, and L. Torsi. Electrolyte-gated organic field-effect transistor sensors based on supported biotinylated phospholipid bilayer. *Advanced Materials*, 25(14):2090–2094, jan 2013.

[41] M.-G. Kim, H. S. Kim, Y.-G. Ha, J. He, M. G. Kanatzidis, A. Facchetti, and T. J. Marks. High-performance solution-processed amorphous zinc-indium-tin oxide thin-film transistors. *J. Am. Chem. Soc.*, 132(30):10352–10364, aug 2010.

[42] D. Weber, S. Botnaraş, D. V. Pham, J. Steiger, and L. De Cola. Functionalized ZnO nanoparticles for thin-film transistors: support of ligand removal by non-thermal methods. *Journal of Materials Chemistry C*, 1(18):3098, 2013.

[43] M. M. Rahman, A. J. S. Ahammad, J.-H. Jin, S. J. Ahn, and J.-J. Lee. A comprehensive review of glucose biosensors based on nanostructured metal-oxides. *Sensors*, 10(5):4855–4886, may 2010.

[44] S. R. Thomas, P. Pattanasattayavong, and T. D. Anthopoulos. Solution-processable metal oxide semiconductors for thin-film transistor applications. *Chemical Society Reviews*, 42(16):6910, 2013.

[45] Y. Sun and J. A. Rogers. Inorganic semiconductors for flexible electronics. *Advanced Materials*, 19(15):1897–1916, aug 2007.

[46] A. Al Naim and M. Grell. Electron transporting water-gated thin film transistors. *Applied Physics Letters*, 101(14):141603, 2012.

[47] M. Singh, G. Palazzo, G. Romanazzi, G. P. Suranna, N. Ditaranto, C. Di Franco, M. Vittoria Santacroce, M. Y. Mulla, M. Magliulo, K. Manoli, and L. Torsi. Bio-sorbable, liquid electrolyte gated thin-film transistor based on a solution-processed zinc oxide layer. *Faraday Discuss.*, 174:383–398, may 2014.

[48] E. Bakker, P. Bühlmann, and E. Pretsch. Carrier-based ion-selective electrodes and bulk optodes. 1. general characteristics. *Chemical Reviews*, 97(8):3083–3132, dec 1997.

[49] D. J. Macaya, M. Nikolou, S. Takamatsu, J. T. Mabeck, R. M. Owens, and G.G. Malliaras. Simple glucose sensors with micromolar sensitivity based

on organic electrochemical transistors. *Sensors and Actuators B: Chemical*, 123(1):374–378, apr 2007.

[50] B.-K. Sohn, B.-W. Cho, C.-S. Kim, and D.-H. Kwon. ISFET glucose and sucrose sensors by using platinum electrode and photo-crosslinkable polymers. *Sensors and Actuators B: Chemical*, 41(1-3):7–11, jun 1997.

[51] H. J. Bolink, E. Coronado, J. Orozco, and M. Sessolo. Efficient polymer light-emitting diode using air-stable metal oxides as electrodes. *Advanced Materials*, 21(1):79–82, jan 2009.

[52] H. Yuan, H. Shimotani, A. Tsukazaki, A. Ohtomo, M. Kawasaki, and Y. Iwasa. High-density carrier accumulation in ZnO field-effect transistors gated by electric double layers of ionic liquids. *Advanced Functional Materials*, 19(7):1046–1053, apr 2009.

[53] K. Hong, S. H. Kim, K. H. Lee, and C. D. Frisbie. Printed, sub-2v ZnO electrolyte gated transistors and inverters on plastic. *Advanced Materials*, 25(25):3413–3418, mar 2013.

[54] M. Sessolo, J. Rivnay, E. Bandiello, G. G. Malliaras, and H. J. Bolink. Ion-selective organic electrochemical transistors. *Advanced Materials*, 26(28):4803–4807, may 2014.

[55] A. Heller and B. Feldman. Electrochemical glucose sensors and their applications in diabetes management. *Chemical Reviews*, 108(7):2482–2505, jul 2008.

[56] J. D. Slinker, A. A. Gorodetsky, M. S. Lowry, J. Wang, S. Parker, R. Rohl, S. Bernhard, and G. G. Malliaras. Efficient yellow electroluminescence

from a single layer of a cyclometalated iridium complex. *J. Am. Chem. Soc.*, 126(9):2763–2767, mar 2004.

[57] J. D. Slinker, C. Y. Koh, G. G. Malliaras, M. S. Lowry, and S. Bernhard. Green electroluminescence from an ionic iridium complex. *Applied Physics Letters*, 86(17):173506, 2005.

[58] T. Hu, L. He, L. Duan, and Y. Qiu. Solid-state light-emitting electrochemical cells based on ionic iridium(iii) complexes. *Journal of Materials Chemistry*, 22(10):4206, 2012.

[59] C. Yang, Q. Sun, J. Qiao, and Y. Li. Ionic liquid doped polymer light-emitting electrochemical cells. *The Journal of Physical Chemistry B*, 107(47):12981–12988, nov 2003.

[60] R. D. Costa, D. Tordera, E. Ortí, H. J. Bolink, J. Schönle, S. Graber, C. E. Housecroft, E. C. Constable, and J. A. Zampese. Copper(i) complexes for sustainable light-emitting electrochemical cells. *Journal of Materials Chemistry*, 21(40):16108, 2011.

[61] F. G. Gao and A. J. Bard. High-brightness and low-voltage light-emitting devices based on trischelated ruthenium(II) and tris(2,2‘-bipyridine)osmium(II) emitter layers and low melting point alloy cathode contacts. *Chemistry of Materials*, 14(8):3465–3470, aug 2002.

[62] N. Armaroli, G. Accorsi, M. Holler, O. Moudam, J.-F. Nierengarten, Z. Zhou, R. T. Wegh, and R. Welter. Highly luminescent CuI complexes for light-emitting electrochemical cells. *Advanced Materials*, 18(10):1313–1316, may 2006.

[63] A. R. Hosseini, C. Y. Koh, J. D. Slinker, S. Flores-Torres, H. D. Abruña, and G. G. Malliaras. Addition of a phosphorescent dopant in electroluminescent devices from ionic transition metal complexes. *Chemistry of Materials*, 17(24):6114–6116, nov 2005.

[64] J. C. deMello, N. Tessler, S. C. Graham, and R. H. Friend. Ionic space-charge effects in polymer light-emitting diodes. *Physical Review B*, 57(20):12951–12963, may 1998.

[65] J. C. deMello, J. J. M. Halls, S. C. Graham, N. Tessler, and R. H. Friend. Electric field distribution in polymer light-emitting electrochemical cells. *Physical Review Letters*, 85(2):421–424, jul 2000.

[66] J. C. deMello. Interfacial feedback dynamics in polymer light-emitting electrochemical cells. *Physical Review B*, 66(23), dec 2002.

[67] J. D. Slinker, J. A. DeFranco, M. J. Jaquith, W. R. Silveira, Y.-W. Zhong, J. M. Moran-Mirabal, H. G. Craighead, H. D. Abruña, J. A. Marohn, and G. G. Malliaras. Direct measurement of the electric-field distribution in a light-emitting electrochemical cell. *Nature Materials*, 6(11):894–899, sep 2007.

[68] G. G. Malliaras, J. D. Slinker, J. A. DeFranco, M. J. Jaquith, W. R. Silveira, Y.-W. Zhong, J. M. Moran-Mirabal, H. G. Craighead, H. D. Abruña, and J. A. Marohn. Operating mechanism of light-emitting electrochemical cells. *Nature Materials*, 7(3):168–168, mar 2008.

[69] P. Matyba, K. Maturova, M. Kemerink, N. D. Robinson, and L. Edman. The dynamic organic p–n junction. *Nature Materials*, 8(8):672–676, jun 2009.

[70] J. Gao and J. Dane. Visualization of electrochemical doping and light-emitting junction formation in conjugated polymer films. *Applied Physics Letters*, 84(15):2778, 2004.

[71] D. L. Smith. Steady state model for polymer light-emitting electrochemical cells. *J. Appl. Phys.*, 81(6):2869, 1997.

[72] D. J. Dick, A. J. Heeger, Y. Yang, and Q. Pei. Imaging the structure of the p-n junction in polymer light-emitting electrochemical cells. *Advanced Materials*, 8(12):985–987, dec 1996.

[73] H. Rudmann, S. Shimada, and M. F. Rubner. Solid-state light-emitting devices based on the tris-chelated ruthenium(II) complex. 4. high-efficiency light-emitting devices based on derivatives of the tris(2,2‘-bipyridyl) ruthenium(II) complex. *J. Am. Chem. Soc.*, 124(17):4918–4921, may 2002.

[74] R. D. Costa, E. OrtÃ, H. J. Bolink, S. Graber, S. Schaffner, M. Neuburger, C. E. Housecroft, and E. C. Constable. Archetype cationic iridium complexes and their use in solid-state light-emitting electrochemical cells. *Advanced Functional Materials*, 19(21):3456–3463, nov 2009.

[75] D. Tordera, S. Meier, M. Lenes, R. D. Costa, E. Ortí, W. Sarfert, and H. J. Bolink. Simple, fast, bright, and stable light sources. *Advanced Materials*, 24(7):897–900, jan 2012.

[76] Y. Hu and J. Gao. Cationic effects in polymer light-emitting electrochemical cells. *Applied Physics Letters*, 89(25):253514, 2006.

[77] K. J. Suhr, L. D. Bastatas, Y. Shen, L. A. Mitchell, B. J. Holliday, and J. D. Slinker. Enhanced luminance of electrochemical cells with a rationally

designed ionic iridium complex and an ionic additive. *ACS Appl. Mater. Interfaces*, 8(14):8888–8892, apr 2016.

[78] R. Younesi, G. M. Veith, P. Johansson, K. Edström, and T. Vegge. Lithium salts for advanced lithium batteries: Li–metal, li–o_2 , and li–s. *Energy Environ. Sci.*, 8(7):1905–1922, 2015.

[79] V. Aravindan, J. Gnanaraj, S. Madhavi, and H.-K. Liu. Lithium-ion conducting electrolyte salts for lithium batteries. *Chemistry - A European Journal*, 17(51):14326–14346, nov 2011.

[80] K. Xu. Nonaqueous liquid electrolytes for lithium-based rechargeable batteries. *Chemical Reviews*, 104(10):4303–4418, oct 2004.

[81] A. Kojima, K. Teshima, Y. Shirai, and T. Miyasaka. Organometal halide perovskites as visible-light sensitizers for photovoltaic cells. *J. Am. Chem. Soc.*, 131(17):6050–6051, may 2009.

[82] W. S. Yang, J. H. Noh, N. J. Jeon, Y. C. Kim, S. Ryu, J. Seo, and S. I. Seok. High-performance photovoltaic perovskite layers fabricated through intramolecular exchange. *Science*, 348(6240):1234–1237, may 2015.

[83] W.-J. Yin, T. Shi, and Y. Yan. Unique properties of halide perovskites as possible origins of the superior solar cell performance. *Advanced Materials*, 26(27):4653–4658, may 2014.

[84] M. M. Lee, J. Teuscher, T. Miyasaka, T. N. Murakami, and H. J. Snaith. Efficient hybrid solar cells based on meso-superstructured organometal halide perovskites. *Science*, 338(6107):643–647, oct 2012.

[85] N. Pellet, P. Gao, G. Gregori, T.-Y. Yang, M. K. Nazeeruddin, J. Maier, and M. Grätzel. Mixed-organic-cation perovskite photovoltaics for enhanced solar-light harvesting. *Angewandte Chemie International Edition*, 53(12):3151–3157, feb 2014.

[86] Y.-H. Kim, H. Cho, J. H. Heo, T.-S. Kim, N. Myoung, C.-L. Lee, S. H. Im, and T.-W. Lee. Multicolored organic/inorganic hybrid perovskite light-emitting diodes. *Advanced Materials*, 27(7):1248–1254, nov 2014.

[87] H. Cho, S.-H. Jeong, M.-H. Park, Y.-H. Kim, C. Wolf, C.-L. Lee, J. H. Heo, A. Sadhanala, N. Myoung, S. Yoo, S. H. Im, R. H. Friend, and T.-W. Lee. Overcoming the electroluminescence efficiency limitations of perovskite light-emitting diodes. *Science*, 350(6265):1222–1225, dec 2015.

[88] M. Sessolo, L. Gil-Escrig, G. Longo, and H. J. Bolink. Perovskite luminescent materials. *Topics in Current Chemistry*, 374(4), jul 2016.

[89] Y.-H. Kim, H. Cho, and T.-W. Lee. Metal halide perovskite light emitters. *Proceedings of the National Academy of Sciences*, 113(42):11694–11702, sep 2016.

[90] A. Miyata, A. Mitioglu, P. Plochocka, O. Portugall, J. T.-W. Wang, S. D. Stranks, H. J. Snaith, and R. J. Nicholas. Direct measurement of the exciton binding energy and effective masses for charge carriers in organic–inorganic tri-halide perovskites. *Nat Phys*, 11(7):582–587, jun 2015.

[91] K. Galkowski, A. Mitioglu, A. Miyata, P. Plochocka, O. Portugall, G. E. Eperon, J. T.-W. Wang, T. Stergiopoulos, S. D. Stranks, H. J. Snaith, and R. J. Nicholas. Determination of the exciton binding energy and effective

masses for methylammonium and formamidinium lead tri-halide perovskite semiconductors. *Energy Environ. Sci.*, 9(3):962–970, 2016.

[92] S. D. Stranks, G. E. Eperon, G. Grancini, C. Menelaou, M. J. P. Alcocer, T. Leijtens, L. M. Herz, A. Petrozza, and H. J. Snaith. Electron-hole diffusion lengths exceeding 1 micrometer in an organometal trihalide perovskite absorber. *Science*, 342(6156):341–344, oct 2013.

[93] C. Momblona, O. Malinkiewicz, C. Roldán-Carmona, A. Soriano, L. Gil-Escrig, E. Bandiello, M. Scheepers, E. Edri, and H. J. Bolink. Efficient methylammonium lead iodide perovskite solar cells with active layers from 300 to 900 nm. *APL Materials*, 2(8):081504, aug 2014.

[94] Y. Chen, H. T. Yi, X. Wu, R. Haroldson, Y. N. Gartstein, Y. I. Rodionov, K. S. Tikhonov, A. Zakhidov, X.-Y. Zhu, and V. Podzorov. Extended carrier lifetimes and diffusion in hybrid perovskites revealed by hall effect and photoconductivity measurements. *Nature Communications*, 7:12253, aug 2016.

[95] Y. Wu, J. Li, J. Xu, Y. Du, L. Huang, J. Ni, H. Cai, and J. Zhang. Organic–inorganic hybrid $CH_3NH_3PbI_3$ perovskite materials as channels in thin-film field-effect transistors. *RSC Adv.*, 6(20):16243–16249, 2016.

[96] O. Malinkiewicz, C. Roldán-Carmona, A. Soriano, E. Bandiello, L. Camacho, M. K. Nazeeruddin, and H. J. Bolink. Metal-oxide-free methylammonium lead iodide perovskite-based solar cells: the influence of organic charge transport layers. *Advanced Energy Materials*, 4(15):1400345, jun 2014.

[97] M. Liu, M. B. Johnston, and H. J. Snaith. Efficient planar heterojunction

perovskite solar cells by vapour deposition. *Nature*, 501(7467):395–398, sep 2013.

[98] C. Momblona, L. Gil-Escrig, E. Bandiello, E. M. Hutter, M. Sessolo, K. Lederer, J. Blochwitz-Nimoth, and H. J. Bolink. Efficient vacuum deposited p-i-n and n-i-p perovskite solar cells employing doped charge transport layers. *Energy Environ. Sci.*, 9(11):3456–3463, 2016.

[99] W. Chen, Y. Wu, Y. Yue, J. Liu, W. Zhang, X. Yang, H. Chen, E. Bi, I. Ashraful, M. Gratzel, and L. Han. Efficient and stable large-area perovskite solar cells with inorganic charge extraction layers. *Science*, 350(6263):944–948, oct 2015.

[100] J. Zhao, B. Cai, Z. Luo, Y. Dong, Y. Zhang, H. Xu, B. Hong, Y. Yang, L. Li, W. Zhang, and C. Gao. Investigation of the hydrolysis of perovskite organometallic halide $CH_3NH_3PbI_3$ in humidity environment. *Sci. Rep.*, 6:21976, feb 2016.

[101] Y. Bai, Q. Dong, Y. Shao, Y. Deng, Q. Wang, L. Shen, D. Wang, W. Wei, and J. Huang. Enhancing stability and efficiency of perovskite solar cells with crosslinkable silane-functionalized and doped fullerene. *Nature Communications*, 7:12806, oct 2016.

[102] M. L. Petrus, Y. Hu, D. Moia, P. Calado, A. M. A. Leguy, P. R. F. Barnes, and P. Docampo. The influence of water vapor on the stability and processing of hybrid perovskite solar cells made from non-stoichiometric precursor mixtures. *ChemSusChem*, 9(18):2699–2707, sep 2016.

[103] M. Shirayama, M. Kato, T. Miyadera, T. Sugita, T. Fujiseki, S. Hara, H. Kadowaki, D. Murata, M. Chikamatsu, and H. Fujiwara. Degradation

mechanism of $CH_3NH_3PbI_3$ perovskite materials upon exposure to humid air. *J. Appl. Phys.*, 119(11):115501, mar 2016.

[104] Y. Zhao, J. Wei, H. Li, Y. Yan, W. Zhou, D. Yu, and Q. Zhao. A polymer scaffold for self-healing perovskite solar cells. *Nature Communications*, 7:10228, jan 2016.

[105] E. L. Unger, E. T. Hoke, C. D. Bailie, W. H. Nguyen, A. R. Bowring, T. Heumüller, M. G. Christoforo, and M. D. McGehee. Hysteresis and transient behavior in current–voltage measurements of hybrid-perovskite absorber solar cells. *Energy Environ. Sci.*, 7(11):3690–3698, aug 2014.

[106] H.-S. Kim, I.-H. Jang, N. Ahn, M. Choi, A. Guerrero, J. Bisquert, and N.-G. Park. Control of i – v hysteresis in CH_3 NH_3 PbI_3 perovskite solar cell. *J. Phys. Chem. Lett.*, 6(22):4633–4639, nov 2015.

[107] Y. Shao, Z. Xiao, C. Bi, Y. Yuan, and J. Huang. Origin and elimination of photocurrent hysteresis by fullerene passivation in $CH_3NH_3PbI_3$ planar heterojunction solar cells. *Nature Communications*, 5:5784, dec 2014.

[108] Y. Yuan, J. Chae, Y. Shao, Q. Wang, Z. Xiao, A. Centrone, and J. Huang. Photovoltaic switching mechanism in lateral structure hybrid perovskite solar cells. *Advanced Energy Materials*, 5(15):1500615, jun 2015.

[109] M. De Bastiani, G. Dell'Erba, M. Gandini, V. D'Innocenzo, S. Neutzner, A. R. S. Kandada, G. Grancini, M. Binda, M. Prato, J. M. Ball, M. Caironi, and A. Petrozza. Ion migration and the role of preconditioning cycles in the stabilization of theJ-VCharacteristics of inverted hybrid perovskite solar cells. *Advanced Energy Materials*, 6(2):1501453, oct 2015.

[110] D. W. deQuilettes, W. Zhang, V. M. Burlakov, D. J. Graham, T. Leijtens, A. Osherov, V. Bulović, H. J. Snaith, D. S. Ginger, and S. D. Stranks. Photo-induced halide redistribution in organic–inorganic perovskite films. *Nature Communications*, 7:11683, may 2016.

[111] J. M. Azpiroz, E. Mosconi, J. Bisquert, and F. De Angelis. Defect migration in methylammonium lead iodide and its role in perovskite solar cell operation. *Energy Environ. Sci.*, 8(7):2118–2127, 2015.

[112] Y. Yuan, Q. Wang, Y. Shao, H. Lu, T. Li, A. Gruverman, and J. Huang. Electric-field-driven reversible conversion between methylammonium lead triiodide perovskites and lead iodide at elevated temperatures. *Advanced Energy Materials*, 6(2):1501803, dec 2015.

[113] C.A. Gueymard, D. Myers, and K. Emery. Proposed reference irradiance spectra for solar energy systems testing. *Solar Energy*, 73(6):443–467, dec 2002.

[114] M. Lenes, G. Garcia-Belmonte, D. Tordera, A. Pertegás, J. Bisquert, and H. J. Bolink. Operating modes of sandwiched light-emitting electrochemical cells. *Advanced Functional Materials*, 21(9):1581–1586, mar 2011.

[115] M. Lenes and H. J. Bolink. Ionic space-charge effects in solid state organic photovoltaics. *ACS Appl. Mater. Interfaces*, 2(12):3664–3668, dec 2010.

[116] S. B. Meier, D. Hartmann, A. Winnacker, and W. Sarfert. The dynamic behavior of thin-film ionic transition metal complex-based light-emitting electrochemical cells. *Journal of Applied Physics*, 116(10):104504, sep 2014.

List of Figures

List of Tables

Appendices

A. Other contributions of the author

1. O. Malinkiewicz, C. Roldán-Carmona, A. Soriano, E. Bandiello, L. Camacho, M. K. Nazeeruddin, H. J. Bolink, "*Metal-Oxide-Free Methylammonium Lead Iodide Perovskite-Based Solar Cells: the Influence of Organic Charge Transport Layers*". Advanced Energy Materials 2014, 4, 1400345.
2. C. Momblona, O. Malinkiewicz, C. Roldán-Carmona, A. Soriano, L. Gil-Escrig, E. Bandiello, M. Scheepers, E. Edri, H. J. Bolink, "*Efficient methylammonium lead iodide perovskite solar cells with active layers from 300 to 900 nm*". APL Materials. 2014, 2, 081504.
3. M. Sessolo, J. Rivnay, E. Bandiello, G. G. Malliaras, H. J. Bolink, "*Ion-Selective Organic Electrochemical Transistors*". Advanced Materials 2014, 26, 4803.
4. D. Tordera, M. Kuik, Z. D. Rengert, E. Bandiello, H. J. Bolink, G. C. Bazan, T.-Q. Nguyen, "*Operational Mechanism of Conjugated Polyelectrolytes*". Journal of the American Chemical Society 2014, 136, 8500.
5. A. Giovannitti, D.-T. Sbircea, S. Inal, C. B. Nielsen, E. Bandiello, D. A. Hanifi, M. Sessolo, G. G. Malliaras, I. McCulloch, J. Rivnay, "*Controlling the mode of operation of organic transistors through side-chain engineering*". Proceedings of the National Academy of Sciences 2016, 113, 12017.

6. C. Momblona, L. Gil-Escrig, E. Bandiello, E. M. Hutter, M. Sessolo, K. Lederer, J. Blochwitz-Nimoth, H. J. Bolink, "*Efficient vacuum deposited p-i-n and n-i-p perovskite solar cells employing doped charge transport layers*". Energy & Environmental Science 2016, 9, 3456.

7. C. B. Nielsen, A. Giovannitti, D.-T. Sbircea, E. Bandiello, M. R. Niazi, D. A. Hanifi, M. Sessolo, A. Amassian, G. G. Malliaras, J. Rivnay, I. McCulloch, "*Molecular Design of Semiconducting Polymers for High-Performance Organic Electrochemical Transistors*". Journal of the American Chemical Society 2016, 138, 10252.

B. List of symbols and abbreviations

Symbol/acronym	**Meaning**
$[\mathrm{X}^{\mathrm{z}+}]$	Concentrationof ion $\mathrm{X}^{\mathrm{z}+}$ (cation)
μ_e	Electron mobility^{+}
C_ins	Area capacitance of a dielectric
e	Electron charge
EDL	Electrical Double Layer
E_g	Band gap energy
EGT	Electrolyte-Gated Transistor
ETL	Electron transport material
F	Faraday's constant
FET	Field Effect Transistor
GLC	Glucose

Symbol/acronym	Meaning
g_m	Transconductance
GOD	Glucose Oxidase
GOPS	(3-glycidyloxypropyl)trimethoxysilane
HOMO	Highest Occupied Molecular Orbital
HTL	Hole Transport Material
I_d	Drain current
$I_\mathrm{d,sat}$	Saturation drain current
ISM	Ions Selective Membrane
ITO	Indium Tin Oxide
J	Current density
LEC	Light-Emitting Electrochemical Cell
LUMO	Lowest Unoccupied Molecular Orbital
MOx	Metal Oxide
NPE	Non-Polarizable Electrode
OECT	Organic Electrochemical Transistor
OLED	Organic Light-Emitting Diode

Symbol/acronym	**Meaning**
PCE	Power Conversion Efficiency
PSC	Perovskite Solar Cell
PVD	Physical Vapor Deposition
R	Constant of gases
RT	Room Temperature
SC	Solar Cell
TFT	Thin Film Transistor
V_{bi}	Built-in voltage
V_{bias}	Bias voltage
V_{d}	Drain voltage
V_{g}	Gate voltage
V_{th}	Threshold voltage
ϵ	Relative dielectric constant
ϵ_0	Permittivity of vacuum